USING A GATLING-GUN CONFIGURED MICRO PULSED PLASMA THRUSTER AS

A MEANS TO CONTROL MICRO SATELLITES WITH EXTREME PRECISION

THESIS

Lee I. Watson, Captain, USAF

AFIT/GAE/ENY/11-M32

AFIT/GAE/ENY/11-M32

USING A GATLING-GUN CONFIGURED MICRO PULSED PLASMA THRUSTER AS

A MEANS TO CONTROL MICRO SATELLITES WITH EXTREME PRECISION

THESIS

Presented to the Faculty

Department of Aeronautics and Astronautics

Graduate School of Engineering and Management

Air Force Institute of Technology

Air University

Air Education and Training Command

In Partial Fulfillment of the Requirements for the

Degree of Master of Science in Aeronautical Engineering

Lee I. Watson

Captain, USAF

March 2011
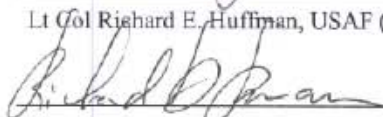
USING A GATLING-GUN CONFIGURED MICRO PULSED PLASMA THRUSTER AS
A MEANS TO CONTROL MICRO SATELLITES WITH EXTREME PRECISION

Lee I. Watson, BS
Captain, USAF

Approved:

Lt Col Richard E. Huffman, USAF (Chairman)	11 Mar 11 Date
Lt Col Richard D. Branam, USAF (Member)	3 May 2011 Date
Dr. William A. Hargus, III (Member)	3 march 2011 Date
Lt Col Carl R. Hartsfield, USAF (Member)	15 Mar 11 Date

Abstract

The number of countries that are gaining access to space is increasing and the drastic increase in both computing and sensor technology has allowed the development of micro (10-100kg), nano (1-10 kg), pico (0.1-1 kg) satellites to be developed and put into orbit to satisfy a particular operational, experimental or functional need. The attractiveness of the micro-Pulsed Plasma Thruster (µPPT) is that the relatively simple construction, reliability, specific Impulse (Isp) of about 800-1000s and require lower power levels than other types of electric thrusters like ion, and hall thrusters. These types of thrusters also supply very small impulse bits on the order of 10-100µN-s per thruster tube and are better equipped for fine attitude and control of the spacecraft, which may be desirable for surveillance or reconnaissance purposes. These thrusters to have a couple of drawbacks to them as well, they are typically not very efficient at converting the electrical energy into thrust with efficiencies typically around 10%. The thrust can also decrease as the µPPT approaches end of life.

The propellant is polytetraflouroethylene (PTFE), also known as Teflon™, which is contained entirely within the thruster, reducing the complexity of the device, eliminating the need for propellant tanks or feed lines. The thruster operates by producing an arc that ablates the surface of the material, and that material is then weakly ionized by the arc and accelerated by electromagnetic forces induced by the arc producing thrust. The Air force Research Laboratory Propulsion Directorate, located at Edwards AFB, CA, developed µPPT initially, as a smaller version of the widely tested Pulsed Plasma thruster. The µPPT has not been tested as extensively as the PPT.

This research is intended to characterize an assembly of nine µPPT thrusters arranged in a 'Gatling Gun' (GG) pattern complete with drive electronics and connections. In doing so, this research will investigate the effects of firing pattern on performance of the GG-µPPT in relation to propellant utilization of each thruster, thrust duration/pattern, the plume discharge and frequency response of the driving electronics.

Table of Contents

ix

List of Figures

List of Tables

List of Symbols

A	Plate Area
A_r	Ratio of LDS and Thruster Radii
B	Magnetic Field Strength (T)
C	Capacitor
C	Dampening Coefficient
D	Plate Diameter
d	Plates Separation Distance
E	Applied Electric Field (V/m)
E'	Effective Electric Field (V/m)
F	Farad
$F(t)$	Forcing Function
g	gram
g_o	Acceleration due to Gravity, 9.81 m/s^2
I$_{bit}$	Impulse Bit,
I$_{total}$	Moment of Interia
Hz	Hertz
I$_{sp}$	Specific Impulse (s)
J	Current (A)
K	CV_o^2 Conversion factor, 96485 (A*s/F)
L	Inductor
M_t	Mass Lost by the Thruster
M_b	Mass Gained by the Collection Bowl
m	milli
$\dot{m}$	Mass Flow (kg/s)
MPD	Magnetoplasmadynamic
N	Newton
N	Number of capacitors
PPT	Pulsed Plasma Thruster
μPPT	Micro-Pulsed Plasma Thruster
PPU	Pulsed Power Unit
Q	Charge of the Plates
q	Charge of the Moving Particles (C)
R	Given Ratio for Arm Movement to Distance Moved (V/m)
R_a	Radius of the Anode
R_c	Radius of the Cathode
r_{LDS}	Radius to LDS Tip (m)
r_t	Radius to Thruster (m)
S	Switch
T	Tesla
torr	Pressure
V	Volts
V_{in}	Input Voltage
V_{LDS}	Laser Displacement Sensor Measured Voltage (V)
V_{out}	Output Voltage

ε_o	Permittivity of Free Space
η	Efficiency
η_f	Frozen Flow Efficiency
η_{heat}	Heat Loss Efficiency
η_o	Overall Efficiency
η_{ppu}	Power Processing Unit Efficiency
η_{prop}	Propellant Efficiency
η_{sh}	Sheath Efficiency
η_{trans}	Transfer Efficiency
Γ	Dampening Coefficient
θ	Motion of arm (rad)
Φ	Late-term Ablation Factor
μ	micro, Torsional Spring Constant
μ_o	Material Permittivity
ν	Fire Rate (Hz), Particle Velocity (m/s)
ω_n	Natural Frequency (Hz)
$w_r.$	Frequency Response
A	State-Transition Matrix
B	Input Matrix
C	Output Matrix
D	Feed Forward Matrix

List of Abbreviations

AFIT	Air Force Institute of Technology
AFRL	Air Force Research Laboratory
BNC	Bayonet Neill-Concelman Coaxial Connector
CCD	Charge Coupled Device
DAQ	Data Acquisition System
DC	Direct Current
GNAT	Geo-orbital Nano-thruster Analysis and Testing Lab
GG	Gatling Gun
LC	Inductor/Capacitor Circuit
LDS	Laser Displacement System
PPT	Pulsed Plasma Thruster
TVAC	Temperature Vacuum Chamber
uPPT	Micro-Pulsed Plasma Thruster
XPPT-1	Thruster used at AFRL
ISR	Intelligence Surveillance Reconnaissance
RMSE	Root Mean Square Error

USING A GATLING-GUN CONFIGURED MICRO PULSED PLASMA THRUSTER AS

A MEANS TO CONTROL MICRO SATELLITES WITH EXTREME PRECISION

I.   Introduction

This research focused on characterizing and determination of the optimum operating conditions of this thruster module. The ability to operate these types of thrusters without excessive carbon build and failure has been an issue for previous research done at AFIT on these types of thrusters. To determine the best operating conditions we need to characterize the performance of the Gatling-Gun micro pulsed plasma thruster (GG-µPPT) under various conditions. However, it is important to understand the various types of electric propulsion (EP) to gain an understanding of the similarities and differences between micro pulsed plasma thrusters and other EP systems.

Chapter 1 discusses the goals and objectives of this research and then explores the different types of EP systems. Chapter 2 focuses on the historical research and results of the pulsed plasma thruster in general and the micro pulsed plasma thruster developed afterwards. Chapter 3 describes the equipment and methodology behind the research conducted. Chapter 4 presents the analysis and results of the research, and Chapter 5 draw conclusions from the results and address future research areas for the GG-µPPT module.

The first objective is to characterize performance of the GG-µPPT. The GG-µPPT is a new device using nine individual µPPTs driven by a single set electronics package. Previous research by Keidar, Boyd, Antonsen, Burton, and Spanjers [1] indicates too high or too low discharge energy can lead to latent-time vaporization, accumulation of carbon deposits and non-uniform arc formation. This phenomenon can result in lost efficiency because as the carbon

builds up more power is required to ionize and the cycle continues until the carbon shorts the electrodes preventing further operation. A secondary objective will be to see how the performance changes with regard to thrust, and efficiency by adjusting the parameters of the single set of drive electronics. To determine the characterization we will need to collect thrust data, firing frequency of the discharges, firing pattern, and power level.

Research Objectives

This research has several objectives. First, characterize the GG-μPPT firing pattern, input power, and frequency. This objective will be accomplished through variation of μPPTs receiving electrical power, increase or decrease of electrical power supplied to μPPTs, and discharge time of the main capacitors to the μPPT. Second, we want to identify the best conditions to operate, focusing on optimized efficiency and longer life of the individual μPPTs. This objective requires determination of the operational envelope of thruster. This task will be accomplished through graphical plots created with power, frequency, and discharge energy, all unique to this thruster, and efficiencies calculated based on the ratio of jet power to discharge power. Third, produce thrust tables designed for more precise control of a satellite through calculation or collection of torque data.

Background

The desire to have a satellite point precisely in the same direction or change its attitude by very small amounts makes the μPPT the right thruster for the job concerning Intelligence, Surveillance, and Reconnaissance (ISR) applications or for very precise north-south station keeping (NSSK). The thruster also finds applications for precision space experiments and astronomy. For instance, the detection of gravitation waves would require very precise positioning relative to the other satellites in the constellation to detect these waves or ripples in

space-time. The waves are generated by massive rotating objects like neutron stars or black holes predicted by Einstein's theory of general relativity [2]. They also find application for many other small satellites like 'CubeSats' where they could be the propulsion source for attitude adjustment and alignment. Electric thrusters have gained more use in recent times, because the manufacturing technology for sensors and equipment has advanced to the point where components are smaller in physical size. This propulsion method is attractive for CubeSats, because their small size does not require massive impulse bits from chemical rockets for re-orient themselves. This niche application for electric thruster propulsion becomes more attractive as precise attitude and control are required for these small satellites and sensor technology power and size decrease with better advances in materials and manufacturing engineering.

The main attractiveness of the micro-pulsed plasma thruster is that they are relatively simple to construct, very reliable, have specific Impulse (Isp) of 800-1000s and require lower power levels than other types of electric thrusters like ion, and hall thrusters. These types of thrusters also supply very small impulse bits on the order of 10-200µN-s per thruster tube and are better equipped for fine attitude and control of the spacecraft, which may be desirable for ISR purposes or interferometer requirements.

They could also find applications on satellites designed for extra-solar planet detection. Early detection methods used the wobble of the star, and the resulting Doppler shift produced as the planet orbits the star and the system oscillates about its center of mass. However, newer methods use the dimming of start light produced occurring when the planet transits the line of sight to the star, which requires precise tracking and orientation capability to detect. They could also counteract potential drag losses for satellites in Low Earth Orbit (LEO). The GG-µPPT is

differentiated from other µPPT systems in that it contains nine thrusters and electronics all housed in one unit, fitting into a 1U (1000 cubic centimeters) package and providing a smoother thrust profile than current µPPT devices in use onboard satellites.

Electric Propulsion

Chemical rockets and thrusters produce thrust through the heating, acceleration, and expulsion of the gas or solid through a nozzle. The specific impulse can be thought of as the fuel efficiency of the thruster, and for chemical rockets, this is limited to about 500 seconds for a Hydrogen-Oxygen rocket. Longer space missions require fuel efficient rockets. This is where electric propulsion has the advantage. Compared to chemical rockets, electric propulsion provide a higher Isp resulting in a lower mass fraction for the same change in velocity. The other drawback to chemical systems is that they rely on pressure forces caused by the chemical reaction and process of combustion to produce thrust. Because the energy transferred to the exhaust products comes from combustion of reactants, chemical rockets are energy density limited due to enthalpy limitations, flame temperatures and temperature limits of the materials exposed to these hot gases. Thrust levels are very high for these devices on the scale of a couple of Newtons to Mega-Newtons (MN).

Electric thrusters get around these limitations by using electro-static, electromagnetic or electrodynamic methods derived from the Lorentz forces [3] and Maxwell's Field Equations [4]. Essentially, three classes of electric thrusters are employed: electrothermal, electrostatic, and electromagnetic. The three categories produce thrust differently, but the main common thread between them is the energy to produce thrust originates from electrical power, not the internal energy of chemical reactions as the case with solid or liquid thrusters. We will now examine the

4

simplest and first kind of EP, the electrothermal thruster that uses electricity to heat the propellant and expand it through a nozzle producing thrust.

Electrothermal Thrusters

The first category of electric thrusters is the electrothermal type like resisto-jets and arc-jets, which use electrical energy to heat a gaseous propellant. These thrusters operate in the following way. First, the cathode is located between prior to the constricted region of the arc jet thruster and this cathode produces a very high-energy arc that attaches to the anode just on the other side of the constrictor. The equivalent temperatures at the core of these arcs are in the range of 10,000-40,000 K, and typical wall temperatures of 1,000-3,000K [3]. Second, propellant is passes along the cavity over the cathode and through the constrictor.

These function very similarly to chemical rockets and have a nozzle that converts the pressure forces to kinetic energy through expansion on the thruster, propelling it forward. However, the kinetic energy relies on the electrical energy to heat the propellant vs. the internal chemical kinetics of combustion. They are also different from other electric thrusters, in that the thrust and acceleration is a purely aerodynamic momentum transfer between the accelerating gas and the nozzle. These thrusters are used on mini and some micro satellites like Telstar™ and have typical Isp of 500-1000s with the upper end requiring use of hydrogen/oxygen propellants [3]. Figure 1 shows a schematic of an arcjet and resistojet thruster [5]. These thrusters can achieve better performance than chemical systems, but Isp is limited by the temperature limitations of the material while exposed to the high temperature gas, arc discharges and erosion of the surfaces of the chamber. Electrostatic thrusters are the next major class of EP thrusters that produce thrust through electrostatic repulsive forces between ions and an electric field.
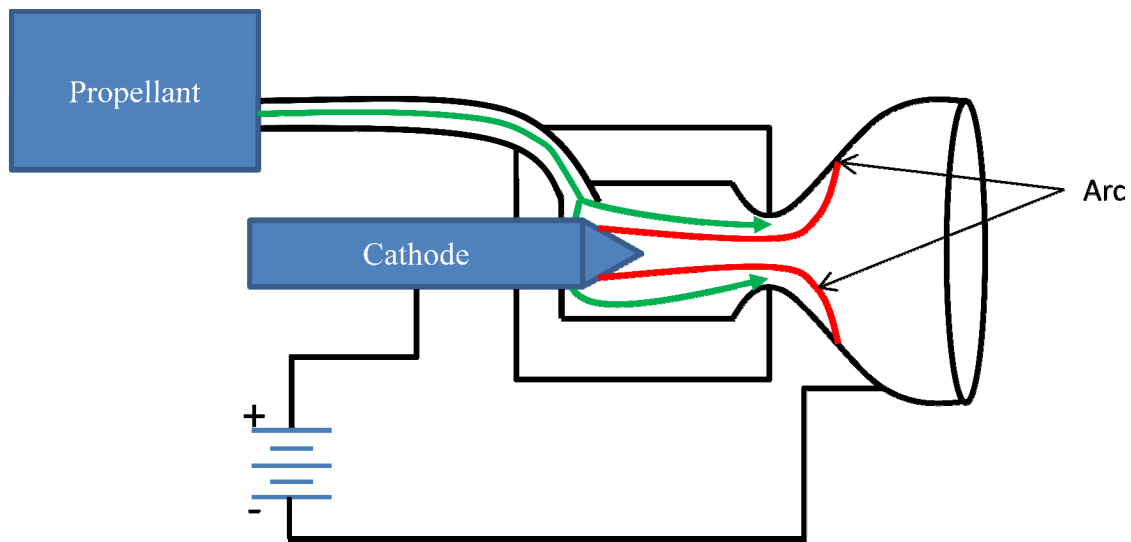
(a) Arc jet schematic.

Propellant is heated as it passes through arc and accelerated out of nozzle by pressure forces
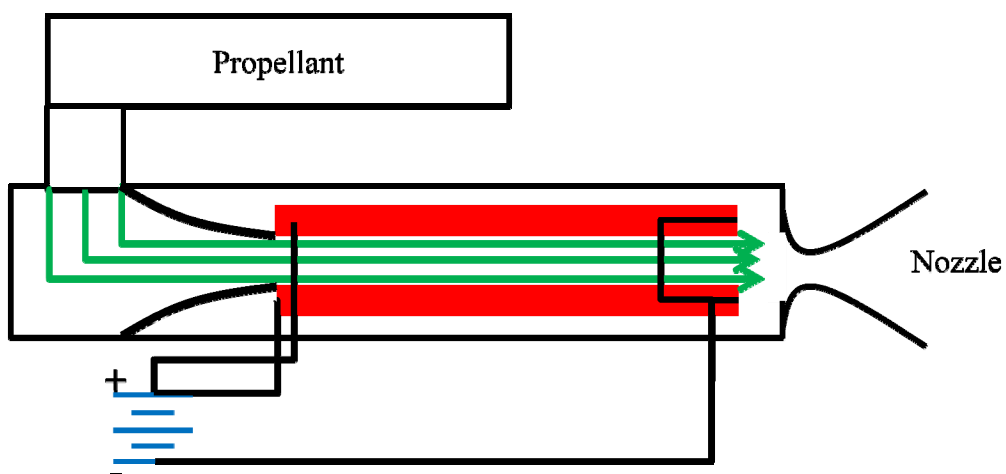
(b) Resisto-jet schematic.

Propellant is heated as it passes resistive elements and accelerated out of the thruster by pressure forces as it passes through the nozzle

Figure 1. Electrothermal Thrusters

Electrostatic Thrusters

These types of thrusters may operate using electrostatic forces to accelerate the particles directly without relying on pressure forces to generate thrust as in the case for electro-thermal propulsive systems (resisto-jet/arc-jet). Ion thrusters are a common type of thruster in this category. The size and complexity of these types of thrusters can vary and power levels can range from a few watts up to 30 kW of electrical power for operation. Ion thrusters work by using cathode to produce a stream of electrons, the electrons then strike propellant atoms (usually Xe or Kr) injected through the a hollow cathode, or through another port. The collision of the electrons with the neutral atoms causes them to lose an electron and become positively ionized. An electrical grid accelerate the ions through electrostatic forces with a potential voltage difference of about 1-2kV where they pass through a grid and are neutralized on the outside by an electron beam to prevent charge accumulation on the thruster and hence the spacecraft.

The propellants are in the gas state for these thrusters and has a pressure vessel containing the propellant and are pressure feed systems. These thrusters are typically the highest power consumption type of thruster due to the high amount of ionization required but offer high very high specific impulse in the range of 2000-10,000 s and efficiencies approaching 90% [4]. Another type of thruster in this category is the Hall thruster, and uses the Hall-effect in conjunction with electrostatic forces to accelerate ions to very high speed producing thrust. This type of thruster operates by using a magnetic field or B field that is perpendicular to the electric or E field. The magnetic field 'holds' back the electrons, while ionization takes place, though the electrons do have a drift velocity and eventually reach the cathode, causing cathode erosion. The electrons then collide with the propellant ionizing them. The E field then accelerates the

ions that have a net positive charge out of the thruster, producing a momentum exchange and producing thrust as shown in Figure 2.

Hall thrusters are electrically simpler than their electrostatic counterparts, but because of about 30 percent of the discharge current produces electrons, which do not directly contribute to thrust, they are about 70% thrust efficient with regard to utilization. However, they are about 80-90 percent efficient at ionizing the propellant so overall they have a total efficiency between 54 and 63% taking the products of the two previous numbers.

The application of electrostatic thrusters in deep space missions provides a way to explore our solar system beyond our planet and the DEEP SPACE-1 spacecraft is a good example of such a spacecraft [6], designed to test the performance of an ion thruster. Future mission to asteroids could also utilize electric propulsion due to their weak gravitational field and small size. The last major category of electric propulsive thrusters is electromagnetic. The thrusters use a combination of electric and magnetic body forces to accelerate particles to high velocities, creating a momentum exchange, and producing thrust.
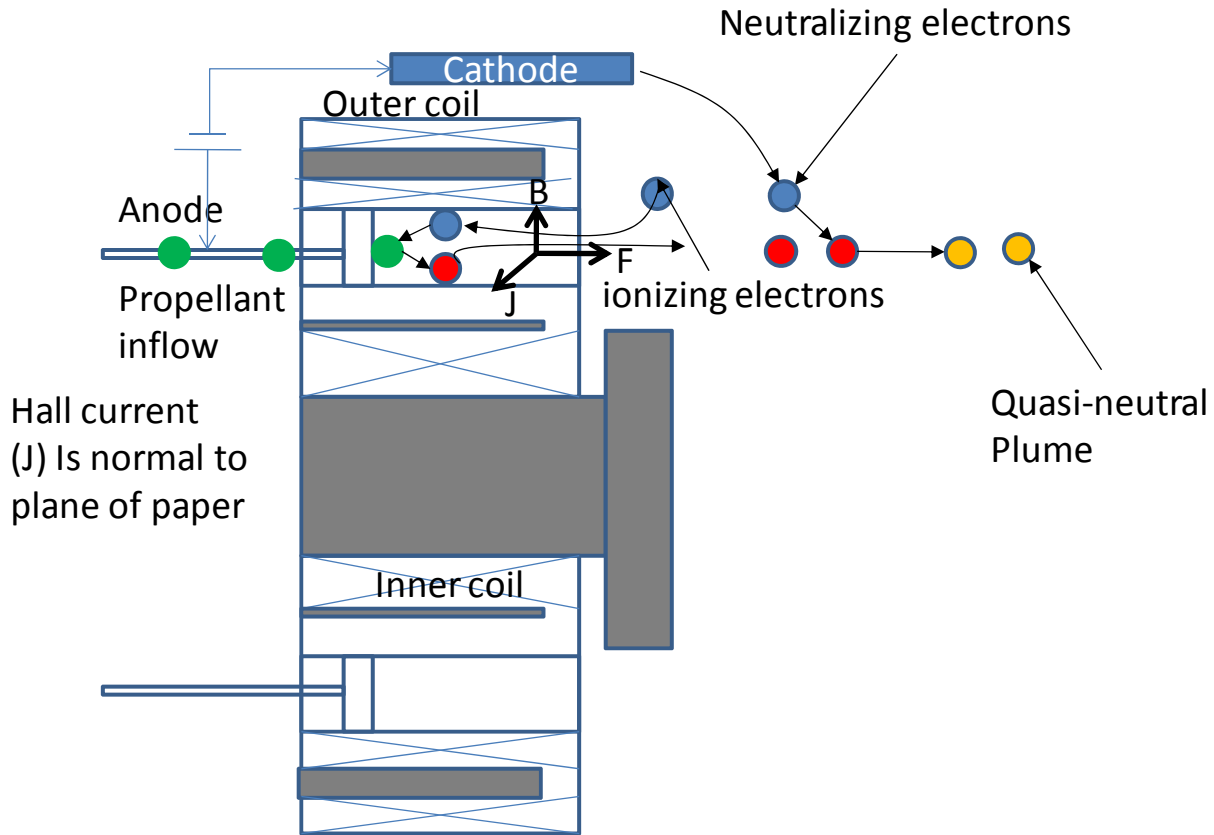
Figure 2. Hall thruster with external cathodes, based on Hofer [7]

Electromagnetic

The electromagnetic thruster types include the PPT, μPPT and magneto-plasma dynamic

(MPD) thrusters. These thrusters operate through electrical ionization of the propellant and

acceleration through external or internally produced electromagnetic fields. In the case of the

MPD thruster, they are really an arc-jet thruster with an electromagnet surrounding the nozzle to

aid in acceleration of the plasma and exhaust products through the Lorentz force once they

become ionized. A schematic of the operation MPD and PPT is shown in Figure 3.
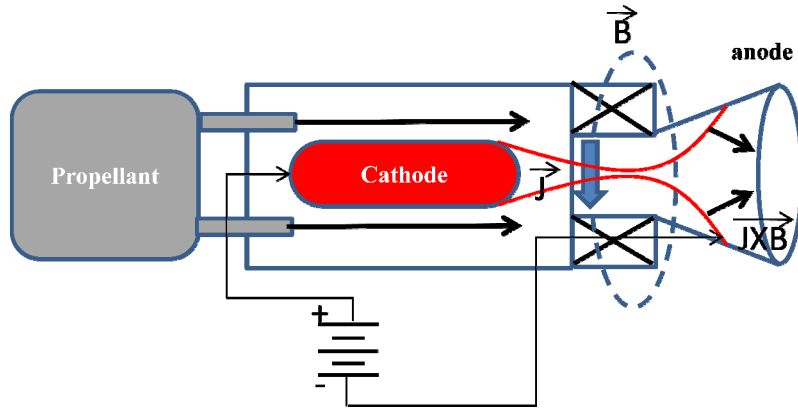
Figure 3. MPD thruster operation

For the PPT and µPPT, the cathode and anode create a strong electrical field eventually resulting in arc formation once the potential is above the breakdown voltage of the material (Teflon™). This arc ablates some of the Teflon™, surface. These particles pass through the arc and are ionized. Self-induced electromagnetic fields accelerate the ionized Teflon™, electrons and bits of cathode and anode out of the thruster. Through the Lorentz force, the thruster produces a momentum exchange producing thrust by pushing back on the electromagnetic field. The electrons and ions will have opposite charge and will spin in opposite directions after leaving the thruster but then come together once further away to form quasi-neutral plasma, thus eliminating the need for an external cathode to neutralize the exhaust plume, as required for Ion and Hall thrusters. A simplified diagram of a PPT is shown Figure 4.
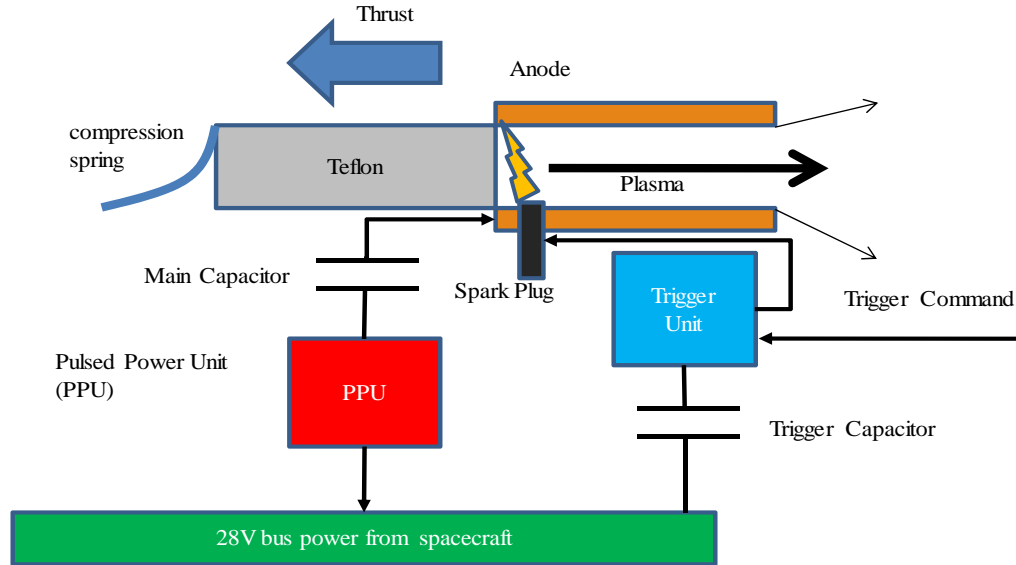
Figure 4. Schematic of Pulse Plasma Thruster, based on Wie [9]

PPTs and µPPT vary significantly in their structure because of the different sizes and applications. The PPT normally has a spring fed propellant system, keeping the propellant near the location of the arc so it can be ablated and ionized by the arc formation. The larger PPT also has a spark igniter or spark plug to reduce the amount of power needed for initial arc creation. Once this arc is established, it can be maintained at a much lower voltage level than the initial trigger spark. The larger size of the PPT allows them to be slightly more complex, but also require higher power levels than µPPTs. PPTs were developed first, then µPPTs afterwards by AFRL Propulsion Directorate at Edwards AFB, CA in 1997 [8].

The µPPT design is much simpler than the PPT. First, it does not require a spring to keep the propellant in contact with the arc face, because as the electrodes erode they maintain a spark level with the remaining electrodes and propellant surface. The electrodes and propellants are circular in cross-section for the µPPT and come in two or three electrode variants. The two-electrode variant shown in Figure 5 has just the cathode and anode. These have since evolved to the three (cathode, inner electrode, anode) electrode configuration for efficiency and power

11

generation requirements for arc formation. The inner electrode acts as an improvised spark plug

providing a seed arc and plasma thereby reducing the amount of voltage to start arc creation.

Once created, the flow of electrons can be sustained at a lower operating voltage during thrust

generation.
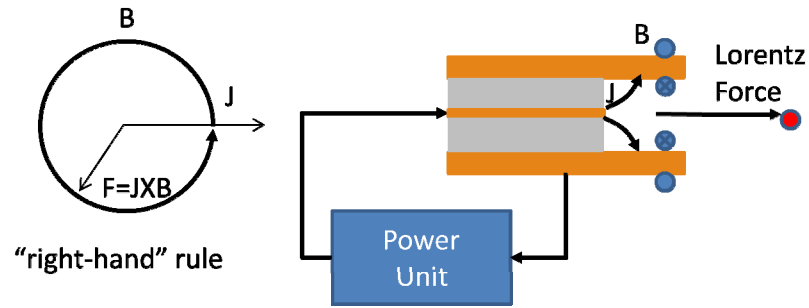
Figure 5. Basic 2-electrode micro-PPT operation, based on Burton [10]

The relatively simple design and low power consumption relative to other types of

electric thrusters makes them an ideal candidate for use on some micro, nano and pico satellites.

For the PPTs and µPPT, one of the biggest losses in efficiency comes from the conversion of

electrical energy into thrust. The ablation of Teflon through heating of the surface does not

produce a strongly ionized gas form of Teflon until it interacts with the arc itself. Double or

triple ionization reduces the overall efficiency of the thruster, because of the removal of more

electrons from one ion, instead of producing more ions. The efficiencies range from about 10%

for µPPT up to about 90% for ion and hall thrusters [3]. For electrical thrusters, the energy

production capability of the power plant limits the energy to create/accelerate ions in addition to

the associated electromagnetic efficiencies of acceleration and ion production itself. On a large

satellite, kW of electrical power may be available in the form of Radio-Isotope Thermal

Generators (RTG) or solar cells. However, for smaller satellites like CubeSats, the power

generation may only be in the range of watts or hundreds of watts. This low available power is one of the main reasons µPPT have become an attractive option.

The Isp of PPTs and µPPTs is typically around 800-1000s [3]. Though they have a lower Isp than their electrostatic or hall thruster counterpart, their simple design along with lower power requirements make up for any disadvantage they may have in Isp for nano and pico satellites. Several spacecraft launched commercially, or as part of a tech demonstration employed PPTs and µPPTs propulsion devices onboard.

History and Use of PPTs and µPPTs on small satellites

The devices are perfect for nano (1-10 kg) and pico-satellites (0.1-1 kg). Many of these satellites require thruster systems with high performance (Isp) and lower power consumption. Because these satellites are very small, the perturbations caused by the impulse of chemical systems can often be significant in comparison to the satellites inertia. The larger thrust to mass ratio for smaller satellites can effectively change the orbit parameters of that satellite enough to interfere with intended orientation of the satellite and would be most notable in attitude changes for the satellite where it may possibly spin in its orbit. However, µPPT are perfect for this type of satellite because the impulse bits are in the range of 10 to 200 µN-s.

The first PPT was flown on the Zond-2 spacecraft in 1964 launched by the former Soviet Union [11]. The first US launched PPT was onboard the LES-6 mission in 1968. In 1976, the LES-8 & 9 satellites tested PPTs for use as station-keeping devices. PPTs have also found application for drag compensation for satellites typically below 2000 km in altitude, (above 200 km other influences dominate, e.g. solar wind, third body effects, and photonic pressure) [12].

The PPT and µPPT were designed to fill a niche for the small satellite enterprise, catering to nano and pico-satellites. The University of Washington's Dawgstar satellite used

PPTs in formation flying experiments. The United States Air Force Academy's FalconSat III satellite used three µPPTs for two-axis orbit stabilization [13]. As the demand for smaller and more precise propulsion systems increase, µPPT research will continue to be very valuable to the commercial/government satellite ventures.

II.   Literature Review

The purpose of this chapter was to provide relevant operating principles and results of research to date completed on the PPT and µPPT devices and implications to the research topic of this paper. The chapter begins by examining the physical principle and physics behind the operation of the PPT and µPPT. What is discussed next are the relevant equations needed to analyze the circuitry of the PPT and µPPT. Afterwards, the GG-µPPT circuit boards are introduced. From there, the efficiency of the PPT is discussed, and finally, the types of failure modes encountered in previous research is presented. Let us look at the operation of the PPT first and then the µPPT.

Pulsed Plasma Thruster and Micro Pulsed Plasma Thruster

The Pulsed Plasma Thruster or PPT is the predecessor to the µPPT. It is a larger device and slightly more complicated, requiring the use of an igniter and spring to maintain the Teflon™ against the location where the arc is likely to form. The thermal ablation caused by the arc does not decrease because the Teflon™ has receded as it is consumed to produce thrust (Figure 4). The PPT being larger requires more power, but is also capable of producing thrust in the µN to mN range. The larger propellant face area exposed to the arc and plasma sheath created in the process of ionization results in the higher thrust levels..

The µPPT developed by AFRL at Edwards AFB, is finding promising uses on state-of-the art, smaller satellites. The limitation onboard energy production is the biggest constraint of

propulsion systems on these spacecraft. The μPPT is a simple, robust way to perform station

keeping maneuvers and precise pointing movements. The μPPT thruster shown in Figure 5 is a

two-electrode μPPT, and was developed prior to the three-electrode μPPT. The addition of the

third electrode changes the operation from the two-electrode design as shown below in

Figure 6. The inner electrode functions much like the spark initiator for the large scale

PPT. This configuration has several advantages over the two-electrode design in terms of break

down voltage and power requirements are concerned requiring less of both to operate.
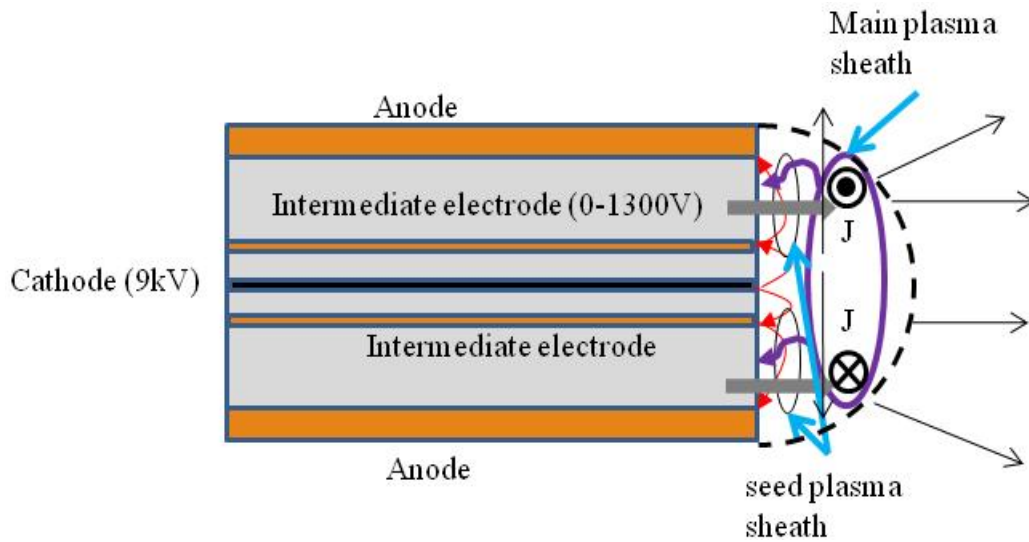
Figure 6. Three electrode μPPT operation

Figure 7, (a) shows the electrical connection for a modern three electrode μPPT with

electrical connections pulsed power unit (PPU) [14]. The trigger capacitor provides just enough

energy to start seed plasma as the arc ablates and ionizes the inner annulus of Teflon™. The

voltage potential of the trigger capacitor must be very high, in order to overcome the dielectric

breakdown rating of the Teflon™ surface. The electrical potential between the trigger capacitor

and ground is around nine kilovolts. The impedance due to the resistor in the trigger circuit

controls the current in the trigger circuit, and prevents discharge of the main from occurring too

early or too late. This discharge then collapses the circuit, and the main capacitor discharges,

producing an arc that jumps from the inner electrode to the outer electrode or anode, ablating and ionizing the outer ring of Teflon™   This is the portion of propellant producing the most thrust. The electrodes are made of copper, because of its malleability, electrical conductivity and heat dissipation properties.
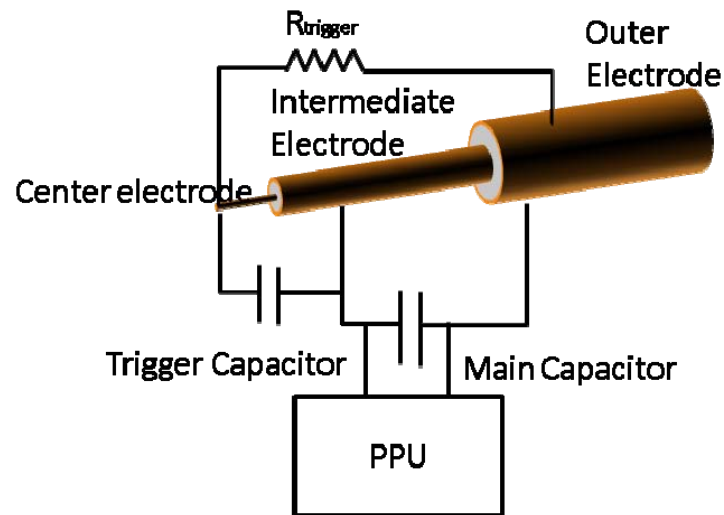
(a) Three-electrode µPPT, based on Spanjers [14]
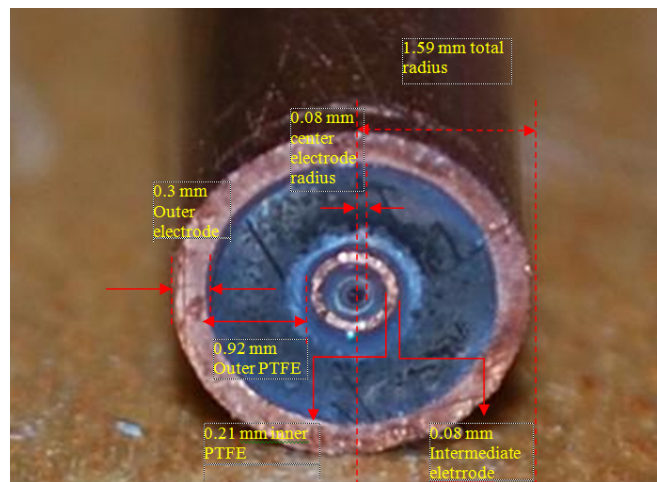
(b) Three-electrode µPPT, taken from Selstrom [13]

Figure 7. 3-electrode µPPT electrical connections and construction

A picture taken by Captain Jeremy Selstrom [13] shown in (b) of Figure 7 shows a close up of the µPPT and the approximate dimensions of the type used in his research.

Previous μPPTs were originally of the two-electrode design as shown in figure 6. More recent designs use a three-electrode configuration. This design has 3 significant advantages over the two-electrode design. First, the energy of the main discharge has less shot-to-shot variation decreasing the probability of carbon accumulation buildup on the propellant face [14]. Second, the seed ionization produced from the cathode and inner electrode greatly reduces the voltage required for the main discharge, which produces the larger plasma. Research indicated the discharge voltage could be reduced from 40kV to 3kV for a ¼-in μPPT if a third or intermediate electrode was designed into the thruster [14]. This significantly reduces the design demands on the PPU. Third, the design is more robust to short term increases in voltages required for initial trigger discharge and therefore arc formation.

Electrical Circuitry and Operation

The GG-μPPT firing sequence is very similar to the operation of a Gatling gun machine gun, or distributor cap in an automobile. In a Gatling-Gun, when the barrel rotates it collects a round and as the round rotates, it comes into contact with the firing pin, which strikes the back of the round firing the bullet. As the barrel continues to rotate, the empty shell is ejected and another is fed into the barrel. This design allows multiple rounds to be fired from the gun very quickly, and still prevent the barrel from getting to hot. The earliest designs required manual cranking to operate. Modern versions are powered with electric motors and are gas/liquid cooled because of the extremely fast firing rate.

A distributor cap in an automobile functions in a similar way. A timing belt is attached to a pulley that rotates the shaft that is timed to provide a spark to the specific cylinder 1-8 for example in a V-8 engine when the piston is near coming close to top dead center (TDC). As the piston nears TDC the points and condenser, which is just a capacitor provides a burst of energy

to the specific spark plug in the amount of about 100mJ of energy. This energy is enough to

ignite the gasoline-air mixture vapor causing rapid combustion and expansion forcing the

cylinder back down and providing power to the wheels via a transmission and drive shaft.

The first step in operation of a μPPT is to produce the high voltage potentials necessary

for arc formation. This voltage potential is accomplished through a resistor-inductor-capacitor

circuit or RLC circuit. A basic schematic is shown below in Figure 8; the diode prevents the

current from flowing backwards. The circuit allows the use of smaller voltages in the 5-28V

range for which a small spacecraft or satellite power bus provides. This energy is stored in a

series of capacitors allowing a large charge accumulation to build up, and therefore a large

voltage potential to be produced as each switch in the circuit closes. When the last switch closes,

the total accumulated charge is discharged over a period of about 20μs [1]. This short discharge

time results in a very large current flow (on the order of kilo-Amps) and a current density of

MA/m^2. The current flow, J (Amps) through a capacitor, resistor, and inductor is related to the

voltage via the following equations:

$$J = C\frac{dV(t)}{dt}\text{(Capacitor)} \tag{1}$$

Where C is the capacitance in Farads dV/dt is the change in voltage per unit time.

$$J = \int_{t_o}^{t} \frac{V(t)}{L}dt \text{ (Inductor)} \tag{2}$$

V(t) is the voltage at time t, L is inductance in Henries, and t_o and t are the limits of integration

$$J = \frac{V(t)}{R}\text{(Resistor)} \tag{3}$$

 R is the resistance in ohms. The capacitor and Inductor are energy storage elements, where the

resistor is a purely dissipative element. Using Kirchhoff's voltage laws and Thevenin's theorem,

the voltage and current flow across any element or node in the circuit shown in Figure 8. The

18

differential equation that governs an RLC circuit can be written in the form of a second order

homogeneous differential equation [15]:

$$L_o \ddot{Q} + R_o \dot{Q} + \frac{Q}{C} = 0 \qquad (4)$$

where R_o is the overall resistance of the circuit, with initial conditions $Q=Q_o$, $J_o=-Q(0)=0$ at

t=0. The solution has two forms. For $C < \frac{4L_0}{R_o^2}$, there is a damped oscillatory behavior, while for

$C > \frac{4L_0}{R_o^2}$, the current pulse is overdamped. In general for the under-damped case, [15]

$$Q = \frac{Q_o}{\omega\sqrt{L_o C}} e^{-\frac{R_o}{2L_o}t} \sin(\omega t + \delta)$$

$$J = -\dot{Q} = \frac{Q_o}{\omega L_o C} e^{-\frac{R_o}{2L_o}t} \sin(\omega t) \qquad (5)$$

$$\omega = \left(\frac{1}{L_o C} - \frac{R_o^2}{4L_o^2} \right)^{\frac{1}{2}}$$

For the over-damped case, [15]

$$Q = \frac{Q_o}{\omega'\sqrt{L_o C}} e^{-\frac{R_o}{2L_o}t} \sinh(\omega' t + \delta')$$

$$J = -\dot{Q} = \frac{Q_o}{\omega' L_o C} e^{-\frac{R_o}{2L_o}t} \sinh(\omega' t)$$

$$\omega' = \left(\frac{1}{L_o C} - \frac{R_o^2}{4L_o^2} \right)^{\frac{1}{2}} = i\omega \qquad (6)$$

$$\delta' = \tanh^{-1}\left(1 - \frac{4L_o}{R_o^2 C} \right)^{\frac{1}{2}}$$

The shorter the fall time of the current, the less propellant used, resulting in higher

discharge densities allowing more ionization of the propellant, and producing more thrust and

higher Isp.. A RLC circuit with capacitors in parallel provide the momentary, instantaneous

power required for propellant ablation and ionization as shown in Figure 8. The circuit operates in the following way. Initially, the first switch is closed allowing the voltage to build in the first capacitor. Then, the second switch is closed allowing the voltage to build in the second capacitor through the inductors, storing energy in the form of a magnetic field, and does not allow an instantaneous changes in current. Inductors are often used in circuits as chokes to reduced currents produced be by AC voltage sources. These components work together to produce a very large voltage with the high currents necessary for ablation and ionization.
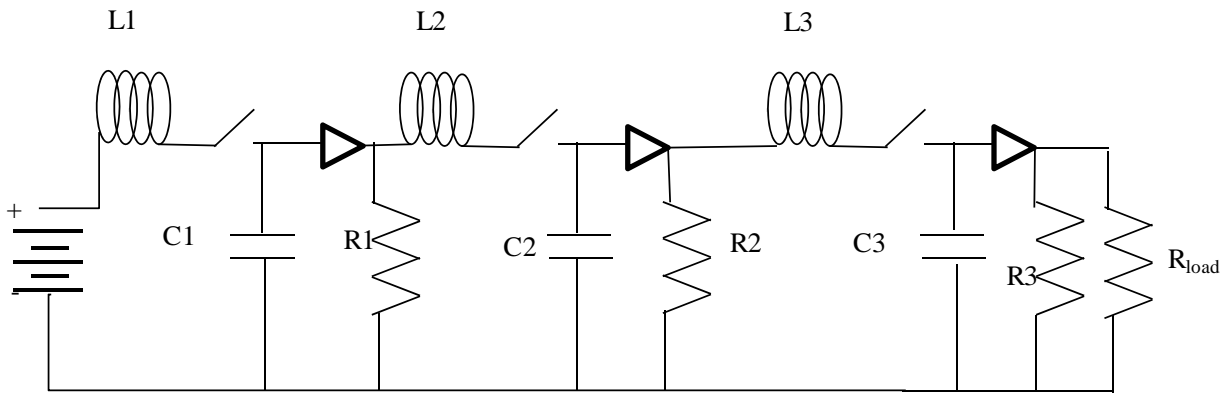
Figure 8. High-voltage RLC circuit

In the GG-µPPT, a high-voltage (HV) 10 kV multiplier provided the necessary voltage for firing each stick for operation. The main capacitor, high voltage switch board, external I/O board, processor board, power input board, and high voltage generation board are the major components of the GG-µPPT module. The bundles of µPPTs, arranged in a GG pattern, is shown in (a) of Figure 9 and the component part in (b) of Figure 9. All these components work together to allow sequential firing of each µPPT at various frequencies.

(a) Associated stick number and arrangement of μPPT sticks Gatling-Gun Configuration

(b) Various boards of GG-μPPT module required for operation
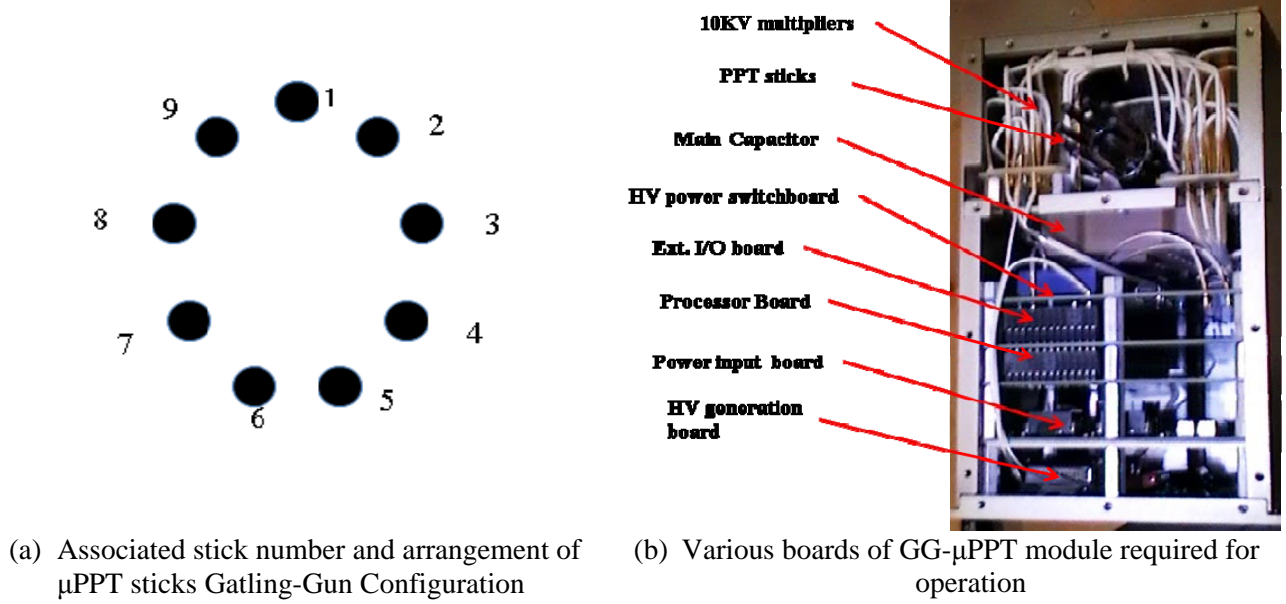
Figure 9. Gatling-Gun configuration and module

Physical principles and Theory

The physical principle of operation for all thrusters starts with momentum conservation. For electric thrusters, the Lorenz force describes the acceleration mechanism [3].

$$m_i \frac{du_i}{dt} = q_i (\vec{E} + \vec{u}_i \times \vec{B}) + \sum_k P_{ik} \tag{7}$$

where m_i is the mass of the ion, du_i/dt is the acceleration of m_i q_i is the particle charge (Coulombs), E (V/m) is the applied electric field, B is the magnetic field (T), and P_{ik} is the collision force per particle. However, we can simplify the momentum conservation for μPPTs to just the contributions from the Lorentz force. The electrostatic force, $q\vec{E}$ does not provide the majority of the acceleration of the ions generated by the arc. The magnetic component $q\vec{u} \times \vec{B}$ imparts a significant force on the plasma, accelerating the ionized mass to speeds exceeding 10,000 m/s for the power and dimensions of these μPPTs.

$$F = q(\vec{E} + \vec{u}_i \times \vec{B}) \tag{8}$$

The effective exit velocity of the ionized Teflon™ is calculated in terms of the radius of the anode, cathode, ablated propellant mass flow rate, thrust, efficiency and current (J) through the following equation [16]:

$$u_e = \frac{F}{\eta \dot{m}} = \frac{1}{\eta} \frac{\mu_o}{4\pi} \ln\left(\frac{R_a}{R_c}\right) \frac{J^2}{\dot{m}}$$

(9)

This equation factors in the efficiency associated with the self-field magnetic field produced when the Teflon™ interacts with the plasma, but is the same equation as described by Jahn with efficiency factored in [15]. The term μ_0, is the permeability of free space $4\pi \times 10^{-7}$ H/meter or N/A^2, J is the current (Amps), R_a is the radius of the anode (m), R_c is the radius of the cathode (m), $\dot{m}$ is the mass flow rate (kg/s), η is the efficiency, and F is the thrust (N). Once the exit velocity is known, I_{sp} is determined through the equation:

$$Isp = \frac{U_e}{g_o}$$

(10)

,where g is the acceleration due to gravity (9.81m/s), U_e is the exit velocity of the ions.

Efficiency

The electro-thermal ablation process of the propellant inherently includes significant loss, resulting in PPTs only able to achieve 10-20% efficiency [3]. The total efficiency written in terms of identified losses is [17]:

$$\eta_o = \eta_{PPU} \eta_{trans} \eta_{sh} \eta_{heat} \eta_f$$

(11)

Where η_o is the overall efficiency, η_{ppu} is the power processing unit efficiency, η_{trans} is the transfer efficiency, η_{sh} is the sheath efficiency, η_{heat} is the heat loss efficiency and η_f is the frozen flow efficiency. The η_{sh}, η_{heat}, η_f efficiencies are often expressed as the acceleration efficiency, η_a for the thruster. This term combined with η_{trans} is thruster efficiency. The diagram

below shows the relationship more clearly. Total thruster efficiency can also be determined based on the exhaust or jet power by measuring thrust and the input power supplied. However, multiple losses including waste heat generated by the capacitor and electronics are hidden in this approach and are only attributed to the PPU efficiency. The loss processes and associated efficiency statistics are graphically shown in Figure 10.
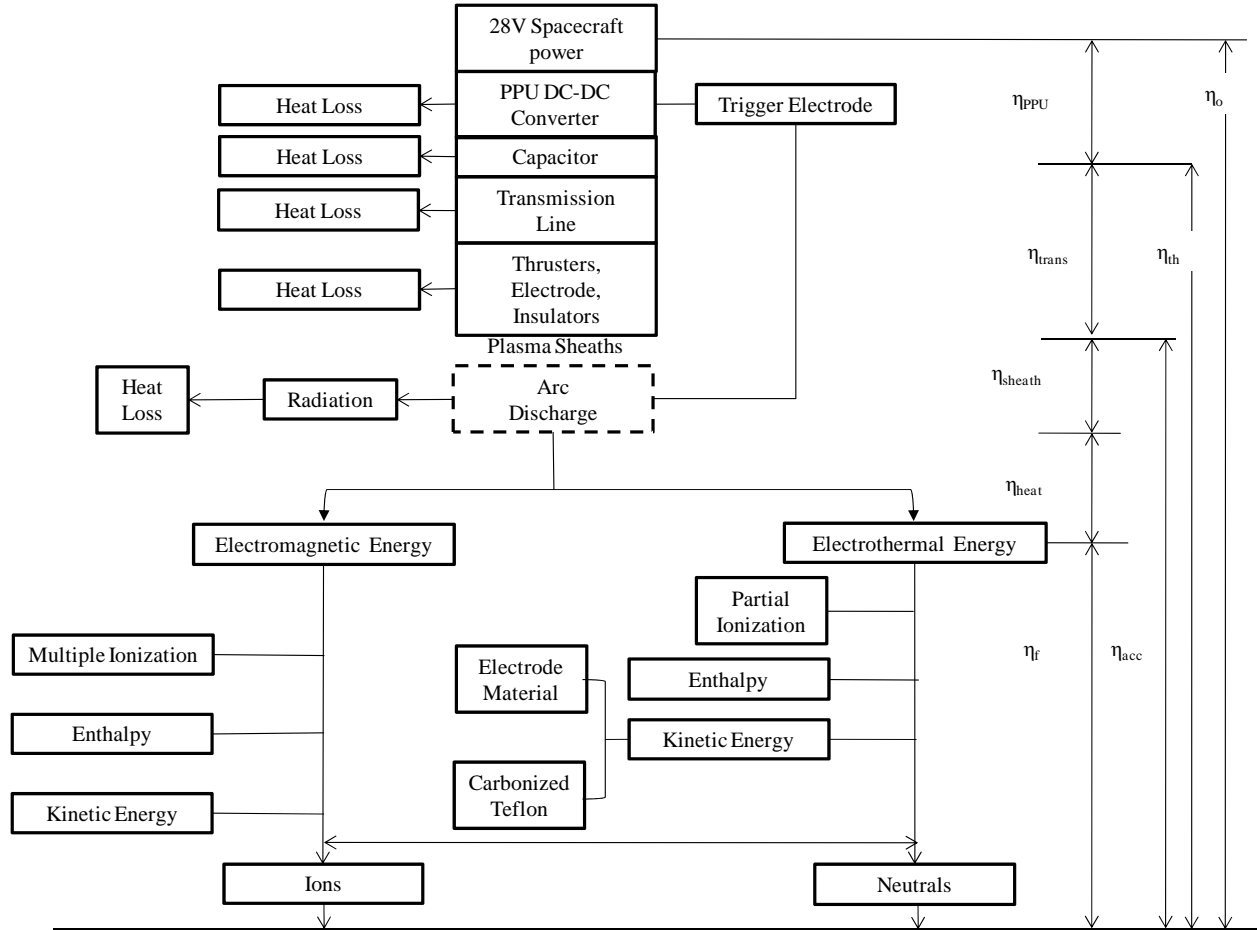
Figure 10. Process efficiencies, based on Bluhm [17]

The exhaust kinetic energy has two major parts, one fast moving ionized mass, m^+, and the other slower non-ionized, neutral mass, m_n, for the thruster efficiency [13]:

$$\eta_t = \frac{\frac{1}{2} m_+ u_+{}^2 + \frac{1}{2} m_n u_n{}^2}{E_o} \tag{12}$$

Where m^+ and m are the masses of the ions (F^+ and C^+) and neutral particles in kilograms respectively, u^+ and u are the exhaust speeds of the ions (m/s) and neutral particles, and E_o is the input energy into the system. Alternatively, this can be written in terms of parameters readily measured from an experiment such as thrust, capacitance and mass flow rate, and firing/discharge frequency [15].

$$\eta_{th} = \frac{F^2}{\dot{m}\, \nu C V^2} \tag{13}$$

where $\dot{m}$ is the mass flow rate in kg/s, ν is the frequency of the discharge in Hz, C is the capacitance in Farads, and V is the voltage supplied to the discharge capacitor.

The total impulse of the thruster is a combination of the impulse produced from the ions and neutrals at their respective velocities.

$$I_{bit} = m_{ions} + m_{neu} \tag{14}$$

$$I_+ = m_+ + m_+ \tag{15}$$

$$I_n = m_n + m_n \tag{16}$$

$$\frac{m_+}{m_n} = \Phi \tag{17}$$

The ratio of the ionized particles to the neutral particles is designated by Φ, important in the efficiency of the thrusters. For different materials and power levels, the ionization fraction varies considerably between zero and one. Multiple ionization is also possible for the same atomic structure, where atoms can be doubly or even triply ionized during their interaction with the electric field. This last term assumes a normal or Maxwell distribution, which is not a good assumption for neutrals and ions. To do this, the individual efficiencies contributing to the overall efficiencies must be solved for. The η_{PPU} can be determined from the energy transferred

to the capacitors from the input power. This efficiency is normally between 80-93% [13]. To

determine the η_{trans}, the impedance of the PPU and the total circuit, R_{total} must be known and

from this the efficiency is calculated by taking the ratio of the two and subtracting from one.

$$\eta_{heat} = \frac{R_{PPT}}{R_{total}} \tag{18}$$

The efficiency of the plasma sheath can be determined from the following equation,

$$\eta_{sh} = 1 - \frac{Vsh}{V_{PPT}} \tag{19}$$

Where V_{sh} is the sheath voltage drop and V_{PPT} is the voltage supplied to the PPT. The

heat efficiency is determined by looking at the amount of heat generated from the arc to the heat

lost that does not result in ablation of the propellant,

$$\eta_{heat} = 1 - \frac{E_{loss}}{E_{arc}} \tag{20}$$

Where E_{loss} represents the energy lost that does not produce ablation and E_{arc} is the

energy in the arc, which can be determined from the energy of the capacitors, $\frac{1}{2}CV^2$. The

frozen flow efficiency, η_f, can be determined from the speed of sound and the total enthalpy of

the ions, which is determined from a lookup table for the material. The equation is,

$$\eta_{heat} = \frac{u^2}{h_o} \tag{21}$$

Research performed by Selstrom (USAF) while at the Air Force Institute of Technology

shows the effect of thruster efficiency and lifetime as the thruster nears End of Life (EOL) [13].

As the thruster operated, the thrust and efficiency decreased as shown in Table 1. The reduction

in performance is due to the larger carbon micro-particles accumulating between discharges.

The thrust is relatively constant as shown in Table 2 and Figure 11. The decreased efficiency but

constant thrust would mean that more propellant is coming off the thruster in the form micro-

particulates instead of the ionized atoms that are accelerated by the Lorentz force.

Table 1. Efficiency as function of firings

Pulses	1000	5000	10000	30000
Efficiency (%)	68.63	48.19	48.37	29.35

Table 2. Thrust as a function of firings

Pulses	0	1000	2500	5000	10000	15000	20000	25000	30000	35000
Thrust(μN)	195.40	215.92	180.27	152.83	163.08	186.15	178.16	188.18	158.86	191.73
Standard Deviation	14.20	18.58	47.01	58.11	10.30	30.27	20.44	15.61	12.09	7.41

$y = -0.0003x + 184.87$
$R^2 = 0.0315$
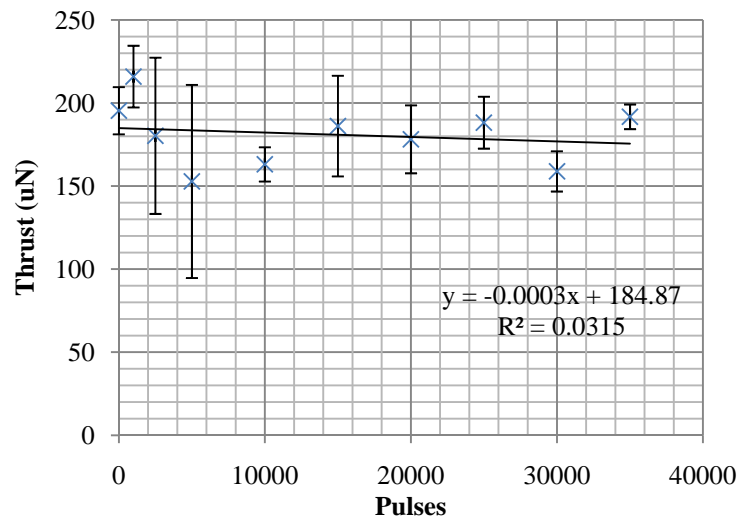
Figure 11. Thrust variation with firings

The µPPT undergoing testing stopped functioning at about 36,000 pulses due to damage

to the working surface of the thruster. Since the thrust is nearly constant after the initial phase of

operation and the efficiency decreases, the conclusion of more mass ejected from the thruster is

in the form of neutral particles is supported. These particulates do provide a momentum

exchange as they leave, but are due to their larger mass and slower velocity with Isp in the range

of 25-35 s, instead of the 800-1000s resulting from ionization and expulsion via the Lorentz

26

force. The premature failing of the µPPT stick, illustrated one of the major failure modes of this type of thruster. This mode is the deposit of carbon to the propellant surface during thruster operation.

Failure Modes

Particulate Ejection and Carbonization

One of the major factors affecting the efficiency is the late-time vaporization and carbon build up on the µPPT as the surface cools between pulses [14]. The gas products from thermal ablation form a carbon layer requiring a larger potential to pulse. Contamination studies of µPPT by Kesenek [18] reveal the carbon deposits in detail as shown in (a)-(c) of Figure 12.
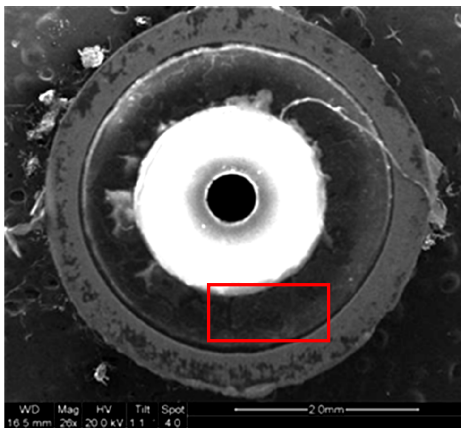
(a) 20X magnification Scanning Electron Microscope (SEM) image of a µPPT stick,
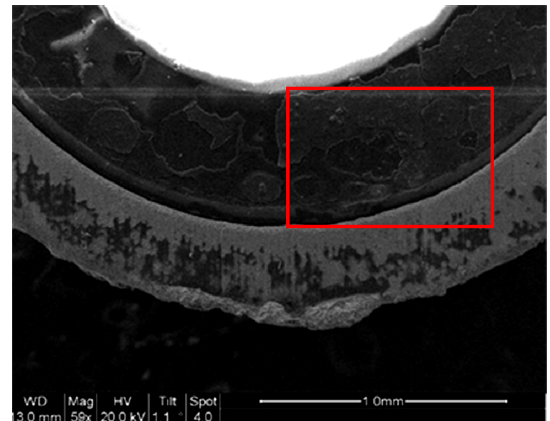
(b) 59X magnification, flaky patches of carbon deposit are clearly visible.
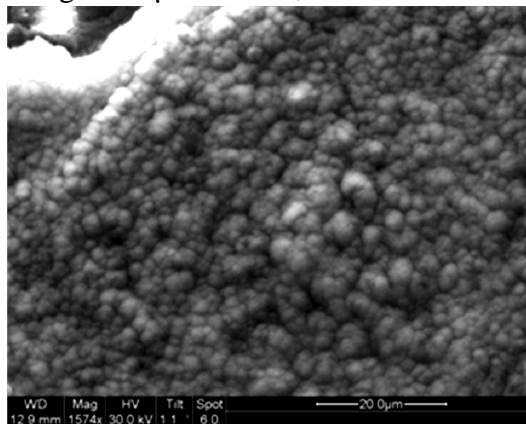
(c) 1574X magnification showing bumpy 'granules' of carbon on Teflon™ surface

Figure 12. Carbon Buildup, taken from Kesenek [18]

Experiments and analysis conducted by Keidar et al, indicates the relationship between the energy supplied and the amount of particulate that returns to the surface of the Teflon™ in the form of carbon deposits [1]. If the current density is low, the higher the ratio of returning particle flux to ablated flux of Teflon™, shown graphically below in Figure 13. As evident from the graph, the higher the current density results in more of the ablated Teflon™ being ionized and results in a lower returning particle to ablated particle ratio.
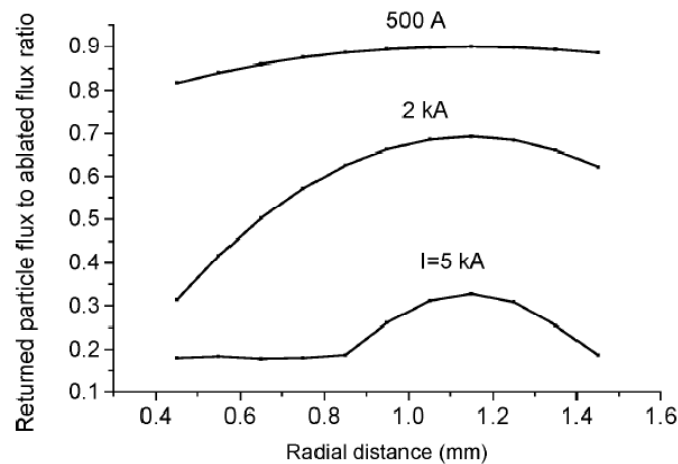
Figure 13. Particulate/Ablation ratio as function of current density, taken from Keidar [1]

Uneven Electrode Erosion

The GG-μPPT can also fail through the improper erosion of the electrodes. If the electrodes are cut with a tool leaving ragged edges on the surfaces of the electrodes, the charge densities will accumulate on these surfaces because the electric field will concentrate at these micro-protrusions. The uneven erosion results in the arc being to too far from the Teflon propellant to cause sufficient ablation through radiation and convective processes. If the electrodes erode slower than the propellant, the arc formation will be too high above the surface to ablate propellant effectively, through the electro-thermal process, and will result in significantly reduced thrust or will not operate. If the electrodes recede faster than the

propellant, the cathode may be unable to see the anode and the result is poor operation and/or charring of the propellant, because of the large power required to jump the gap. A diagram is shown below in Figure 14. Another failure mode is due to uneven arc formation or 'spokes' that dig a channel resulting in uneven propellant utilization and ionization.
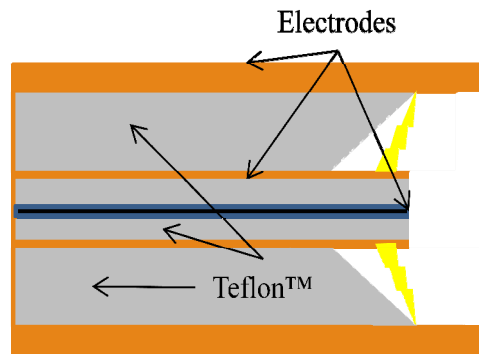
Figure 14. Uneven electrode erosion

Non-Uniform Discharge and Temperature Effects

This is another aspect of μPPT operation that is different from the large PPT. The larger PPTs were of rectangular cross section, so there was not a point concentration of the electrical current as there is in the coaxial μPPT. The temperature of the propellant increases significantly where arc convergence is larger. These arc spokes are seen if the energy of the pulse is too small [19]. The small energy results in non-uniform arc distribution, because the current will flow along the path that offers the least electrical resistance, very similar to the lightning strikes on earth during severe thunderstorms. The pattern can vary in both the radial and azimuthal direction [19]. The non-uniformity results in higher propellant ablation temperatures of the propellant and affects efficiency of the thruster.

The propellant utilization efficiency suffers directly as a result of this uneven propellant ablation and heating. Research conduct by Selstrom [13] indicates uneven ablation does indeed occur for the μPPT and as a result, the μPPT firing rate would vary. A channel was created in

the Teflon™ as a result of arc formation in a concentrated area. The non-ionized particles

emitted from the µPPT due to late-time ablation does contribute to thrust, robbing the efficiency

of the thruster, because these particles are not accelerated to velocities of 10-20 km/s by the

Lorentz force. These particles are more massive than the ions, but are only moving at sonic

speeds. They do not contribute significantly to the high Isp as shown in Table 3.

Table 3. Propellant Velocity versus Energy

Input voltage (Energy)	4 V (2 J)	5 V (2.7 J)	6 V (3.4 J)	7 V (4.0 J)	8 V (4.4 J)
Ave axial velocity (m/s)	215	256	345	270	258
Isp (sec)	22	26	35	28	26

Capt Seo Myeongkyo [20] in 2007 captured some images of the particles leaving the

three electrode µPPT to characterize the exhaust plume. The velocity of the particles emitted

ranged from 100-8076 m/s with 77% of all particles collected traveling below 300 m/s as shown

in Figure 15.
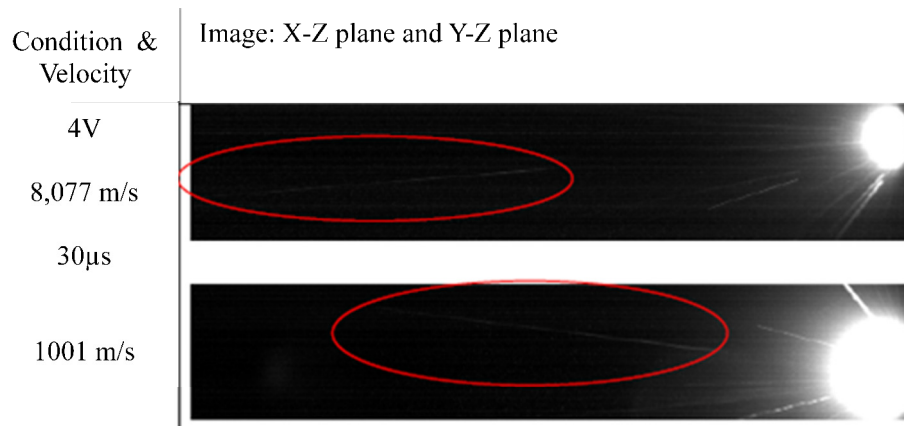
Figure 15. Fast particles from µPPT, taken from Myeongkyo [20]

The low efficiency of the µPPT can be attributed to the poor thermal ablation process and

non-ionization of particles ejected from the device. Though it does contribute to thrust, the

utilization efficiency would be higher more of the propellant is ionized before expulsion from the thruster. The theoretical efficiency of these devices could be as high as 60% [17]. Current performance is an order of magnitude smaller. The goal becomes how to vary the input energy, discharge time of the arc, and frequency of firing to optimize efficiency and propulsion from this particular device. The GG-μPPT is a collection of nine individual μPPTs, and should reveal the relationship between firing frequency, discharge energy and input power in more detail, because the electronics and their component properties can be controlled via a computer interface into the unit.

III.   Methodology

This chapter focuses on methodology and the process of calibrating and setup of the equipment in order to conduct the research. We begin by describing the facility and vacuum chamber where conduction of the experiment occurs. Then, there is discussion of the specific equipment and procedures of connection and calibration. Afterwards, we discuss the technique for getting the center of mass (COM), moments of Inertia (MOI) and physical parameters of the torsion balance. From there, the research discusses how to level the torsion balance and setup the calibration electrode distance. Then, we discuss the variables under the operator's control. Finally, we describe the planned test matrix and operating conditions under investigation. Let us begin by describing the facility at AFIT where this research took place.

The Geo-orbital Nano-Thruster and Analysis and Testing (GNAT) Laboratory at AFIT was the primary testing facility for the GG-μPPT research effort. The torsion balance required calibration for testing of the GG-μPPT. The available vacuum chambers are capable of reaching 10^{-8} torr [21]. The chamber used in this research was a horizontally mounted vacuum chamber by LACO^{TM} Technologies. The chamber pressure reached a low of 4.7×10^{-7} torr, or 0.47μtorr.

The vacuum chamber has front and side windows as well as feed-through (s) for high voltage lines and BNC connections for instrumentation, and test equipment. It is a cylinder roughly 0.61 m in diameter and 0.61 m in depth with a volume of 0.178 m^3. The chamber required little input from the user, and operated using a LabView™ interface. In order to ensure on-orbit like conditions, testing will occur below $2x10^{-5}$ torr, though $2x10^{-6}$ torr is preferred according the instruction manual for the thruster. Figure 16 shows a picture of the chamber used with the main viewport window facing the camera. Prior to beginning the research, several key pieces of equipment were required.

Equipment and Connections

The most critical piece of equipment used in this research was the torsion balance system, TBS manufactured by Busek™ Space Propulsion Company. Shown in Figure 17, is the torsion balance. The torsion balance consisted of a calibration electrode, an active damping electrode, a swinging arm to mount the thruster and its counterweight, a mirror for the laser displacement sensor or LDS, a mount for the LDS and micrometers to level the balance. This device can accurately measure μN forces produced by a μPPT. The LDS measured the linear travel of the arm as it rotates, and calibrated according to manufacturer specification sheets. The TBS also has an active damping system, but does not require use as long as the permanent magnet remains in place. The voltage required to operate the calibration electrodes above the noise floor present in the lab was set at 800V based on recommendations from Selstrom in his research [13].
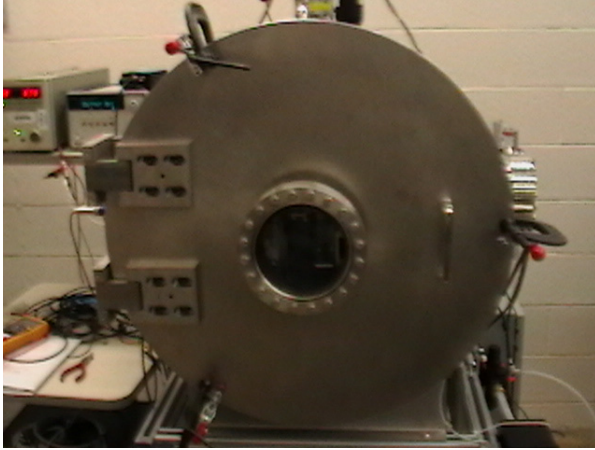
Figure 16. LACO Vacuum chamber
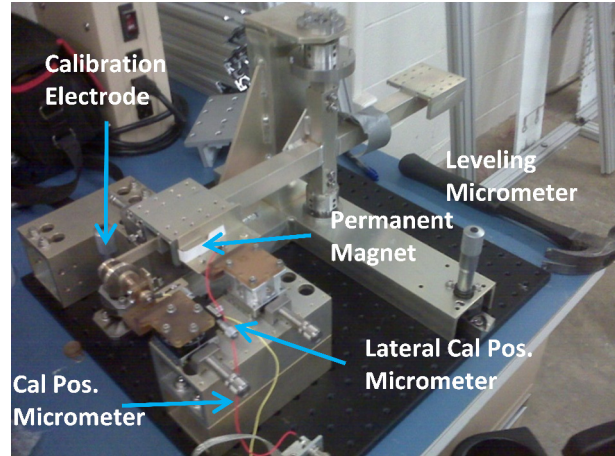
Figure 17. Torsion balance

The GG-µPPT shown in Figure 18 is a nine-stick array of 3.175 mm diameter 3-electrode

µPPTs. The GG-µPPT is a system that requires a power source capable of 10-20V at four amps

or about 40-80W peak in pulsed operation. However, keep in mind this power is pulsed and not

continuous. When the system is idle, it only draws about 8W. The GG-µPPT comes with a 25-

pin data cable and a 15-pin power cable that connects to the device on the top and bottom ports

respectively as shown in b of Figure 18. A re-programming port also exists on the interior for

software changes shown in b of Figure 18. The re-programming port allowed change of the

discharge energy from the main capacitor in the range from zero to 1300V. However, to

reprogram the thruster, removal of the side panel is required, and the high-voltage wires had to

be isolated and secured to prevent accidental discharge of the thruster in atmospheric conditions.

Once accomplished, the thruster was ready to be back into the chamber for further testing at the

new discharge energy condition set by the operator.
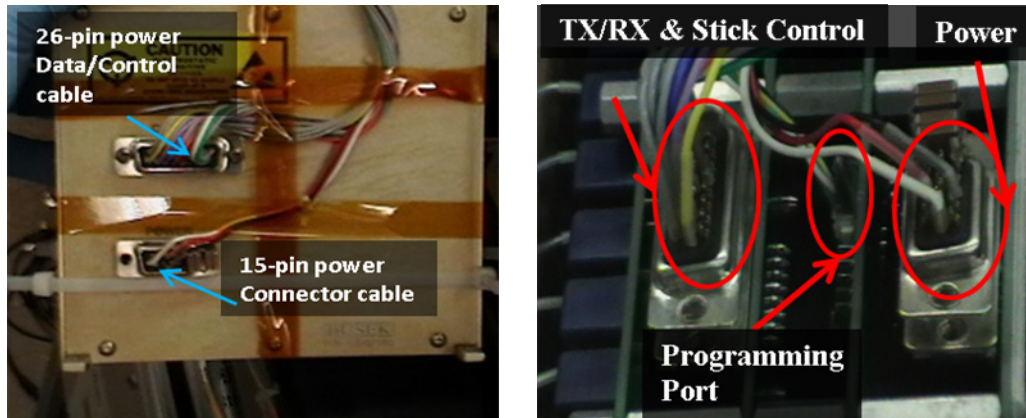
(a) Electrical connections control   (b) Programming connection port

Figure 18. External connections to the GG-μPPT

The next piece of equipment needed was the stick selector module that allowed the user

to change the firing frequency of the thruster sticks and control/enable which sticks are to fire.

The stick selector module can run off a nine-volt battery for internal power, or off external

power. Because of the long wait times for data processing, external power is the preferred power

supply method for the stick selector module. The center rotator knob controls the firing

frequency and the toggle switches enable or disable thruster sticks. The relay of status and firing

information from the GG-μPPT device to the computer requires the RS232 serial connection. A

LED on the side indicates power status. Shown in Figure 19, is the stick-selector module. The

large bundle of wires needed for GG-μPPT operation required attachment of a 'Cross' flange to

the top of the vacuum chamber in order to feed all of the connectors into the chamber. Due to its

length, the LDS tip is impossible to insert into the chamber any way other than straight down

from the top of the flange shown in Figure 20
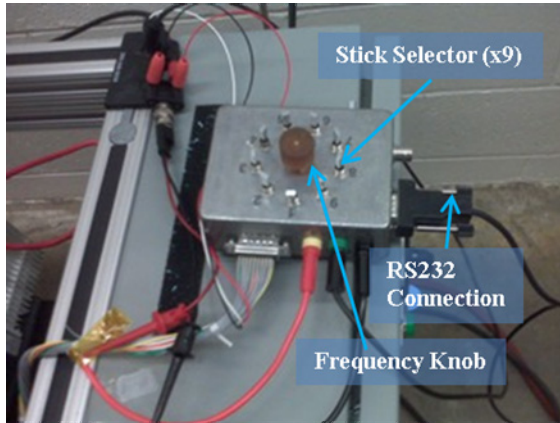
Figure 19. Stick selector module
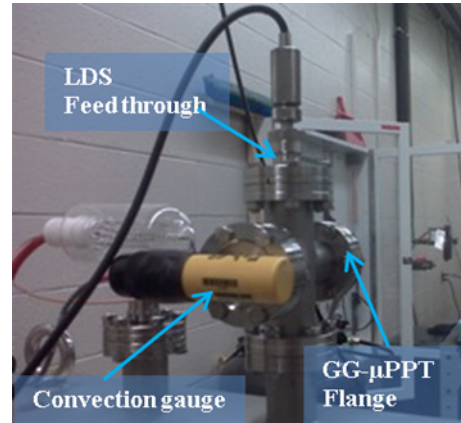
Figure 20. LDS/GG-μPPT feeds

An Agilent 54622D Mixed Signal Oscilloscope was used to collect the raw data coming from the LDS, and has multi-channel operation and digital/analog signal acquisition capability. The voltage output of the LDS was set in a range where the voltage output is a linear function of distance from the LDS tip to the reflecting mirror. To collect data, the output voltage of the LDS required connection to the oscilloscope via a BNC connector and the oscilloscope connected to a computer. As the thruster fires, it causes a small rotation in the arm which shows up on the oscilloscope as a change in voltage. Shown (a) of Figure 21 is the oscilloscope along with power supply(s) for the calibration electrode and the LDS box. The voltage changes due to thruster firing are in the mV range, so background noise is a concern as discussed in section four, results, and analysis. The focus now shifts to collection of system parameters and setup.
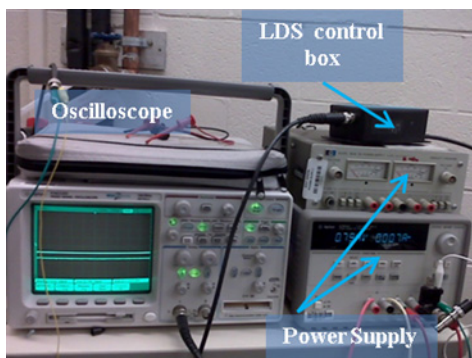
(a) Power for Torsion Balance and LDS

(b) Power supply for GG-μPPT

Figure 21. Agilent 54622D oscilloscope and power supply

Center of Mass and Physical Properties

Center of Mass

The first step prior to using the torsion balance was to obtain the physical properties of the thruster. A couple of ways to determine the center of mass of an object exist. The first and often simplest way is to attach the object to a slider able to hang freely under the influence of gravity. The hanging point is changed until the center of mass (COM) is directly in line with the hanging wire, assuming no disturbances are present, the object should be balanced, with the sum of the moments and forces equal to each other.

If the COM is not at the location of the tension of hanging wire, a net moment will tend to rotate the object about its hanging point as in Figure 22. If the mass of the object is uniformly distributed, then the COM is usually the geometric center of the object as well, but does not have to be. If the components of the thruster for instance are more massive on one side or another, the COM will shift from the geometric center. If it is desired to have the COM for all three axes, the thruster is hung from each of its principle axis and make adjustments until no moments in that axis exist.
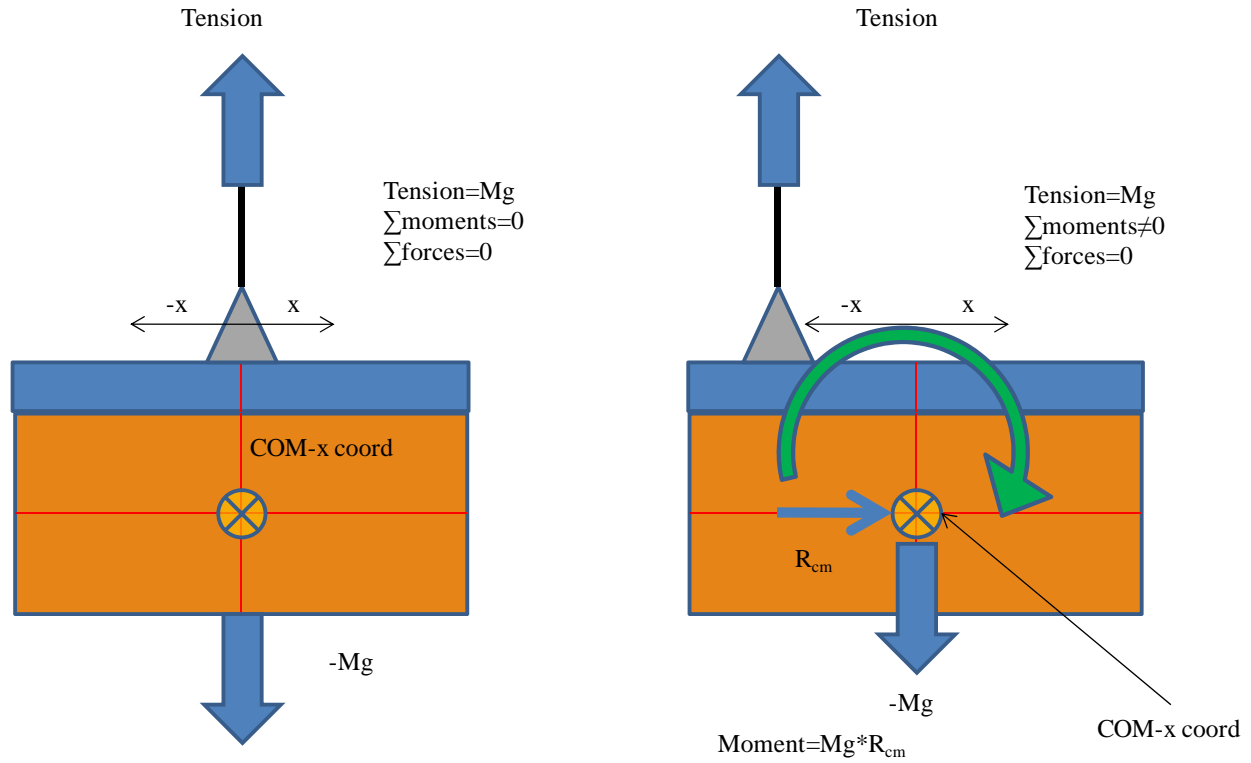
Figure 22. COM determination by hanging

Another way to measure the COM of an object is to place the object on a rail resting on two knife-edges fastened to a precision scale. First, the scales are placed a measured distance apart. The center of the rail was placed at the midpoint distance between the scales. The COM of the rail was determined by adjusting the location of the rail until the scales read the same value. The thruster was placed on the rail and moved back and forth until both scales read the same value to within a milligram of each other. The change in distance from the geometric center of the thruster along with the scale measurements allowed precise determination of the COM. Because of the transformers and various components, the COM was off from the geometric center by 0.5 mm. The knife-edge setup used in this research and the precision digital caliber to measure the dimensions of the thruster is shown in Figure 23.

(a) Digital scales with knife edge and rail

(b) Digital caliper for measuring distances

Figure 23. Knife edge/scales to determine center of mass

The scales were capable of reading to 0.0001 kg, (0.1 g) with a capacity of 6 kg. This process was repeated for each principle axis of the thruster. With the COM of the thruster known, the next task was to make physical measurements of the torsion balance itself and determine the moment arms of the thruster and counterweight.

Moment Arms

The next step prior to using the torsion balance is to characterize its physical dimensions, because these dimension were important in determine the moment arms of the thruster, counterweight, and location of the LDS sensor tip relative to the axis of rotation for the torsion balance, which is was designated zero for reference purposes. The length of the arm of the torsion balance was measured using a combination of measuring tapes and the calipers shown in Figure 23. The length of the torsion balance arm measured 0.476 m from end to end, with the center bar having a thickness of 25.4 mm. The base plates of the balance, which hold the counterweight and thruster are squares that are 38.1 mm. on each side. The distance from the center of one plate to the other is therefore 0.400 m.

Because of the wiring required to connect the thruster to its power supply, the radius of the thruster is not exactly the same as the radius of rotation for the counter weight. They differ by about 3.17 mm. The location of the LDS sensor was found by measuring the distance from the end of the balance arm to the center of the mirror, accounting for the diameter of the LDS

sensor tip. This The result is 0.22512 m for the LDS sensor tip and a radius of rotation of 0.200

m. for each arm if the counterweight is located at the center of each mounting plate. With these

values known for the balance, the next task was to determine the masses and moments of inertia

(MOI) for both the counterweight and thruster. The moment of inertia of the balance arm was

provided by Busek™.

Calculation of Mass and Moment of Inertia (MOI)

The mass of the counterweight and the thruster were measured directly using the same

precision scales used to determine the center of mass of the thruster. The next step afterwards,

was to figure out the MOI of both. The mass of the thruster with its stand was 1.9208 kg; the

mass of the counterweight with its base was 1.921 kg. These masses differ by only 0.2 mg. The

error associated with the difference in mass is only 0.01% of the total mass of each. The MOI

for both the counterweight and the thruster, can be calculated using the parallel axis theorem and

MOI formulas about the body axis of the counterweight and thruster. The thruster and counter

weight are both rectangular solids in by design, so this makes the calculation of the MOI

relatively simple. The MOI of a rectangular solid about its own axis of rotation, say the z-axis,

which we will call the height of the thruster and counterweight is:

$$I_z = \frac{1}{12} m\, (w^2 + d^2)$$
(22)

The terms w and d are the width and depth of the rectangular solid respectively. Once I_z

was determined, the parallel axis theorem was used and the total MOI was determined from the

equation:

$$I_{total} = I_z + mr^2$$
(23)

The term r is the radius of rotation from its body rotation axis to the desired axis of

rotation, and is equal to the radius between the center of the torsion balance and the COM of the

thruster or the counterweight in the X-Y plane. The moment MOI for the thruster using formulas above was 0.0791 kg-m^2 and 0.08037 kg-m^2 for the counterweight respectively. The MOI for the balance arm is 0.01692 kg-m^2 provided by Busek. The total MOI is just the sums of these which are equal to 0.17643 kg-m^2.

Calibration Pulse and Force Calculation

The torsion balance does not measure thrust directly, but calculates it through a comparison to a calibration pulse of known voltage and a force conversion factor that is a property of the geometric properties and spacing between the electrodes. Assuming the spacing between the electrodes is 1.0 mm, the force can be calculated using electromagnetic principles and modified equations for the attraction between two parallel, electrically conducting plates. In collecting data, a calibration pulse should be taken as frequently as possible to obtain more accurate results and calculations. These values can be statistically analyzed to see if the variance, mode, or standard deviation changes significantly between one run and the next. Once the calibration pulse is completed, the calibration voltage is turned off. After some settling, the thruster is started and data collection can take place. A calibration pulse should have an exponential sinusoidal decay based on the physical dynamics of the torsion balance. It is essentially an oscillator with viscous forces resisting the movement of the balance arm. A good calibration pulse can be seen on the oscilloscope for qualitative assessment as in Figure 24.
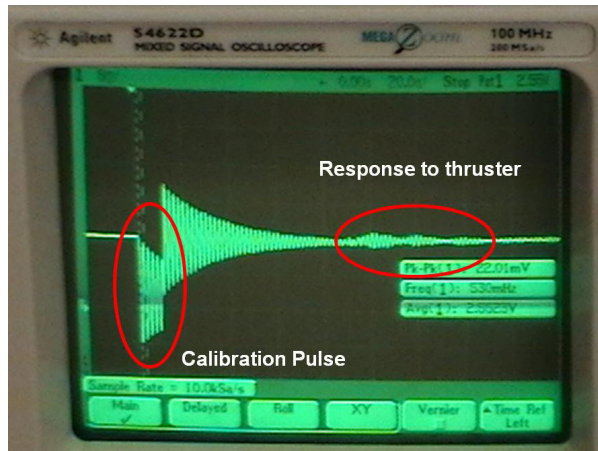
(a) Oscilloscope display of calibration pulse and thruster response after settling.
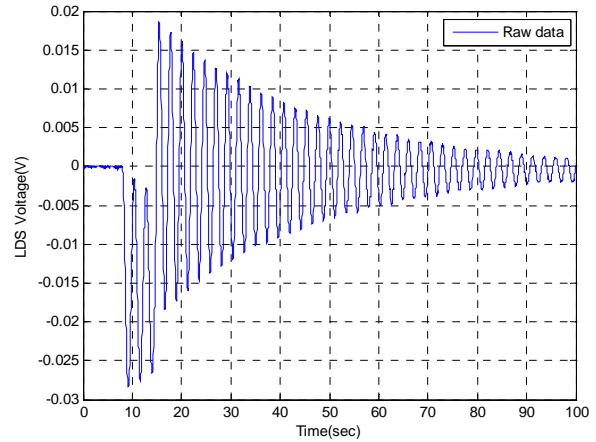
(b) MATLAB™ plot of calibration pulse

Figure 24. Typical calibration pulse

The data collected for various calibration pulses and the thruster is presented in the analysis and results chapter of this thesis.

Calibration of Laser Displacement Sensor (LDS)

The TBS requires the LDS operation in a region where the voltage is a linear function of displacement. The LDS is manufactured by Philtec™ and the manufacturer provided sensitivity measurements and calibration curves. The near side sensitivity of the LDS is 0.916 mV/µIn. The far side sensitivity slope is -15.30mV/mil, and used to relate the voltage change to a change in linear displacement of the arm and mirror relative to the LDS sensor. For the sensor, a voltage range of three to three and a half is used as the operating region of the LDS, and is where the output voltage varies directly with distance between reflecting mirror and the LDS sensor tip.

The LDS has coarse and fine correction screws and is adjusted so the maximum voltage output from the LDS is five volts. The LDS operates on either the 'near' and 'far' side, with each calibration curve having different constants, so the operator needs to know which side of the curve applies to the system under operation. Once the LDS unit is calibrated, the next step is to determine the proper distance the calibration electrodes need to be apart.

41

Calibration of Electrode Distance

The calibration electrode distance must be exactly 1mm apart to use the voltage force conversion formula in the TBS operations manual. If the electrodes move too close together, and make contact each other, they will short out. If shorted out, the electrodes will remain together and calibration data cannot be taken. This occurred twice during the research, and each time, the chamber brought back to atmospheric conditions, recalibrated, and pumped back down to vacuum conditions. Once the electrodes are the correct distance apart, the force of attraction between the electrodes is calculated using equation (24)

This equation is a modified form of the equation for two parallel conducting plates but adjusted due to the different sizes of the electrodes and electric field variations near the edge of the electrodes. This set distance is accomplished in the following way. First, the operator verifies the LDS system is on and calibrated as stated above. Second, have the spacing initially about 1.0 mm apart, and move the calibration electrode towards the electrode on the TBS arm until the LDS voltage changes up or down as shown in Figure 25.
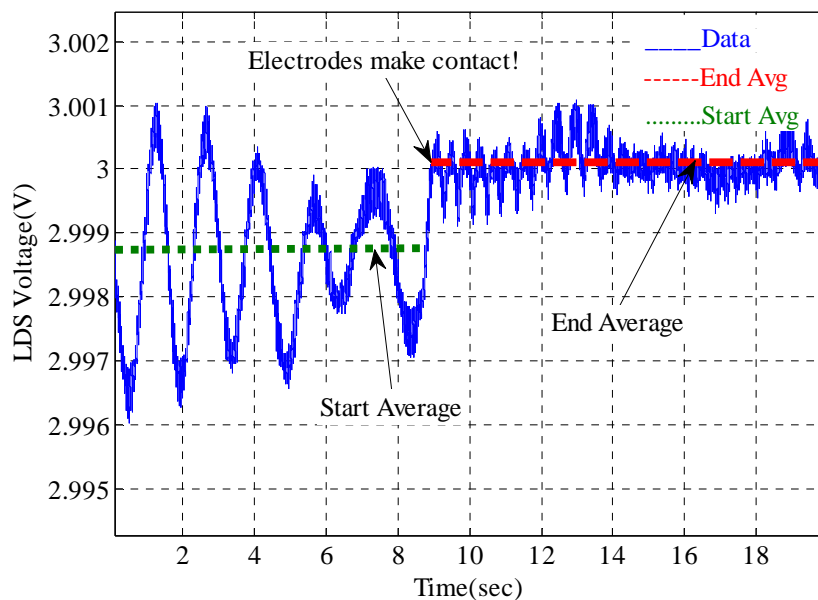
Figure 25. Electrode calibration

Once the electrodes make contact, there should be an immediate vertical shift in the oscilloscope trace. Back the electrode off until this shift is as small as possible. Third, using the position micrometer turn the micrometer two full turns counterclockwise. Each full turn corresponds to 500 µm, so two full turns is 1000 µm or 1.0 mm. The electrodes are now exactly 1.0 millimeter apart in spacing. The formula to calculate the calibration force between the set of electrodes is:

$$F_{cal} = \frac{(1.262 \times 10^{-9})(1 + 138.1 * d)V_{cal}^2}{d^2} \tag{24}$$

The quantity d is the distance between the electrodes (1.0 mm) if set properly using the procedure discussed in the operations manual above. V_{cal} is the applied calibration voltage, which was 800V in this case to provide enough force to move the balance arm above the noise floor. This force is inversely proportional to the square of the distance between the electrodes and proportional to the square of the applied voltage. The non-linearity of this equation poses challenges if the electrodes move significantly, especially if it results in moving outside the linear response range of the LDS.

The electrode distance must be set prior to obtaining vacuum conditions, the LDS response may drift due to variations in thermal conditions and metallic expansion/contracting inducing strain. To correlate the effect of thruster with the oscilloscope, the sign convention and direction must be established. The sign convention of the system is shown in Figure 26. From Figure 26, if the electrodes are moving move further away from each other, then the mirror is moving closer to the LDS tip resulting in an increase in the voltage output from the LDS. This result indicated the LDS is operating on the "far" side of its sensitivity curve. If it were on the near side, as the gap became smaller, the voltage output would decrease. The near side

sensitivity slope of 0.916 mV/µIn would be ideal for sub micro-Newton thrusters, but proved too difficult to use in practice.
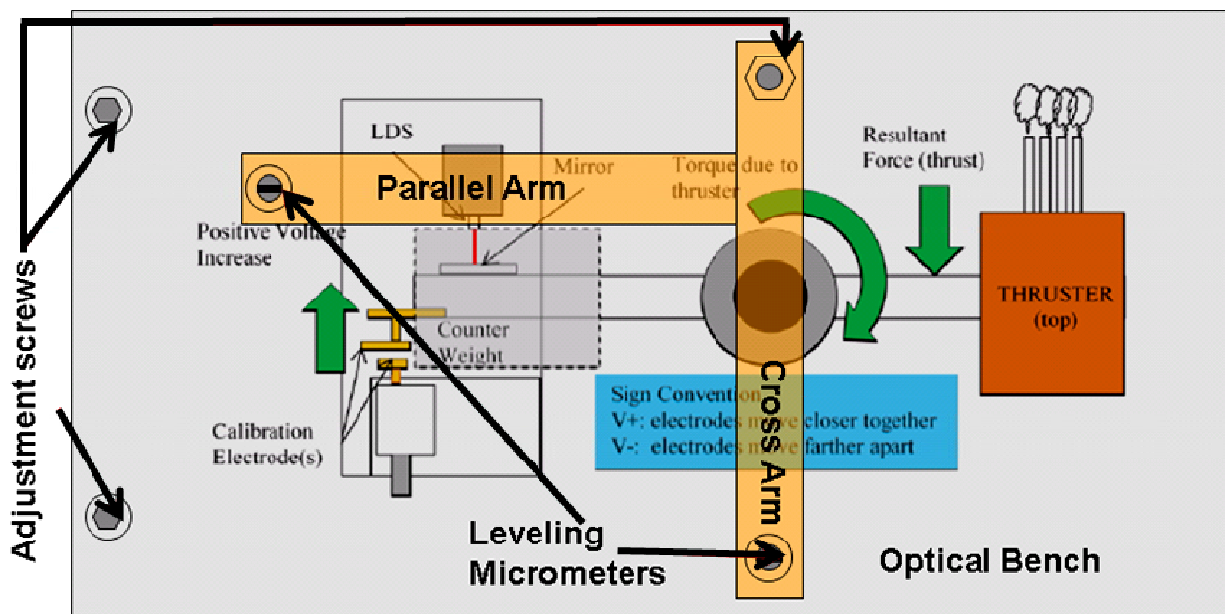
Figure 26. Sign convention/leveling devices-using far side of LDS

The extreme sensitivity on the near side of the sensor, made that side impractical to use. Use of the near side is desired for sensitivity reasons, but was too sensitive and would quickly move out of the linear operating range of the LDS, or would saturate and move to the topside of the curve, making it useless for data gathering and analysis. The near side of the LDS only has a useful range of 1.9 (0.05 mm) to 3.7 mil (0.094mm). Thermal drift and external noise are enough to move the TBS out of this range. However, the far side has a useful range from 37 mil (0.942 mm) to 149.2 mil (3.79 mm), which should be controllable.

Balancing and Leveling the Torsion Balance

The LACO™ vacuum chamber only has a volume of 0.178 m^3, and made it very confined space to work inside with the torsion balance, thruster, and counterweight. A special stand constructed out of 80/20™ aluminum was used to elevate the torsion balance, which was mounted to an optical bench plate. The adjustment screw on the left side of cross arm in Figure

26 was inaccessible so two more screws were added to the optical bench to allow leveling in 2-axes. The additions of these screws provided an additional benefit of providing greater control of the leveling procedure without having to bump the counterweight or disturb the wiring inside the chamber.

The leveling of the balance should be done with the thruster and counterweight installed, because the weight of these components will affect the leveling and strain on the stand and need the level point may change if these mass effects are not taken into account in the baseline measurements. The counterweight was milled out of T6061 aluminum and had dimensions of (127 x 76.2 x76.2) mm, cross sectional area of $5.80644 *10^{-3}$ m^2 and a volume of $7.374*10^{-4}$ m^3. Using the volume and mass, the density of the block is calculated to be 2604 kg/m^3. The block of aluminum also had a 7.9375 mm hole drilled into the bottom, so it could be mounted on a sheet metal base and attached to the thruster mounting plate. It was recommended later the counterweight not be fixed to compensate for any center of gravity (CG) error due to moving the thruster in and out of the chamber.

One of the other pieces of equipment needed to level the balance properly was a pivoting mirror. The tight space of the chamber prohibited anyone from sticking their head in to directly view bubble level provided with the torsion balance. So, this mirror is required in combination with a laser and LED light source to see when the bubble was in the center of the black circle indicating the system was level. A device was constructed to allow viewing of the bubble level and the physical operation of the thrust using two mirrors mounted to an 80/20™ stand at 45 degrees, effectively acting as a beam redirector. The stand, mirror, and the bubble level are shown in a-d of Figure 27. The picture in (a) of Figure 27 redirected the image of the thruster out of one of the port windows on the side of the chamber.

The size of the chamber severely limited pointing options for the thruster. If the thruster is placed in the front, it would not be possible to adjust the leveling micrometers from the back of the vacuum chamber without disturbing the test setup significantly. The length of the balance optical bench and the arm would also not permit sideways mounting of the torsion balance, where the thruster would face the main viewing window on the front of the chamber. The other difficulty in repositioning the torsion balance is to avoid the wires going to the GG-µPPT unit from twisting too much. Any excessive twisting in the wires will force them to act like a torsional spring, adding undesired responses and measurements of the dynamics of the system, if severe enough. There is also concern of damaging the fiber optic fibers of the LDS feeding into the chamber. Excessive twisting could potentially result in fracture of these fibers and degraded LDS performance and measurements.

(a) Thruster observation stand

(b) Pivoting mirror to see position of bubble leveler

(c) DPSS 532 nm laser illumination

(d) LED illumination
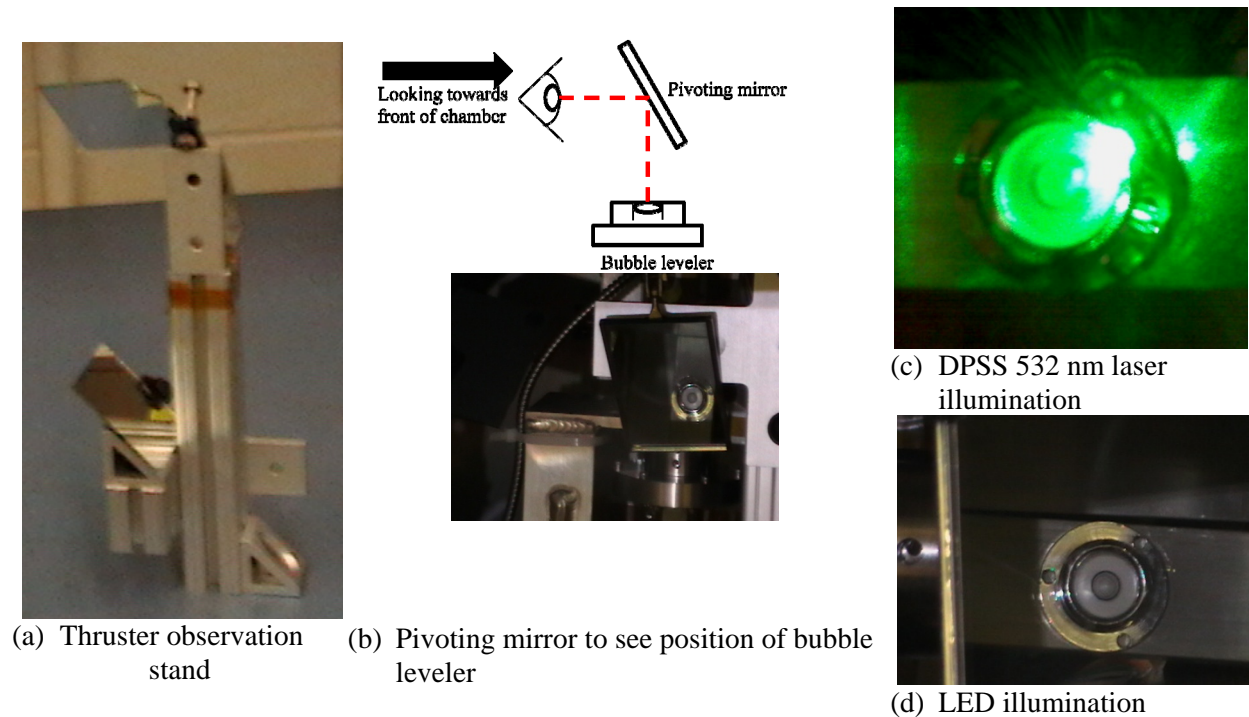
Figure 27. Viewing mirrors and bubble leveler

The image in (b) of Figure 27 allowed the leveler to be viewed from the top, because the mirror placed at a 45-60 degree angle to the vertical provided a top view of the bubble leveler, which eliminating the need for an individual to stick their head into the chamber and risk perturbing the system. With the balance level, connections made, and calibration of LDS and torsion balance, we now discuss the input parameters that the operator can vary, and the test point matrix.

Independent Control Variables

The four parameters controlled in the operator of the GG-μPPT are discharge energy, firing order, pulse frequency, and input voltage. The discharge energy of the arc is crucial due to operation and potential carbon deposition. The firing order can reveal the impact of buildup and cross contamination as well as potential asymmetric thrust from one stick to another. The input frequency can vary from 0.5 to 2.0 Hz. The higher frequency provides the ability to achieve a pseudo-constant thrust level. The variation in input voltage allows determination of the minimum power required for thruster operation.

The GG-μPPT system is software controlled with an RS232 serial connection. The operator of the thruster can see the status of the individual μPPTs on the Cubloc™ software provided by Busek™. Once all the connections are made, the operator provides power to the GG-μPPT unit and opens up the debugger tool in the Cubloc™ software that came with the unit. The operator should see a Gatling-gun pattern of 'X's, indicating those sticks are not enabled. When enabled, the 'X's will turn into a number, indicating that stick is active and ready to fire. The operator then determines the sequential firing order of the sticks by turning on the appropriate toggle switches numbered one thru nine on the stick selector module.

The operator then turns the frequency knob to a value between a one-half hertz and two

hertz. The sticks are now firing and should show up as voltage changes on the oscilloscope as in

(a) of Figure 24. A complete setup of the system is shown in Figure 28. The necessary

calibration voltage needed, is provided using the EMCO™ DC-DC power converter and a

Hewlett-Packard™ 200W power supply. The 800V voltage was routed into the chamber

separate from the other connections to prevent the possibility of arcing or short-circuiting to a

component in the thruster. The power to electrodes was supplied only when a calibration pulse

needed to be taken, for instance when the thruster was reprogrammed and placed back into the

vacuum chamber for further testing.
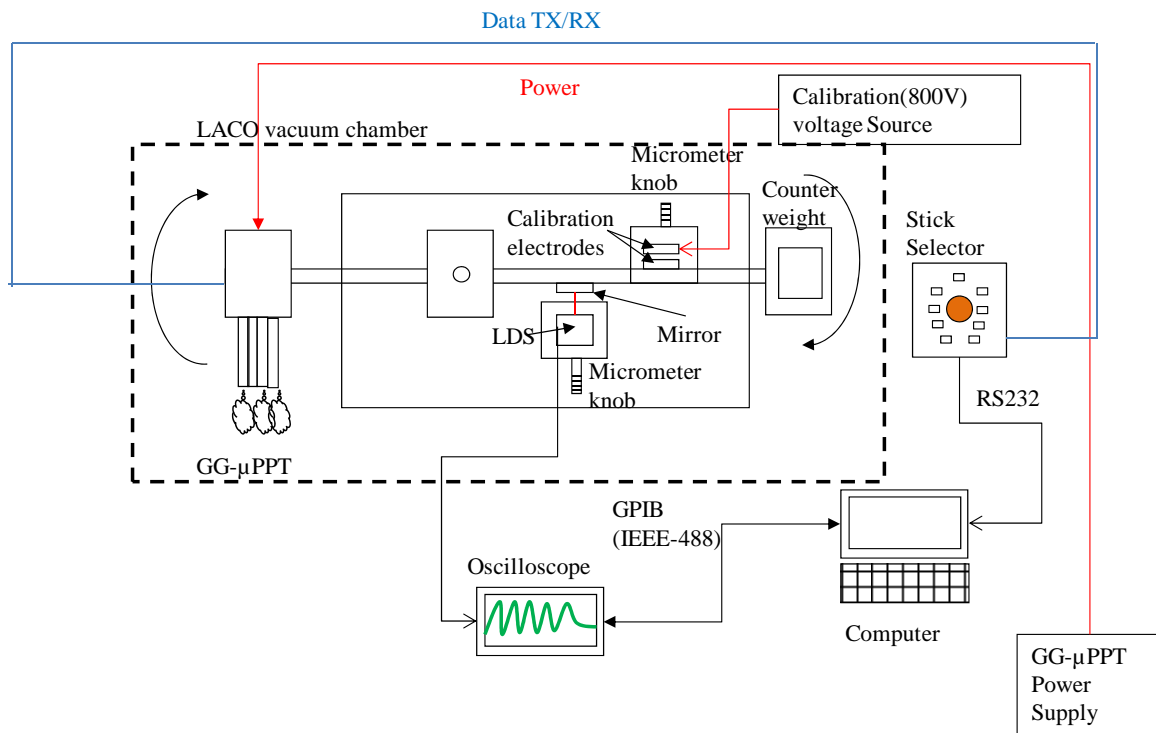
Figure 28. GG-µPPT setup

To determine the effect of frequency, discharge energy, and firing pattern on the performance of the thruster, a test matrix was required. The test conditions are repeated enough times so bias and experimental error can be determined. This thruster configuration and module being new, very little research into its operation and characterization exist.

The testing to date on this thruster was simply to determine the impulse bit or Ibit for the thruster, and the average mass loss per discharge. The matrix of planned test conditions is shown in Table 4. This combination of parameters provided 192 possible test conditions, more than sufficient to provide the needed data sample size for statistical data analysis and comparison.

Table 4. Test Conditions for various input voltage, frequency and discharge energy

Discharge energy (J)	Output Voltage (V)	Frequency(Hz)	Stick pattern	Voltage (V)
		$E=1/2CV^2, C=2\mu F$		
1.7	1303.84	0.5,1,1.5,2	1,2,3,4,5,6,7,8,9	12.5,15,17.5,20
1.6	1264.91	0.5,1,1.5,2	1,2,3,4,5,6,7,8,9	12.5,15,17.5,20
1.5	1224.74	0.5,1,1.5,2	1,2,3,4,5,6,7,8,9	12.5,15,17.5,20
1.4	1183.22	0.5,1,1.5,2	1,2,3,4,5,6,7,8,9	12.5,15,17.5,20
1.3	1140.18	0.5,1,1.5,2	1,2,3,4,5,6,7,8,9	12.5,15,17.5,20
1.2	1095.45	0.5,1,1.5,2	1,2,3,4,5,6,7,8,9	12.5,15,17.5,20
Discharge energy (J)	Output Voltage (V)	Frequency (Hz)	Stick pattern	Voltage (V)
1.7	1303.84	0.5,1,1.5,2	3,8	12.5,15,17.5,20
1.6	1264.91	0.5,1,1.5,2	3,8	12.5,15,17.5,20
1.5	1224.74	0.5,1,1.5,2	3,8	12.5,15,17.5,20
1.4	1183.22	0.5,1,1.5,2	3,8	12.5,15,17.5,20
1.3	1140.18	0.5,1,1.5,2	3,8	12.5,15,17.5,20
1.2	1095.45	0.5,1,1.5,2	3,8	12.5,15,17.5,20

After the equipment was set-up and the necessary connections are made as shown in Figure 28, the physical properties of the thruster, counterweight and torsion balance was measured and collected. Once complete, the equipment was calibrated and baseline data taken to

establish a reference frame from which the data collected was analyzed. We are now to ready to

start collecting data from the thruster and start by solving the equations of motion (EOM) for the

torsion balance system and its thruster and counterweight.

Solution approach

The desired method of modeling for the torsion balance system and the thruster was to

model the system as a harmonic oscillator and solve the equations of motion directly to achieve

predicted deflection angles, theta in radians. Once this deflection angle is known, the force and

hence thrust from the thruster can be found by applying rotational dynamics and statics to the

system and find the force that produces the observed deflection with the determined spring

constants for the entire system. This method was iterated until the root mean square error

(RMSE) was minimized or matching was optimal, based on the pulse train of the input signal for

various thrust levels from 0 to 200 µN. The formula is fairly simple and has the form:

$$\text{RMSE} = \sqrt{\frac{\sum_{i=1}^{n}(\text{X\_data} - \text{X\_model})^2}{n}} \tag{25}$$

RMSE has the same units as the dependent variables and is the error doubles, the RMSE

doubles. This direct relationship is not so if using MSE, but it is still widely used. The smaller,

the RMSE, the better fit the model is to the data in question. The solution approach can also be

depicted graphically and shown Figure 29.
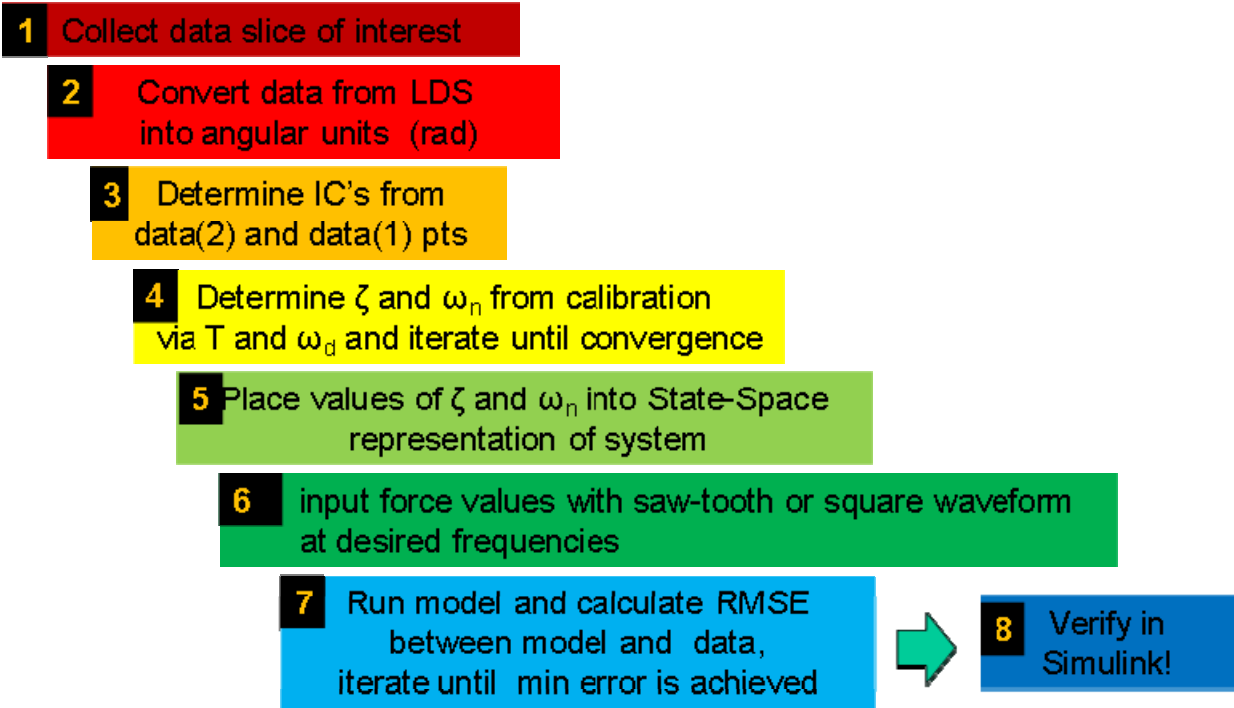
Figure 29. Graphical Solution Approach

IV.   Analysis and Results

This chapter begins by looking at the mathematics and physical properties of the torsion balance system, and from there, develops the equations of motion (EOM) for the torsion balance and its relation to the force provided by the thruster. Next, some plots for the range of discharge energies from 1.7 to 1.2 J comparing the data gathered against the model. Then, discussion of power needed for operation and the accumulation of carbon on the propellant face. Afterwards, the discussion turns to the variation of thrust with discharge energy, frequency and input power. Next, we discuss the results of determining torque from the firing of sticks three and eight of the GG-μPPT module. Finally, we discuss the various amounts and forms of error present in the experiment

Equations of Motion

The first step in understanding the behavior of the thruster was to solve the equations of motion for the torsion balance and to use this solution to model the behavior of the balance due to the thruster for various firing frequencies and discharge energies. The equation of motion of the torsion balance was a second-order ordinary differential equation, ODE. The solution of this ODE required use of state-space methods or Laplace Transforms from linear systems theory.

From linear systems theory, the force is not always a linear function of the spring constant if the angle is very large, because all springs have a range where their force is no long linearly proportional to the amount of deflection. This phenomenon is because of elastic limits of real materials. Fortunately, the angles resulting from the thruster are approximately 10^{-5} radians, so small angle approximations are valid for this analysis and provided excellent results. The angle of displacement can be determined from some trigonometry and data about the moment arm and LDS measurements as in Figure 30. For angles on order of tens to micro-radians, the inverse tangent and inverse sine functions provided the same result essentially, because of the small angles involved.

$r_{LDS}\_tip*sin(\theta)$
$=Y(displacement)$

r_{LDS}_tip

θ
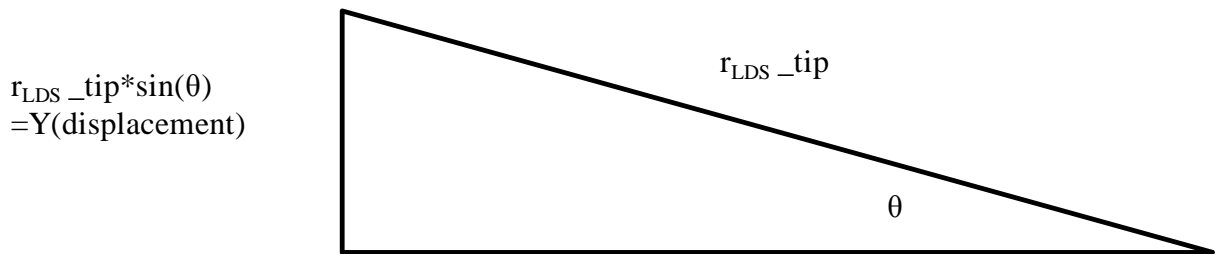
Figure 30. Trigonometry to determine angular displacement

Determination of the angle was accomplished by taking the inverse sine of the ratio of the displacement, to the radius of rotation of the LDS sensor tip. The displacement was determined by converting the LDS output voltage into an equivalent displacement. For example if the

sensitivity was 15.30 mV/mil (602 mV/mm) and we saw a 1.0 mV change from the LDS, then

the displacement is 1/602 mm or ~$1.6611*10^{-3}$ mm or 1.6611 μm. This relationship is shown in

Eq.(26)

$$\theta = \sin^{-1}\left(\frac{Y}{rLDS\_tip}\right) = \frac{output(V)*\dfrac{1}{Sensitivity(V/m)}}{distance(m)} \tag{26}$$

The angle and hence the displacement from the neutral position was found through the

above method. This assumption allows the equations of motion to be modeled as a linear

system. With this being the case, the angular displacement was directly proportional to the

spring constant of the system. The torsion balance has an internal spring constant of 11.6

mN/radian, but the spring constant of the wiring and connecting structure must be taken into

account to get an "equivalent" spring constant for the system. This effect should not affect the

overall thrust calculation, but rather will result in a stiffer spring constant and therefore smaller

angular displacement.

The system model for the balance and thruster is essentially a harmonic oscillator

described by the second order ODE. The parameters that affect the behavior are the damping

ratio, ζ, and the natural frequency of the system, ω_n. The equation for the system is [22]:

$$\ddot{\theta} + 2\zeta\omega_n \dot{\theta} + \omega_n^2 \theta = \frac{F(t)*R_{thruster}}{I_{total}} \tag{27}$$

The first and second derivatives of angular position are angular velocity and angular acceleration

respectively. F(t) is the forcing function (thruster) and $R_{thruster}$ is the moment arm of rotation, and

I_{total} is the total moment of inertia for the torsion balance including the arm, thruster and

counterweight. If the damping ratio is less than one, the system will have at least one complete

oscillation and is under-damped. If the damping ratio is larger than one, the system will have no

oscillations and critically damped. The system will respond like a first order differential system where it will rise steeply, but then asymptotically approach its equilibrium or final value at t→∞. This system is the angular analog to the spring mass damper system.

The damping ratio can be determined by looking at the calibration pulse. The natural frequency, ω_n can be determined from ω_d, which is the damped natural frequency of the system, and the only one observed experimentally. They are related to each other through the damping ratio, ζ, so once one is known, the other can be found. The ability to determine the quantities accurately along with measurement errors, system noise, and tolerances will dictate how closely the model matches the data. Ziemer [22] solved the equation for an impulse input. The initial conditions for model at time equal to zero was determined from the data when the pulse first was detected by the oscilloscope and Cublock™ software. The impulse solution to the above equation has the form:

$$\theta(t) = \frac{I_{bit} * R_{thruster}}{I_{total} * \omega_d} * e^{-\zeta * \omega_n * t} \sin(\omega_d * t + \Phi)$$

(28)

$$\omega_d = \omega_n \sqrt{\left(1 - \zeta^2\right)}$$

The term Φ is the phase shift of the signal in radians from zero. For the system at rest, the phase angle, Φ should be zero for the simplest case. The impulse bit or I_{bit} is determined from the initial velocity at t=0, I_{total}, and radius of rotation, $R_{thruster}$ through:

$$I_{bit} = \frac{\dot{\theta} * I_{total}}{R_{thruster}}$$

(29)

The angular velocity at time zero, can be evaluated by determine the change in slope of the angular displacement very close to the time when the input supplied force, F (t). Some error

results, but if the time step is very small, it should provide a good approximation for angular velocity at t=0.0. Once these quantities were determined, MATLAB™ can model the system and compare that result to the data for comparison and amount of agreement between theory and experiment. Laplace Transforms are another method for determining the response of the system if the forcing function is simple, i.e. impulse, step, ramp, or sinusoid. This method allowed manipulation of the parameters algebraically in the frequency domain, instead of dealing with differential and integral Calculus [24].

The other method of solving this system of differential equations is to work in the frequency or 's' domain as it is commonly referred to. The attractiveness of this method is that the solutions can be obtained using algebra to solve the roots of the characteristic polynomial, which represents the zeros, poles, and gain of the system (ZPK). Once the general form to the solution is found, eigenvectors and their corresponding eigenvalues along with matrix algebra and a table of Laplace transforms will provide a solution to this system. Analysis in the time domain and frequency should provide the same result, since we are talking about the same physical system under analysis. MATLAB™ is equally capable of working in this domain as well, and the 'tf2ss' function can be used to get back to the state-space representation if desired.

H(s) is the transfer function and maps the input F(s) to the output Y(s) in the frequency domain. In the case of the system given by Eq.(27), if the input F (t) is a unit impulse, than its Laplace Transform is one in the frequency domain. The transfer function will have the form of:

$$H(s) = \frac{1 * \dfrac{R_{thruster}}{I_{total}}}{s^2 + 2\zeta\omega_n s + \omega_n^2} \tag{30}$$

This equation will generate the same response as the time domain state-space representation in equation (27) for a unit impulse. However, since all the data and parameters are measured

relative to time, the analysis was done in the time domain. The other down side to using Laplace

Transforms to solve the ODE for the system, is that the inverse Laplace Transform for that

forcing function must be known, and is not always the case. The first situation examined was the

impulse response of the test data against the impulse model of the system.

Test Data and Models

The impulse model for the system was the first system analyzed to see the system

response and to determine how closely it agree with data for a measurement. The impulse was

supplied by the firing of a single thruster stick, accomplished by rapidly turning the thruster off

immediately after one discharge. The state-space of the system is found by writing the 2nd order

ODE as a set of first order ODEs using substitution letting $X_1=\theta$ and $X_2=\dot{\theta}$, the system has the

follow representation in terms of matrices A, B, C, and D. A is called the state transition matrix,

[24] because it maps the states from one value to another as the input signal is applied to the

system

$$\dot{x}=Ax+Bu, x=\begin{bmatrix}\theta\\\dot{\theta}\end{bmatrix}, u=F(t), \text{ where } A=\begin{bmatrix}0 & 1\\-\omega_n^2 & -2\zeta\omega_n\end{bmatrix} \quad B=\begin{bmatrix}0\\\dfrac{R_{thruster}}{I_{total}}\end{bmatrix}$$

$$C=\begin{bmatrix}1 & 0\end{bmatrix} \qquad D=0$$

$$y=Cx+Du \qquad\qquad\qquad\qquad\qquad\qquad\qquad (31)$$

The matrices also have significance in the frequency domain as well, since the transfer H(s) was

computed from A, B, C, and D through the formula:

$$H(S) = (sI - A)^{-1} \cdot B + D$$

$$\qquad\qquad\qquad\qquad\qquad\qquad\qquad\qquad (32)$$

The inverse term denotes the matrix inverse. The above system can also be built in Simulink™ which was used to verify the code that found the thrust values, and to check out the system response to various types of forcing functions.
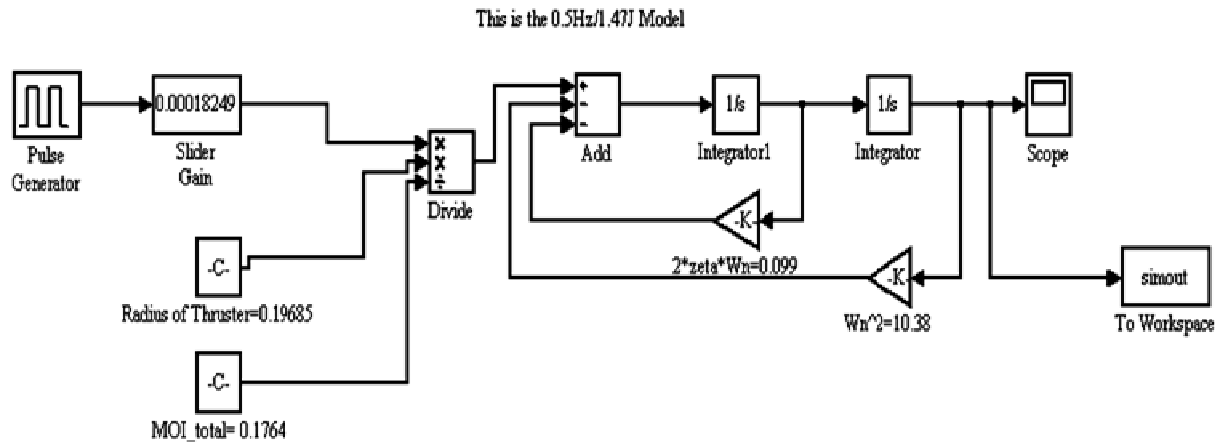
Figure 31. Simulink™ model for Torsion Balance System and Thruster

For the multi-pulse model, the pulse generator was set to operate at the firing frequency of the thruster according to the time between firings provided by the Cubloc™ software. Both in Simulink™ and MATLAB™, the signals usually have unit amplitude. This effect is the reason for the slide gain in which it amplifies or attenuates a baseline input signal. The signal is then fed into the state-space model to obtain the output, which is an angular deflection.

The impulse response for 1.47J is shown in Figure 32. The data was compared against the model and the system was iterated until a minimum Root Mean Square Error, RMSE of 12.6197 μrad was obtained. This corresponded to a Ibit of approximately 107 μN-s with a standard deviation of 23 μN-s. The LDS does drift a little over time, but is on the order of 100 μV, and does not significantly affect the fitting of the data slice to the model. The drift is progressing at a constant rate, so it can be removed through algebraic techniques. This drift determination essentially involved determining the linear regression coefficient of the data that had a drift rate, and shift the data in the opposite direction to counteract the drift. For example, if

the data had a slight negative slope to it, the data would be shifted by a positive slope of equal

magnitude to the negative slope vectorially, cancelling out the drift due to the external factors or

improper C.G. placement or external vibration .
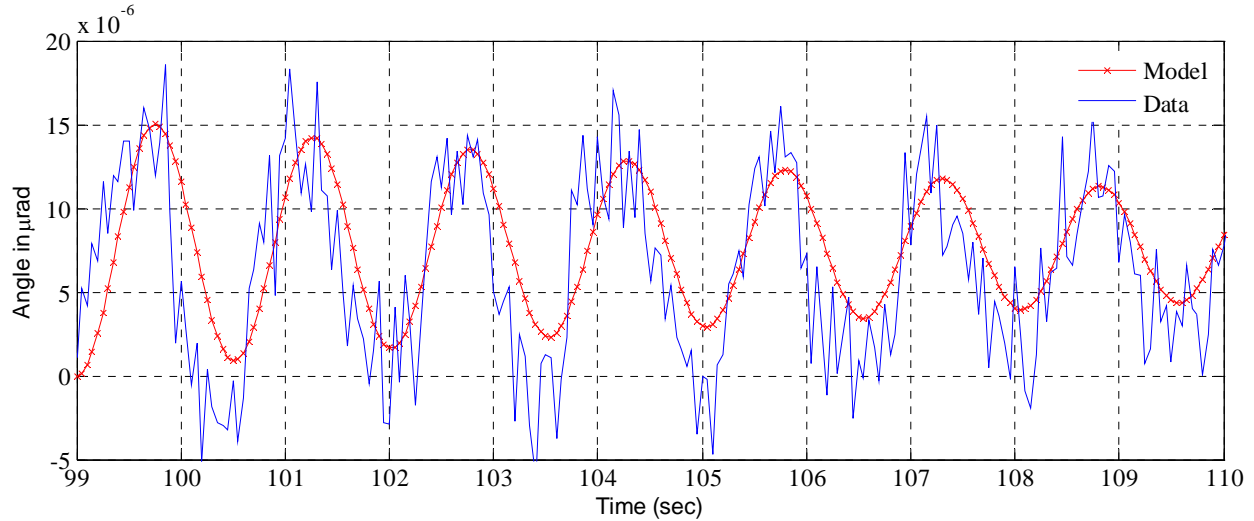
Figure 32. Impulse response for 1.47J setting

The initial set of data was taken at the default energy discharge setting of 1.47J, and the

nominal operating voltage was chosen at 15V, the midpoint between the 10-20V ranges stated in

operations manual. From this point, the voltage varied from 12.5 to 20 volts in increments of 2.5

volts. The original plan was to start from 10 volts, but as described later, 10 volts was too low to

operate the thruster sticks of the GG-μPPT module.

The data processing required the use of a Butterworth filter that has a slope of -20*n

decibels (dB) per decade (power of 10), where n is the order of the filter. A fifth or sixth degree

filter was used and shown in Figure 33 and is used as low-pass filter for the data.
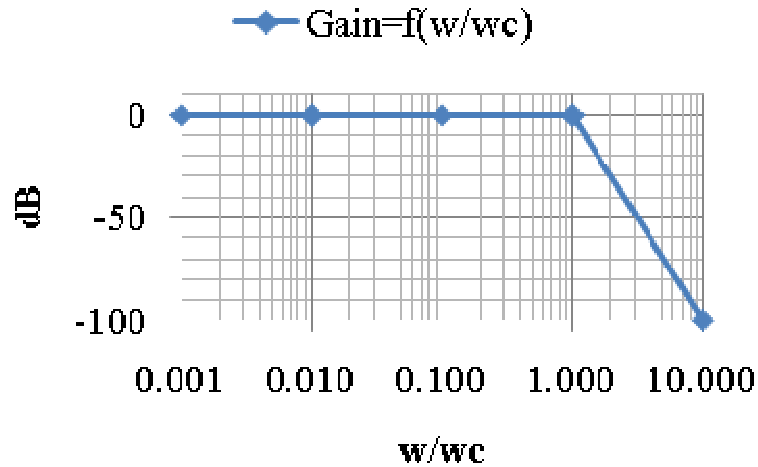
Figure 33. Fifth-order Butterworth filter

The EMI spikes generated by the discharge capacitor proved to be very useful as an accurate clock and counter of pulses from the thruster sticks. For example, using the spikes from the raw data, before it was filtered the starting point for the multiple pulse data set was determined. Because of the very short nature of these pulses, the pulses would accurately depict where or when the thruster fires. This ability eliminated the need to rely on a separate detection sensor to count the pulses as the thruster fired in the chamber. The voltage spike seen from the oscilloscope were much greater than the noise floor as seen in (a) of Figure 34. The data was further processed to see in more detail, the magnitude and response of the balance to the thruster as shown in (b) of Figure 34.
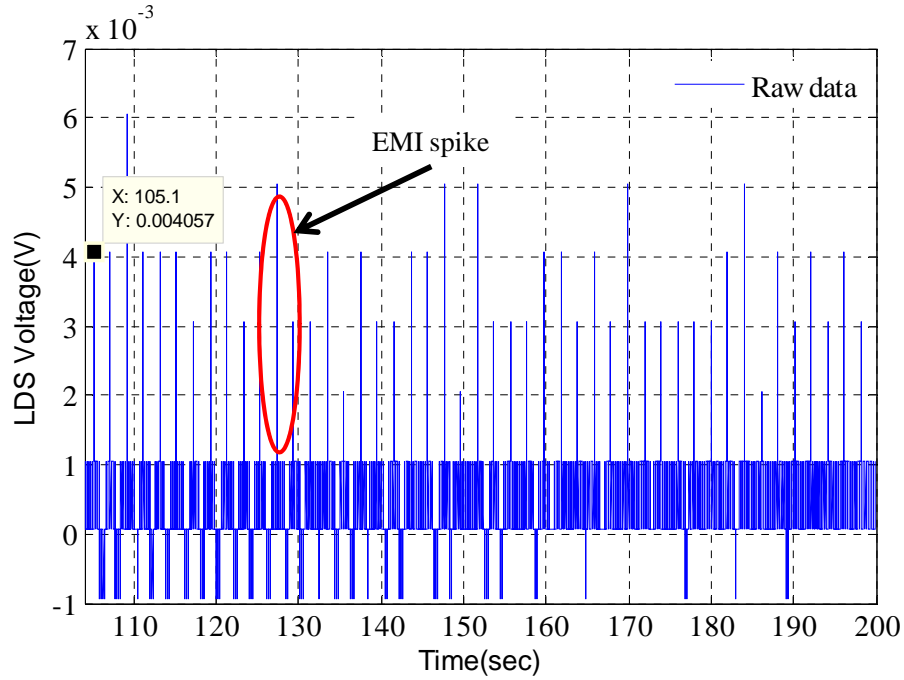
(a) EMI spike provides a reliable way to determine exact firing of thruster, within the resolution of the oscilloscope and sampled data
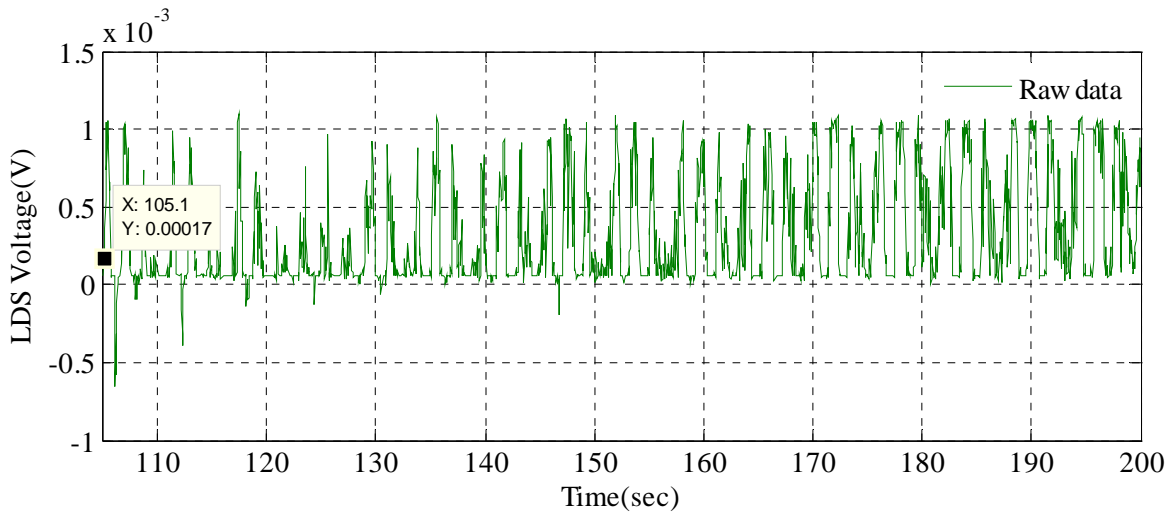
(b) Butterworth filter of response in (a) showing the detailed oscillations of the balance from the thruster firing at the set frequency

Figure 34. Filtered data of raw system response

To model system response, a model of the input forcing function requires simulation, along with the initial conditions of the system. The system can be modeled as saw tooth or

square wave input. The type of forcing function model used will depend on how accurately it represents the actual shape of the forcing function in the experiment.

The forcing function, F(t) can be modeled using the 'gensig' function in MATLAB™ or the pulse generator in Simulink™. The 'gensig' function will produce a unit amplitude pulse train. It must be multiplied by the appropriate gain to scale the forcing function to the correct value needed to model the data. The multi-pulse model is more complicated to model than a single impulse model, because the pulses will interact with each other preventing a complete decay of the transient condition to the final state as will happen with an impulse input. However, if the general shape of the forcing function is known, i.e., it is a square, sinusoidal, exponential, linear (ramp) input or constant (step) input, the system can be iteratively solved to determine the thrust values responsible for producing those waveforms.

For the pulse generator, the pulse width was chosen 1.0 second in duration, which allowed the force determined to be equal to the average Ibit over that period of time. The actual pulse trigger discharge occurs very quickly and based on discussions with Busek, is around 10µs. Thrust generation occurs over a longer time frame is usually in the range of 60 to 80µs, based on plume analysis and high-speed imagery captured by Selstrom [13] as well as pulse durations captured during this research effort. Shown in Figure 35, are five pulses plotted on top of each other. The pulse duration in Figure 35 was determined by looking at the point where the voltage increased above the baseline noise and continued upward to its maximum value, and then decreased back down to the baseline voltage level, which was 4.03V in Figure 35. This pulse duration represents the entire ablation an ionization timeframe. The actual duration of the discharge is smaller and approximately 10 µs. The pulses all have a triangular shape, but vary in magnitude and duration slightly over the five pulses collected and plotted in Figure 35.
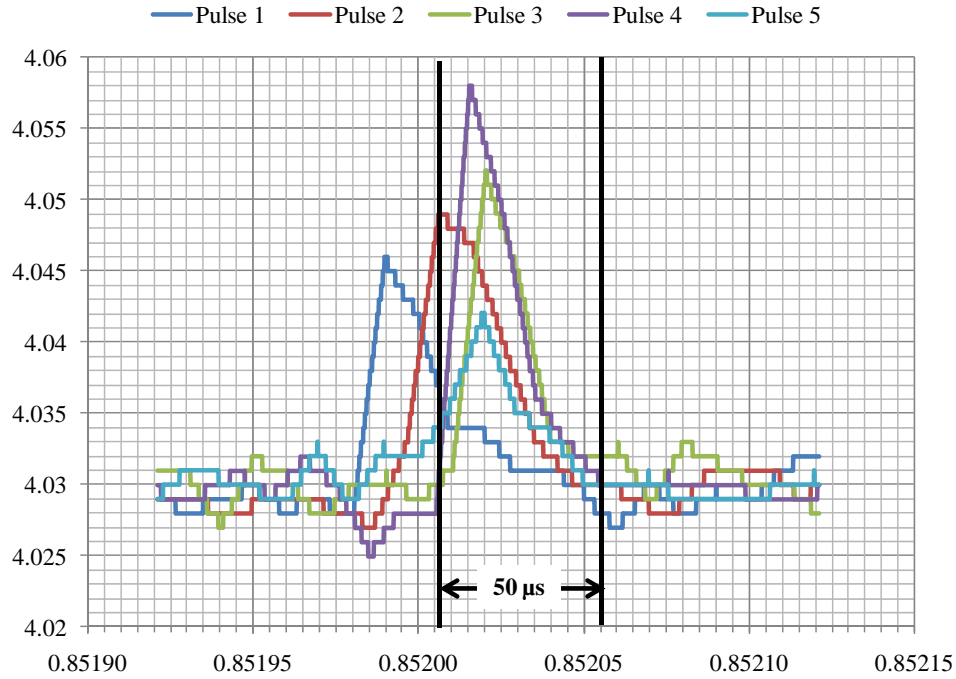
Figure 35. PPT pulse shape and duration

This was then chosen as the timeframe initially for the pulse model and adjusted up to 1.0 second with a period equal to the inverse of the firing frequency chosen. Now, we will look at some of the plots generated from the data and model and plot them on top of each other for comparison.

The 1.47J data was the first round data taken, since it did not require removal from the vacuum chamber and reprogramming of the thruster. The match of 1.0 Hz data with the model, shown in Figure 36 and had a total RMSE of 81 µrad for the pulse train. The data under ideal conditions should be closer to the shape of the model, but even the use of the Butterworth filter was not able to remove all the sources of noise present in the signal or perturbations from the nitrogen pumps that would turn off and on in the lab during testing. Two large tanks of carbon dioxide were also present in the lab, and would vent from time to time to regulate the pressure in the tanks. Unfortunately, when this occurred, the vibration would transit from the tanks to the balance through the floor, affecting the measurements slightly.
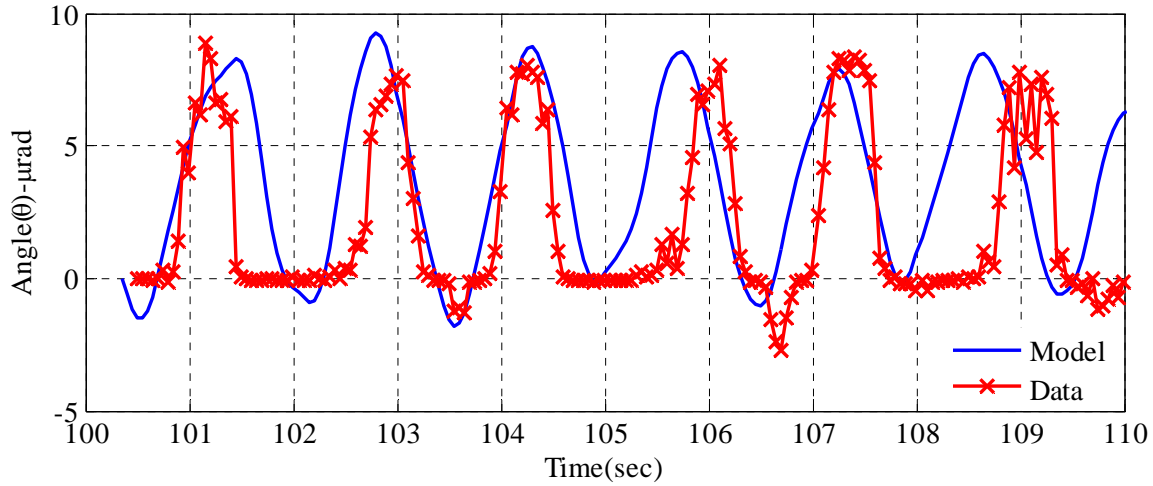
Figure 36. 1Hz 1.47J data and model plotted on same graph

The Ibit corresponding to this plot is 95.98 µN-s. The average Ibit over all runs is 108 µN-s. Other measurements were taken and the thrust and Ibit determined from solving the EOM for the system and the forcing function respectively. All the thrust values obtained for the 1.47J setting for various frequencies and input settings are shown in Table 5. The range of thrust values tend to be spread out for this sample, but are higher in magnitude than the rest as we will see.

Table 5. Ibit at various frequencies and voltages for 1.47J

Voltage	Frequency (Hz)	Ibit (µN-s)
17.5	2.00	134.12
15	2.00	95.98
20	1.50	157.19
15	1.50	105.99
15	1.00	106.90
12.5	1.00	95.98
12.5	0.67	79.00
17.5	0.50	107.48
12.5	0.50	96.51
Mean Ibit (µN-s)		**108.79**
Standard Deviation (µN-s)		**23.35**

The next set of plots is the 1.697J data collected at various operating voltages and frequencies. The 1.697J setting was the highest programmable setting on the thruster, for discharge energy. The software did not allow the selection of a voltage past 1300V, without risk of damaging the unit, and a two-µF capacitor provides approximately 1.7J of energy to each thruster stick per discharge at 1300V. The match between the data and the model was iterated until reaching the minimum RMSE was found. The 12.5V 1.697J plot is the first one in this set of data. The RMSE associated with the run is 12.1 µrad and is shown in Figure 37. The data matches the model well in this case, as indicated by the low RMSE value compared with the previous plot.
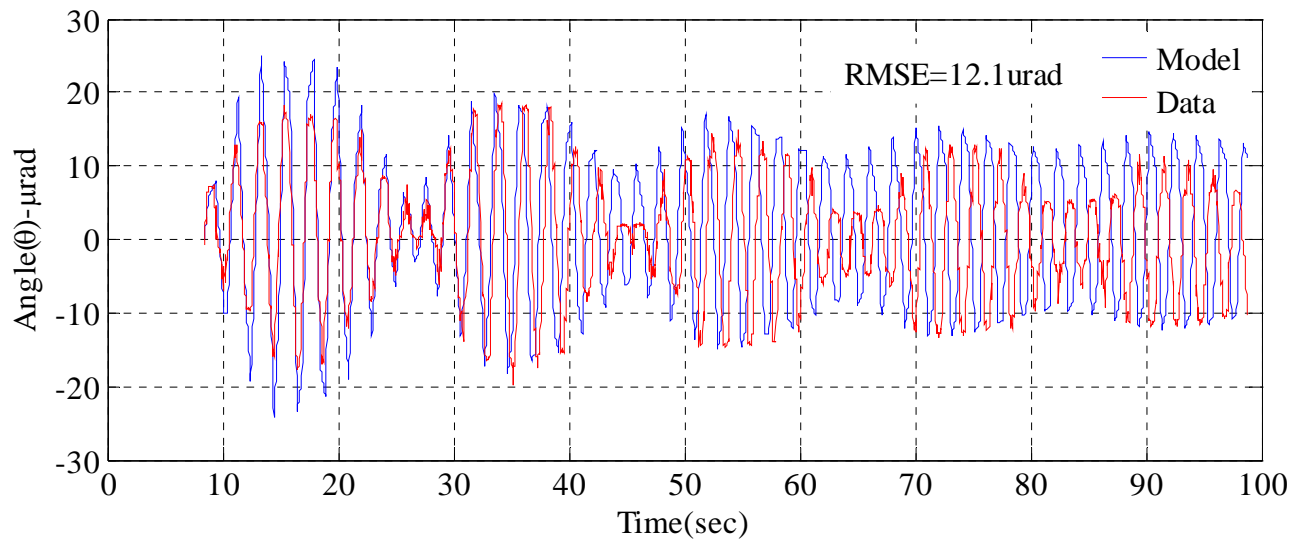
(a) Entire pulse train with data

From (a) of Figure 37, there was close agreement between the model and the data, the model has the rougher edges because of the sampling period of the simulation. Smaller sampling will smooth out the irregular tips of the model plot. The first 50 seconds are shown in (b) of Figure 37.
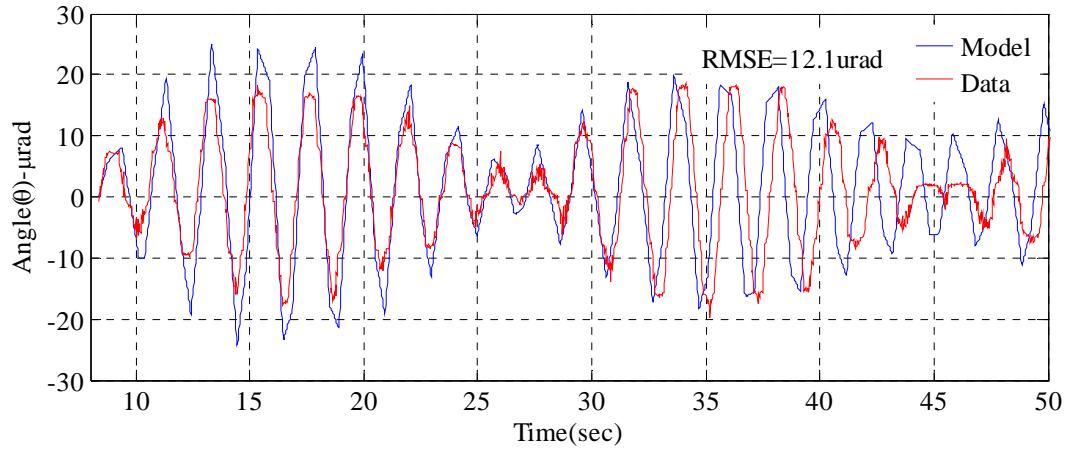
(b) Close up of the first 50 seconds of the pulse train

Figure 37. 1.697J result for 15V

Table 6. Ibit at all voltages and frequencies for 1.697J

Voltage	Frequency (Hz)	Ibit (µN-s)
17.5	2.0	105.68
15.0	2.0	109.11
12.5	2.0	70.11
20.0	1.5	65.96
17.5	1.5	71.17
15.0	1.5	72.13
12.5	1.5	109.23
20.0	1.0	67.16
17.5	1.0	77.07
15.0	1.0	68.16
12.5	1.0	60.73
20.0	0.5	95.17
20.0	0.5	66.15
17.5	0.5	61.07
17.5	0.5	54.83
15.0	0.5	73.03
15.0	0.5	62.24
12.5	0.5	70.04
12.5	0.5	52.30
Mean Ibit (µN-s)		**74.28**
Standard Deviation (µN-s)		**17.49**

65

The average Ibit for the 1.697J setting is 74.28 μN-s for all runs. Looking at Table 6, the Ibit would appear to increase as the frequency of operation of the thruster unit increases. The reason is if the pulses are faster, there is less time between firing and the propellant face does not cool as much as it would at the lower operating frequencies. Less energy is required to ablate the propellant, still hot from the previous pulse, and more energy will go into ionizing and accelerating the propellant, to a high Isp, resulting in a larger Ibit though the momentum transfer of the ionized Teflon™. The next set of data examined is the 1.6J data.

The next set of data examined was the 1.6J data from 12.5 to 20V and shown in (a) and (b) of Figure 38. In this data, the ringing and oscillatory nature of the torsion balance for an impulsive thruster is evident
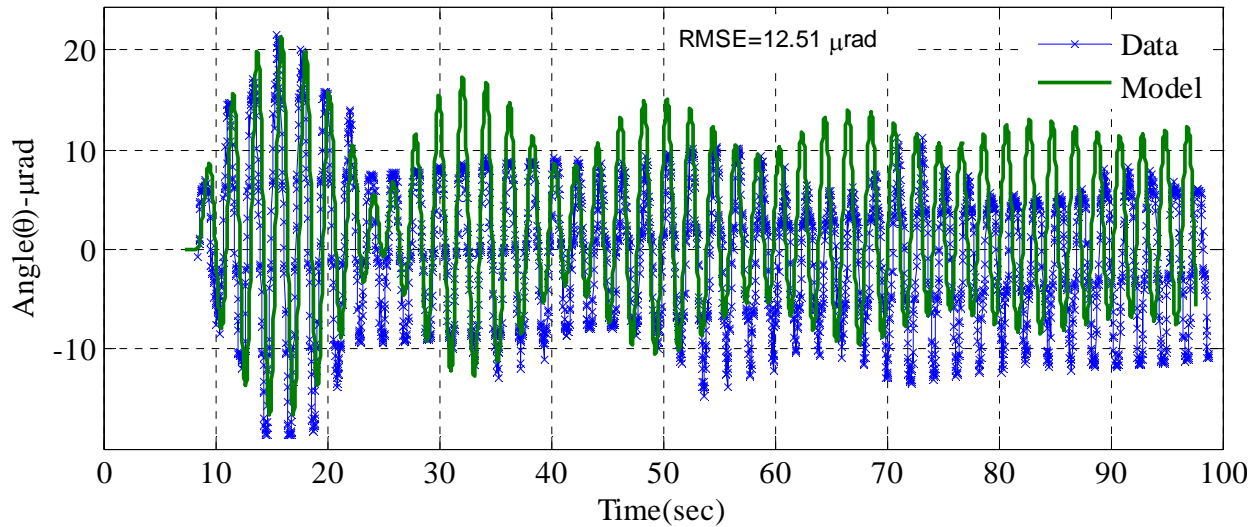
(a) 1.6J Entire pulse train, showing data and model

The oscillatory ringing observed in the 1.6J pulse train, results from the thruster providing impulse bits in resonance with the motion of the balance and increasing until the maximum deflection is reached. The large 'hills' in the data show the effect. The average Ibit over all frequencies and discharge energies is 36.1 μN-s with a RMSE of 12.51 μrad. The statistics are summarized below in the table for the all the runs at 1.6J.
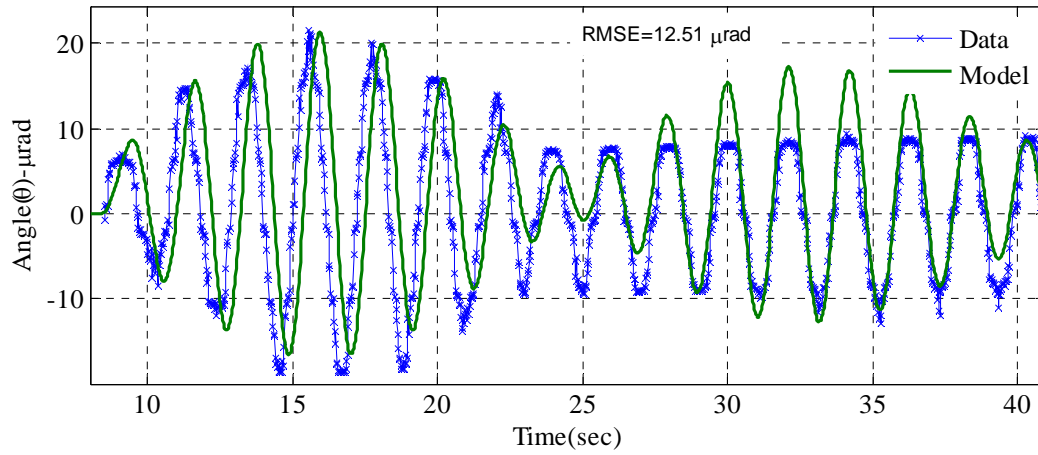
(b) 1.6J Pulse train, first 40s showing data vs. model average Ibit is 36 μN

Figure 38. 1.6J Pulse train, comparing model, and data

Table 7. Ibit values for 1.6J at all voltages and frequencies

Voltage	Frequency(Hz)	Ibit (μN-s)
12.5	2.000	55.35
15.0	2.000	43.47
17.5	2.000	42.96
20.0	2.000	42.87
12.5	1.500	29.73
15.0	1.500	29.90
17.5	1.500	16.19
20.0	1.500	30.59
12.5	1.000	36.29
15.0	1.000	32.68
17.5	1.000	35.71
20.0	1.000	38.85
20.0	0.627	38.19
12.5	0.500	31.22
15.0	0.500	34.71
17.5	0.500	36.81
20.0	0.500	37.76
Mean Ibit (μN-s)		**36.08**
Standard Deviation (μN-s)		**8.20**

From this table, the Ibit does have a slightly higher at the higher voltages, with the exception of the very first measurement. The one unusual thing about this data is the Ibit was significantly lower than the thrust observed and calculated from the other discharge energies. The exact reason is unknown, but one reason could be that the sizing of the μPPT sticks are not favorable for this discharge setting or affected by the time constant 1/RC of the circuit powering the thruster sticks. The complete spreadsheet of test conditions was placed in appendix B. The next set of data will consist of the 1.4J data. The 1.5Hz data is in Figure 39. The next set of data that was collected and analyzed is the 1.4J data, and a plot of which is shown in Figure 39.
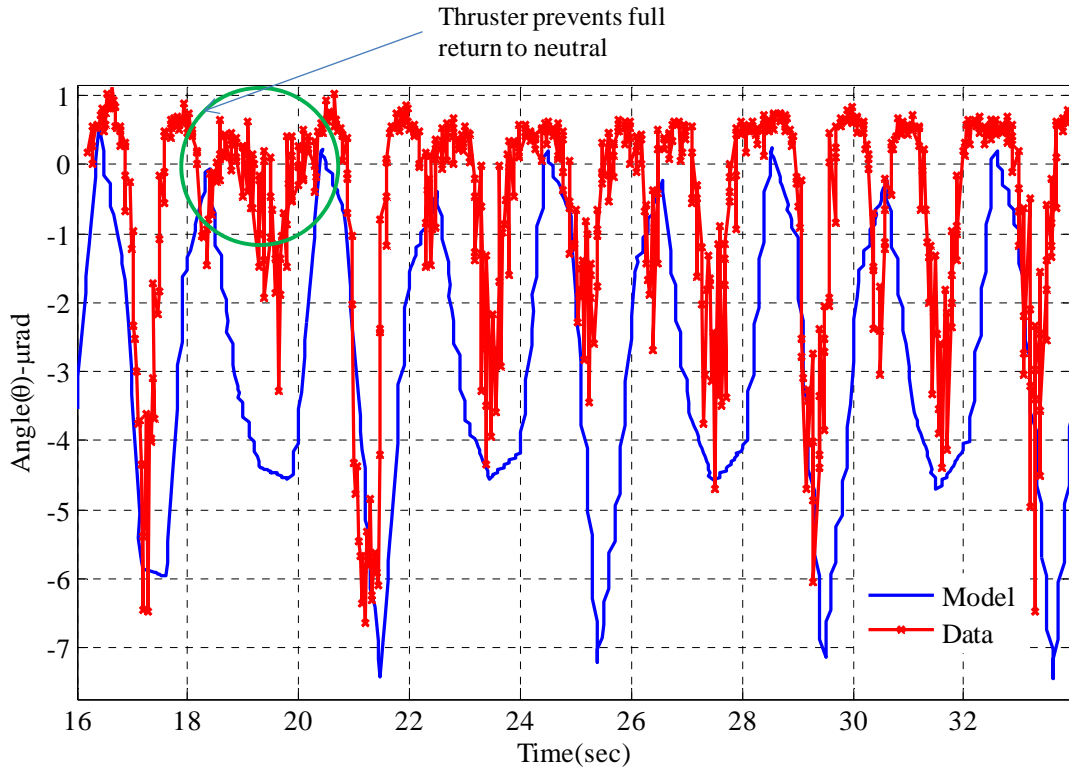
Figure 39. 1.5Hz 1.4J at 20V

The RMSE was approximately 3.6 μrad for the 1.4J data slice in Figure 39. The average Ibit for all the 1.4J 0.5Hz runs was approximately 92 μN-s, and the average over all runs is 79.91 μN-s as shown in Table 8. This result is consistent based on the period of the calibration pulse of

1.357 seconds, and a natural frequency of 4.63 rad/s. The deflection is lower than some of the other plots with smaller Ibit values, because the effective spring constant is so much larger in this case requiring a greater impulsive force for the same amount of displacement via Hook's law for a torsional spring ($F(t)*r=k_{spring}\theta(t)$). The interesting aspect of this data is the fact that the firing frequency is fast enough to keep the arm from returning fully to neutral as annotated in Figure 39

Table 8. Ibit for 1.5Hz, 1.4J data at all voltages and frequencies

Voltage	Frequency (Hz)	Ibit (μN-s)
12.5	2.0	49.70
15.0	2.0	85.46
17.5	2.0	88.60
20.0	2.0	99.06
12.5	1.5	91.80
15.0	1.5	58.99
17.5	1.5	55.20
20.0	1.5	77.65
12.5	1.0	96.53
15.0	1.0	97.08
17.5	1.0	87.87
20.0	1.0	82.04
12.5	0.6	33.83
15.0	0.6	30.49
17.5	0.6	63.30
20.0	0.6	70.88
12.5	0.5	107.89
15.0	0.5	106.83
17.5	0.5	107.52
20.0	0.5	107.52
Mean Ibit (μN-s)		**79.91**
Standard Deviation (μN-s)		**24.25**

The other phenomenon observed was the resonance due to the forcing function having

the same frequency, roughly as the torsion balance. Previous research using the balance

indicates its natural frequency should be in the 0.62-0.67 Hz range. Resonance was very

pronounced at two frequencies, one at 0.668Hz and another mode present around 0.627 Hz. A

graph showing the phenomenon of the 0.668Hz resonance is in Figure 40. In this graph, the

resonance builds to the point where it is almost as large as the calibration pulse caused by the

electrodes. The force between these electrodes is 919.22 µN when they are exactly 1.0 mm

apart.
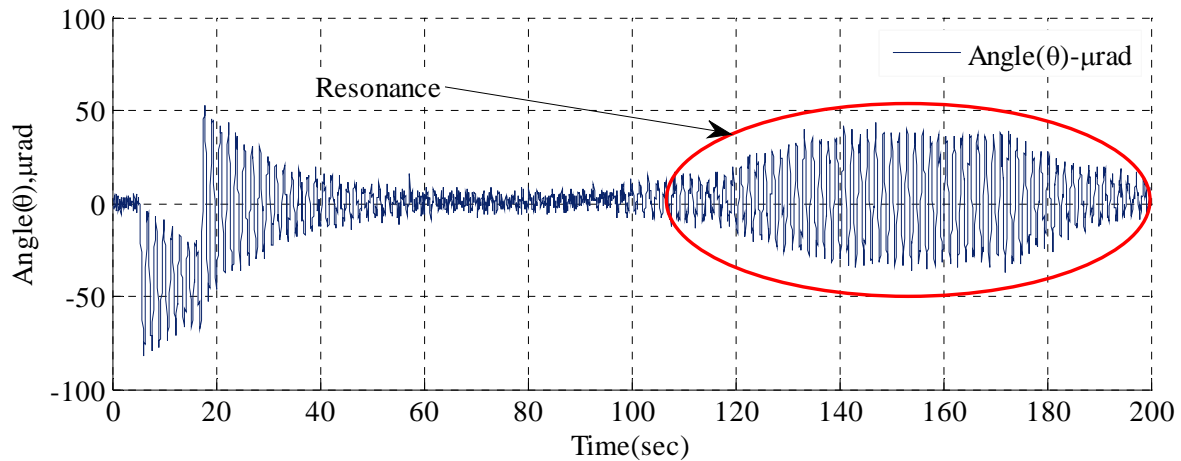
Figure 40. Resonance at 0.668 Hz when firing frequency of thruster is equal to natural frequency
of torsion balance

For the resonance to build to this magnitude, the forcing function of the thruster is exactly

in phase with the oscillatory motion of the balance, and is analogous to the construct interference

and resonance of wave of water or light in physics. The frequency of 0.668 Hz corresponds to a

period of about 1.497s. The reason for wanting to know the resonance frequency is that the

frequencies and modes of oscillations are typically bad for structural and mechanical stress

reasons. In this case, however, they can mask the true effect due strictly to the thruster

operating. Selstrom [13] estimated that the natural frequency of the torsion balance should be

around 0.66 Hz, which is close to 0.668. The balance exhibited some modal responses similar to Figure 40 but did not reach the same magnitude; the frequency of this response was around 0.627 Hz. This frequency did not pose any problem for data acquisition, because the test frequencies were at 0.5, 1, 1.5, and 2 Hz. These frequencies are far enough from the 0.668 Hz to avoid the excessive oscillations leading to resonance.

The next set of data to analyze was the 1.3J case. Sometimes, the graph needed shifting left or right, so the simulation and the data had the same starting point at t equal to zero. This shift was only for comparison purposes and did not change the relationship between the physical responses of the torsion balance to the thruster as shown in Figure 41. The RMSE was 3.37 μrad for this sample set. With some of the graphs, not all the points match up, because of experimental error associated with the equipment and taking measurement.

For instance, at 100 μV, which is the lowest value the noise level reduced to, correspond to an angle of 0.827 μrad, so the data and model are at least off by this amount at a minimum amount, but is at least 6 times lower than the value typically seen, from 4.0 to 10 μrad. The average Ibit value for the 1.3J setting was around 71 μN-s. The standard deviation for this data set was 17.82 μN-s. The results are in Table 9. The model matched the data closely, once the initial conditions are considered, and added to the simulation as an initial state vector, contain the initial angle, θ and the angular velocity, $\dot{\theta}$. The transient response of the model compared to the data was very sensitive to the initial conditions. If they were not matched properly, then the two would become out of phase much quicker than anticipated and may not match up as well, since the forcing function from the thruster takes time to imparts its frequency characteristics on the torsion balance system.
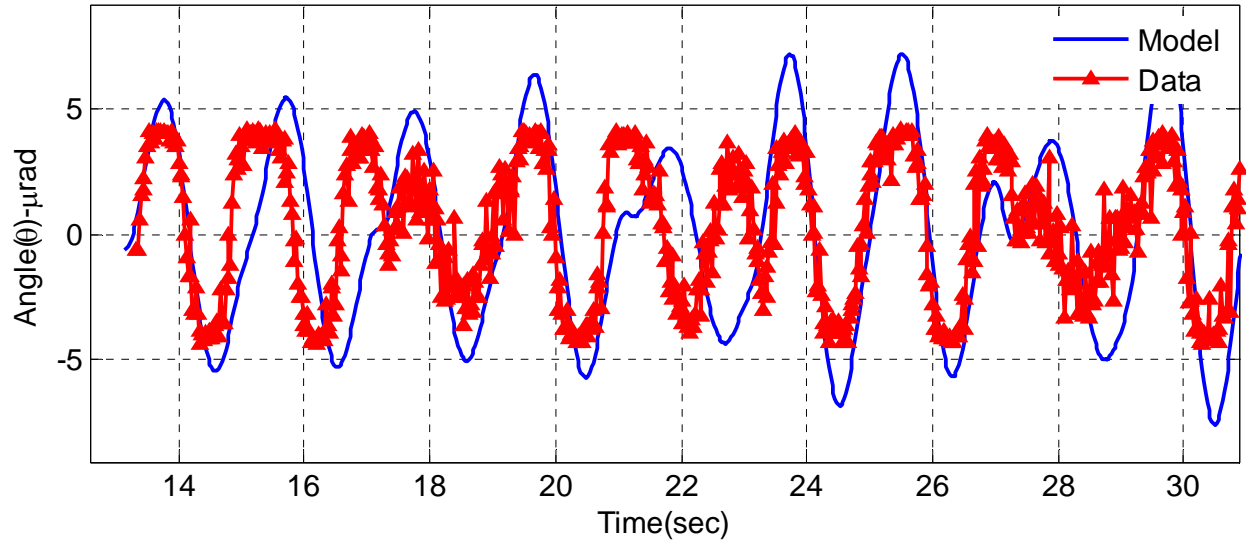
Figure 41. 1.3J data at 0.5Hz and 12.5V

Table 9. Ibit for 1.3J over all voltages and frequencies

Voltage	Frequency	Ibit (µN-s)
12.5	2.0	78.87
15.0	2.0	84.16
17.5	2.0	60.82
20.0	2.0	42.87
12.5	1.5	55.69
15.0	1.5	96.21
17.5	1.5	73.93
20.0	1.5	82.49
12.5	1.0	62.65
15.0	1.0	39.97
17.5	1.0	67.14
20.0	1.0	82.43
12.5	0.5	56.32
15.0	0.5	95.27
17.5	0.5	88.99
Mean Ibit (µN-s)		**71.19**
Standard Deviation (µN-s)		**17.82**

The last set of data in the top portion of the data matrix is the 1.2 J data which and shown in Figure 42. The Ibit required for convergence is in the 59 µN-s range. This case is one where the drift was a significant hindrance to calculating the thrust. The drift likely caused by center of gravity error, resulting from poor placement back in its holder on the base. Fortunately, it is a linear function of distance and eliminated mathematically from the response of the torsion balance as was done with the case here. This setting had the lowest average thrust with the exception of the 1.6J data shown previously in Table 7. The results of the 1.2J setting are shown Table 10.

Table 10. 1.2J Ibit at all voltages and frequencies

Voltage	Frequency	Ibit (µN-s)
12.5	2.00	70.18
15.0	2.00	91.72
17.5	2.00	47.02
20.0	2.00	92.25
12.5	1.50	68.47
15.0	1.50	38.72
17.5	1.50	102.45
20.0	1.50	62.64
12.5	1.00	58.02
15.0	1.00	42.86
17.5	1.00	32.02
20.0	1.00	57.39
12.5	0.50	62.09
15.0	0.50	41.10
17.5	0.50	27.43
20.0	0.50	58.70
Mean Thrust (µN-s)		59.57
Standard Deviation (µN-s)		21.85
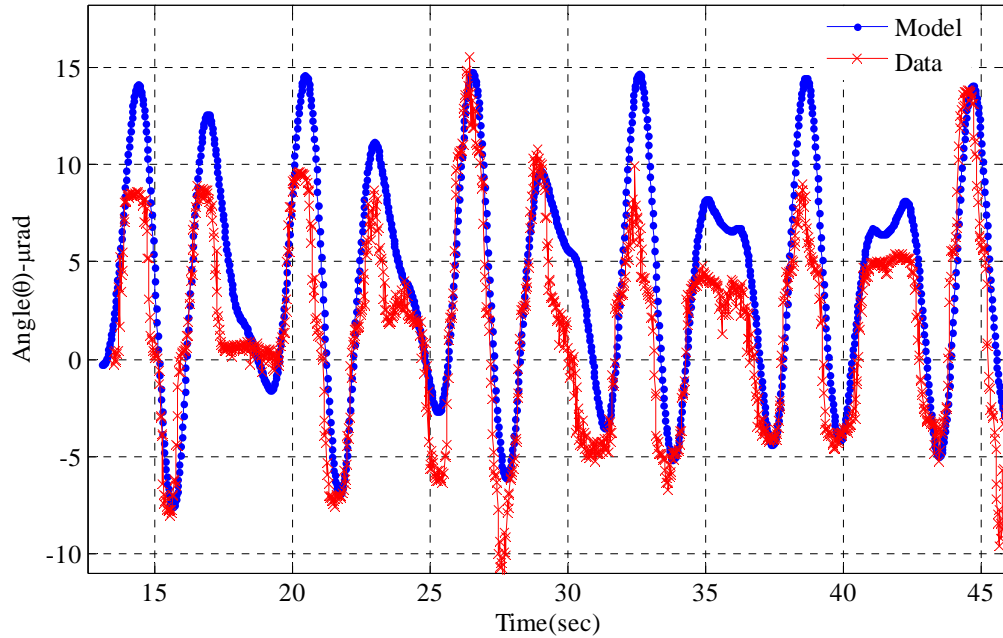
Figure 42. 1.2J, 1.531Hz 15V

Now that the solutions to the response of the torsion balance can be accurately modeled using ODE solution techniques, and the average thrust for each discharge energy setting was found, the next step was to correlate the thrust to other parameters of interest like the discharge energy frequency, and supplied power. We will now make some observations about the overall testing.

All the Ibit values were plotted as function of frequency to see if there was any correlation between the Ibit and the frequency of operation. The Ibit values seem to increase in general with high frequency, but more samples would need to be taken at the various frequencies to verify this result. A scatter plot is shown in Figure 43. Statistically speaking, they are all very close to the same value and have similar standard deviations, which places the average Ibit around 72 μN-s for all thrust values, considering discharge energy and voltage input. The standard deviation for the each data is larger for a single frequency, than between frequencies.

74
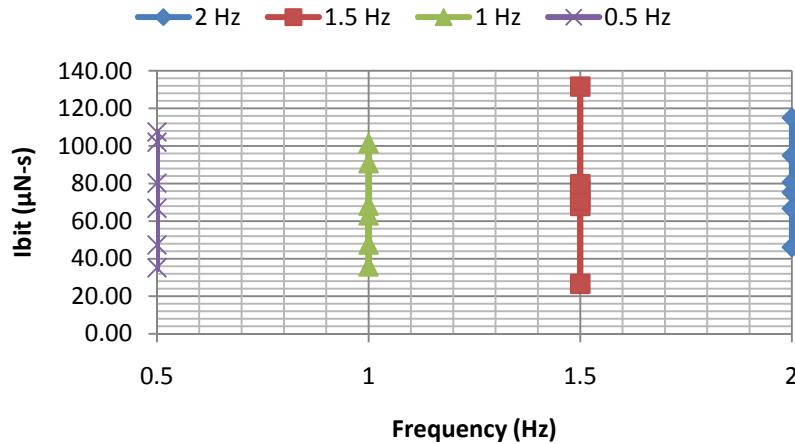
Figure 43. Chart of Ibit values vs. frequencies

The other objective besides examining the performance of the thruster due to variations in discharge energy and input voltage, was to attempt to determine the torques produced by the sticks separated by some distance.

Torque Calculations

The other goal that was set out was to determine the torque difference if any, that could be measured by the torsion balance. Due to time restrictions, only data at 1.3 and 1.2 J were completed out of the original planned matrix.

The torque was calculated using the difference in deflections caused when stick 8 or stick 3 of the GG-µPPT. Stick 8 was the stick further of the two from the rotation axis of the balance. The distance between the stick centers is 0.585 in. (.0149 m). This difference in length is what is responsible for the difference in torque produced between the two sticks assuming that the thrust produced is the same for both sticks, which considering the close agreement of earlier data is a safe assumption to make. The thrust was obtained by dividing the Ibit by 1.0 s, the pulse width used in the model. Neither of these sticks were contaminated with carbon build-up, further increasing confidence in this assumption.

Table 11. Torque difference produced between stick 8 and 3 at 1.3J

1.3J stick	Voltage	Thrust (μN)	Rstick (8)-m	Rstick (3)-m	Torque(μN-m)	Delta Torque (uN-m)
8	12.5	92.20	0.203	0.191	18.70	
3	12.5	81.50	0.203	0.191	15.60	3.127
8	15.0	79.50	0.203	0.191	16.10	
3	15.0	45.80	0.203	0.191	8.74	7.367
8	17.5	59.60	0.203	0.191	12.10	
3	17.5	35.60	0.203	0.191	6.79	5.284
8	20.0	21.30	0.203	0.191	4.32	
3	20.0	20.20	0.203	0.191	4.09	0.236
Delta Torque (Avg)- μN-m						**4.003**

Table 12. Torque difference produced between stick 8 and 3 at 1.2J

1.2J stick	Voltage	Thrust	Rstick (8)-m	Rstick (3)-m	Torque(μN-m)	Delta Torque (uN-m)
8	12.5	86.70	0.203	0.191	17.60	
3	12.5	91.30	0.203	0.191	17.40	0.122
8	15.0	80.40	0.203	0.191	18.90	
3	15.0	99.20	0.203	0.191	16.30	2.638
8	17.5	95.30	0.203	0.191	20.20	
3	17.5	106.00	0.203	0.191	19.30	0.924
8	20.0	71.00	0.203	0.191	21.50	
3	20.0	75.40	0.203	0.191	14.40	7.08
Delta Torque (Avg)- μN-m						**2.691**

From Table 11 and Table 12, there is a small difference between the two but hardly noticeable and requires the noise floor and external vibrations to be as minimal as possible. Though a torque produced, it is small compared to the actual magnitude of the thrust itself. With the average for 1.3J at 4 µN-m of torque, the average thrust (Ibit/pulse duration) is somewhere between 70 and 100 µN and amounts to only six percent of the thrust produced by each µPPT thruster stick. These thrust levels are not large enough to rotate a CubeSat with a mass of few kilograms. It is safe to say that the separation between the sticks on the GG-µPPT module will not result in a nutation of the CubeSat.

Observations

There were several important things discovered about the operation of the thruster as it was firing. The first thing found was the thruster has a minimum voltage required for operation higher than the lowest value stated in the operations manual.

Discovery number one, the GG-µPPT minimum operation voltage is between 10 and 12.5 volts. During, preliminary investigation of the thruster, the input voltage was turned to the lowest recommended setting of 10V. Everything else on the thruster was powered on and ready for operation. When the frequency knob on the stick selector module was turned on, none of sticks fired. Had these sticks fired, the Cublock™ software and the firmware in the thruster would have relayed a signal indicating a fire or misfire of the thruster as shown in the screen in Figure 44. This screen contained other useful information about the behavior of the GG-µPPT thruster module. For example, it would display the time between firings, essential in determining the frequency of the forcing function that went into the MATLAB™ and Simulink™ models. It also contained very useful information like the discharge voltage of the

main capacitor and the trigger capacitor, it tracked system time and the number of misfires for a given μPPT stick.
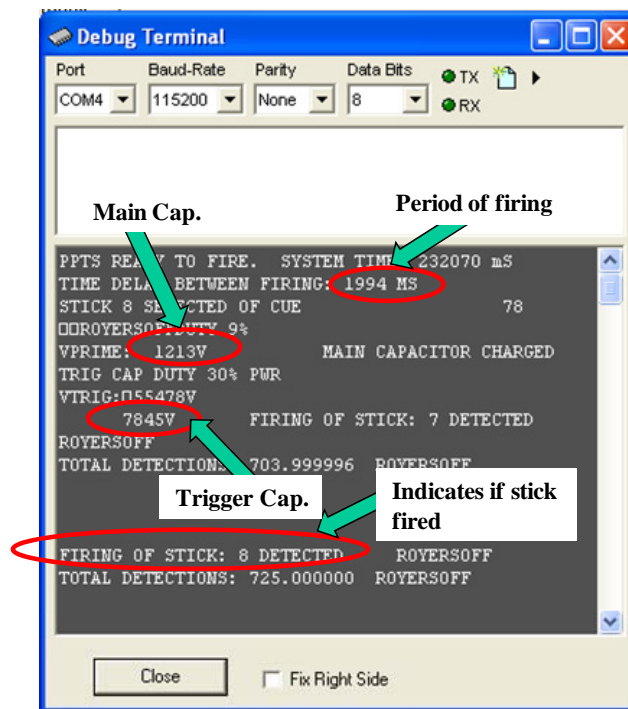
Figure 44. Screenshot of cublock™ debug terminal

In this screenshot for instance the voltage of the trigger capacitor is 7845 volts, and the main capacitor is discharging at 1213 V, about 1.47J discharge energy. There would have also been a flash of light that would have been observed through the side viewport on the left side of the vacuum chamber as well, and would have looked like bright blue flashes shown in Figure 45. This result is important for the satellite this device is intended for, because of voltage requirements. The exact cutoff voltage for operation was not determined, but operation at 12.5 volts allowed continuous thruster module operation. So the limit is somewhere between 10 and 12.5 volts. The flashes of light were also dimmer at the lower voltage settings of 12.5 volts vs. 20 volts. The viewing stand shown in the equipment section in (a) of Figure 27, made it relatively easy to see the operation of the thruster in the confined space of the vacuum chamber.

At times, there were instances when the sticks would misfire or two to three of them would fire rapidly in succession. The thruster side window was on the left side, looking towards the front of the chamber.

(a) Orientation of thruster/mirrors   (b) High-resolution of picture
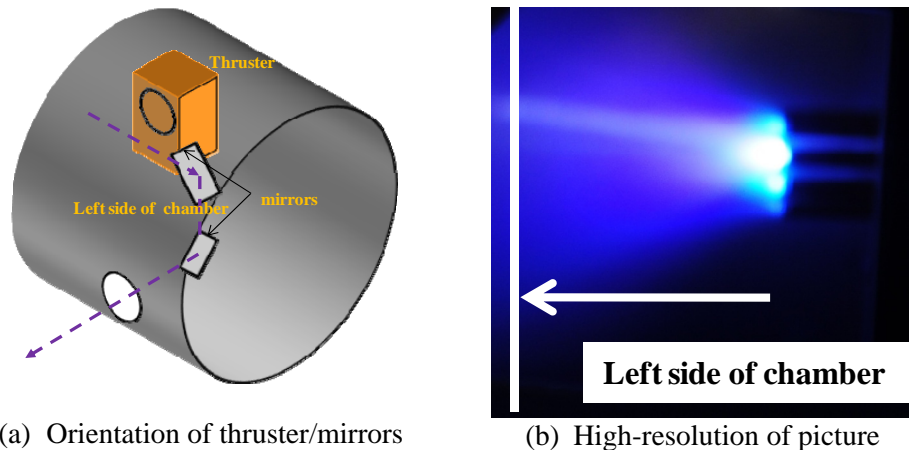
Figure 45. Side profile operation of GG-PPT

Discovery number two was while the thruster was operating, not all the sticks accumulated carbon during operation, or at the same time for those sticks where carbon deposit buildup did occur. The first stick to have a visible carbon buildup on the Teflon™ surface was stick number seven. Each time the thruster was removed out of the vacuum chamber for reprogramming, pictures of the thruster and thruster heads were taken. Each thruster head was inspected to check for cracks in the surface or damage to any of the electrode surfaces. In general, the center electrode and cathode receded away with the Teflon™ as expected. The surface however did not remain entirely flat, some of the thruster sticks had a 'bowl' or curved Teflon™ surface. The sticks were still firing reliably throughout testing.

Looking at (b) of Figure 46, the bowl or conical depression in the Teflon is visible. The inner electrodes visible in the center of each stick, also recedes with the Teflon™ as designed during thruster operation. The initial thought was the thruster plume could be returning to the surface of the thruster, because it is in close proximity to the wall of the chamber. If that was the

only source then all the thrusters should have equal amounts of carbon on them statistically speaking.
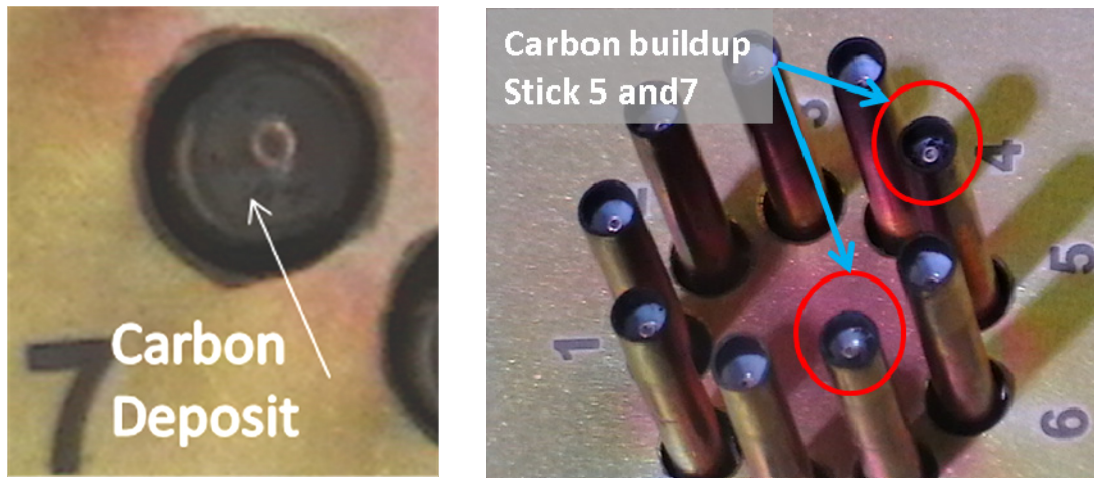
(a) Close-up of stick 7   (b) Contamination now present on sticks 5 and 7

Figure 46. Carbon build-up on thruster heads

From (a) in Figure 46, the carbon build up on this sticks is shown by the arrow, sometimes the thrusters would discharge prematurely or more rapidly than would be expected, based on the set firing frequency for the thruster module. These carbon deposits are semiconductors when they are hot and vaporized and could lead to some shorting of the potential between the cathode and the inner electrode. The other noticeable effect on the data was if the thruster center of gravity, C.G was either forward or back of the counterweight C.G. This effect showed up as a positive or negative drift of the waveform observed.

Discovery number three, the high drift rates are due to CG location error and tension changes in wiring. If the drift rates were thermal in nature, they would likely have averaged out to about the same amount each time. However, some of the rates were has high as 10 μrad over a 100 s period indicating the source was due to something else. The drift rates were also consistently negative. The wires had some associated weight with them and not easily accounted for in the center of mass calculations discussed earlier.

Figure 47, provides an example of the drift present in some of the data that had to be corrected. The figure depicts the raw change in LDS voltage vs. time, and the negative drift due to mirror moving further from the LDS tip is evident from the negative constant slope of the data in Figure 47. However, because it was linear, it was a simple correction factor to make to the original data file and turn it into a graph similar to Figure 48. This technique was applied to the data for accuracy and consistency. had to done to the files earlier allow the plot of the data against the model to make sense. Once adjusted, the data could then be compared directly against the ODE model for the system, and the thrust corresponding to the minimum RMSE with the same timing frequency as the thruster could be found. Initial thoughts were the thruster may be forcing the drift. If the thruster was the cause, the drift would have been in the opposite (positive) direction, the direction the the torsion arm moves, moving the mirror closer to the LDS tip. Correcting the data for the center of gravity error allows the MATLAB™ to assume that there is no placement error when running the simulation. The result is the ability for the code to converge and find a minimum RMSE value for the specific thrust accurately.
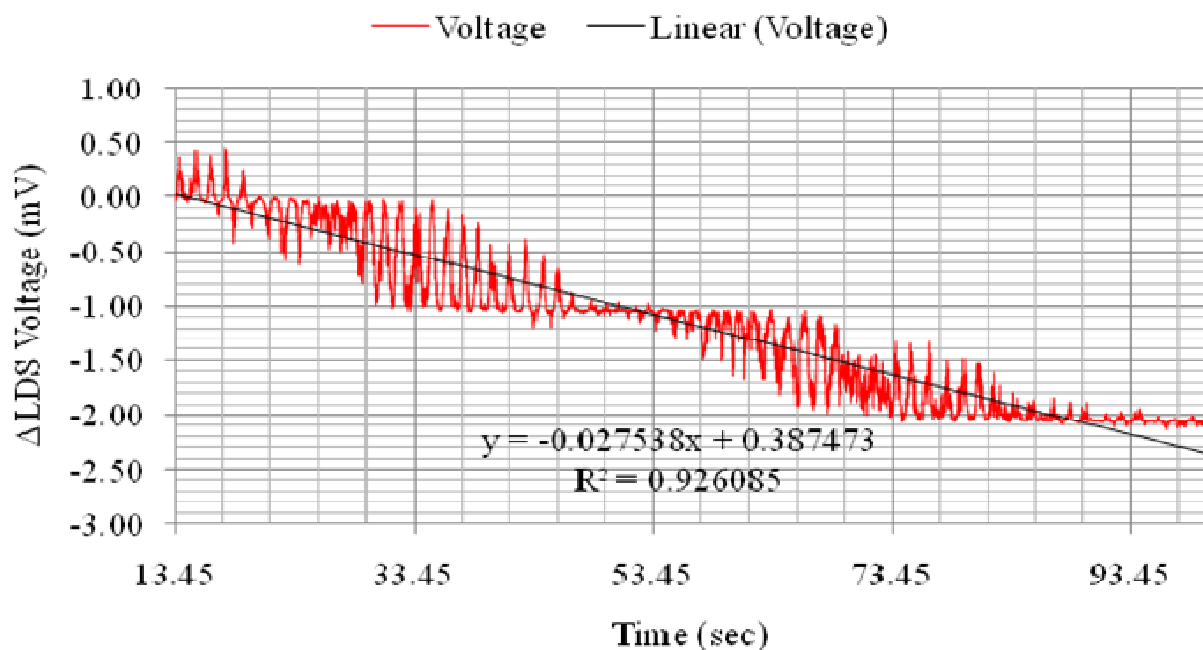
Figure 47. Uncorrected data with drift rate

81
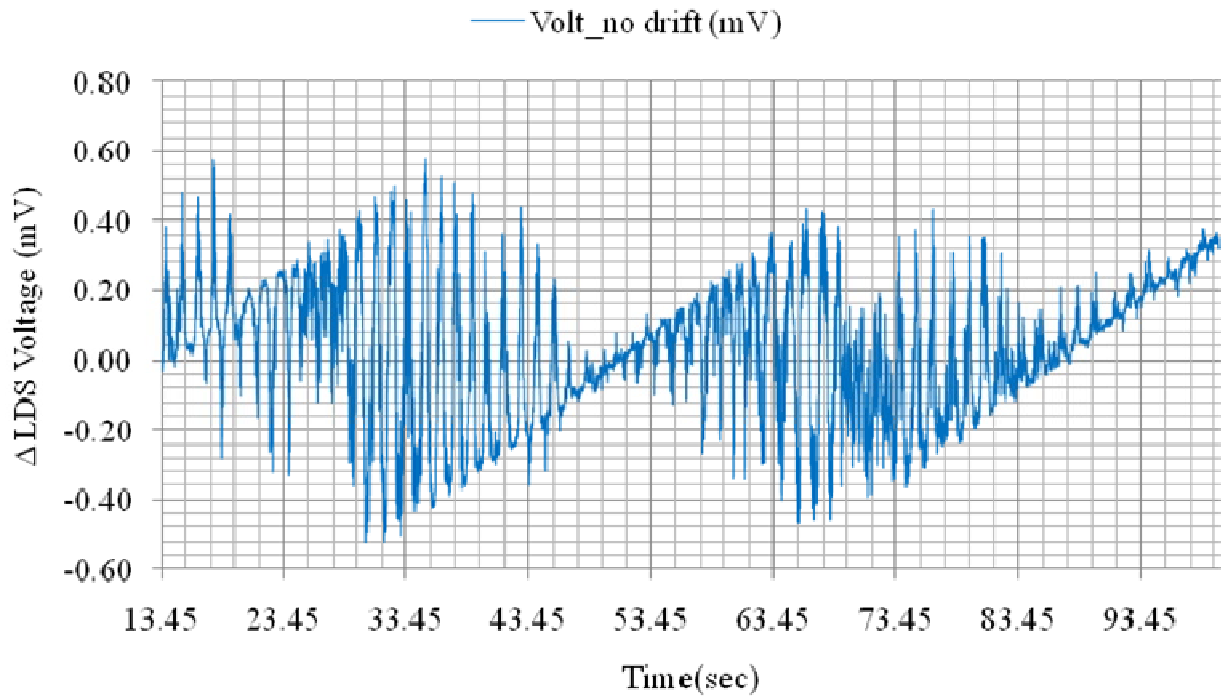
Figure 48. Corrected data without drift

Discovery number four, the thrust is primarily a function of discharge energy and firing

rate. The voltage did seem to increase slight at 20 volts, but this was not always consistent

across discharge energies. In some cases, for example the 12.5 volt setting produced more thrust

than the 20 volt setting for the same discharge energy. However, the chart in Figure 43 indicates

that there is a small but noticeable increase in the average thrust as the firing rate is increased.

This is increase was unexpected initially. The power supply will maintain constant

voltage, and the capacitor will only charge to the voltage set by the discharge energy setting. So,

increasing the voltage without increasing discharge energy has little effect on the calculated

thrust from the thruster. However, if the voltage is insufficient, then the electronics cannot

amplify the given voltage to the level needed for discharge, and was seen, when powered at only

10V, the thrusters would not fire at all.

Error Analysis

   This section on the error analysis, identifies the various sources of error in the research experiment. We begin by discussing the noise present in the signal coming from the LDS, and the signal to noise ratio. From there the error associated with the sample time and time steps chosen are discussed, and then measurement error in the output of the Agilent 54622D Mixed Signal Oscilloscope. Next, we generate some normal probability and histogram plots for the thrust data. We end this section with discussion on the norm of the residuals

  Signal to Noise (SNR)

   The biggest source of noise was the high frequency turbo-pump and the surrounding N_2 pumps that were co-located in the lab where the research was performed. The signal-to-noise, SNR ratio is a useful quantity to determine how much stronger the signal is than the noise floor of the environment. Initially the oscilloscope was used as is. Early attempts were made to collect quality data, but the noise floor was around 10mV and much too high to accurately see the motion of the balance due to thruster operation without extensive signal processing techniques.

   Most of the pulses on average were only one or two mV in magnitude. Operating key features of the oscilloscope like the high frequency noise rejection mode, eliminated sources greater than 50Hz in frequency greatly reducing the noise present in the signal. The data sample was averaged using the previous point, and resulted in a cleaner signal, and eliminated much of the random noise present.

   With these settings, the noise floor was reduced from 10 mV to approximately 100 to 260 µV. This corresponds to an increase in detection sensitivity of 38X. This was especially important in this research, because of the relatively massive thruster and counterweight. Other individuals had thrusters, but one of them was only one-tenth the mass of the GG-µPPT module.

An increase by a factor of 38 is easily converted to decibels, dB and is the common unit way of measuring the power and intensity of signals in the electrical/acoustical engineering world. The value in dB was found using the formula:

$$dB=10 \log \frac{P_{out}}{P_{in}} = \frac{I_o}{I_{in}}$$

(33)

P_o, I_o is the power or intensity output and P_{in}, I_{in} is the power or intensity input respectively. Substituting numbers into the equation, the value corresponding to this change was from 10 mV to 260 µV is +15.8dB for example.

Time Step Resolution

The impulsive nature of the thruster and the relatively short pulse of the thruster and oscillations required instrumentation capable of measure brief instants in time but enough memory capacity to store a couple of minutes of data during a experimental run. The Agilent 54622D Oscilloscope has a dynamic range from 5.0 ns to 50.0 s. This range covers the fastest of familiar events. At 5.0 ns, even a beam of light travelling at 670 million mph will only travel about 5 ft! The original data files had two to four million data points, but was discovered to cause problems during data analysis, because of the time required/and computing resources. A decision was made to reduce this number to 4000 data points per run, which Excel could handle for quick assessment on the quality of the data.

Measuring Instrument Error.

The error associated with taking the masses of the counterweight are +/- 0.1 g for the scales that were used in ASYS 632-Satellite Design and Test. The calipers used for measuring the distances on the torsion balance had accuracy down to 0.01 mm or 0.397 mil. The Agilent 54622D oscilloscope had a dynamic range in voltage of 5V to 1 mV/division.

Data Error and Statistics

The statistics have been tabulated for all the Ibit data and shown in and

Table 13. The maximum Ibit appeared to be around 1.47J.

Table 13. Mean and standard deviation statistics

Discharge Energy (J)	Mean Ibit (uN-s)
1.47	108.79
1.69	77.43
1.6	35.54
1.4	81.19
1.3	71.56
1.2	59.57
Total	**72.35**
	Standard Dev.,σ (μN-s)
1.47	23.35
1.69	17.49
1.6	7.82
1.4	8.20
1.3	17.82
1.2	21.85
Total	**16.09**

The largest standard deviation is from the 1.47J data with a standard deviation of 23.35

μN-s. All other values have standard deviations that are smaller. The total average Ibit for this

thruster over all energies and frequencies is approximately 73 μN-s and comparable to other

micro-thrusters with similar power requirements. Busek tested these sticks at 1.96J, and

indicated a average Ibit 153 μN-s as the starting max for the μPPT sticks, and 80 μN-s was the

average throughout the life of the thruster until all propellant has been consumed according to

the operations manual and shown in Figure 49. The average mass loss per pulse was around

19.71 µg/pulse, according to the manufacturer, with a Isp of 827s [25]. The Isp corresponds to a

velocity of 8110.1 m/s or 26,609 fps.
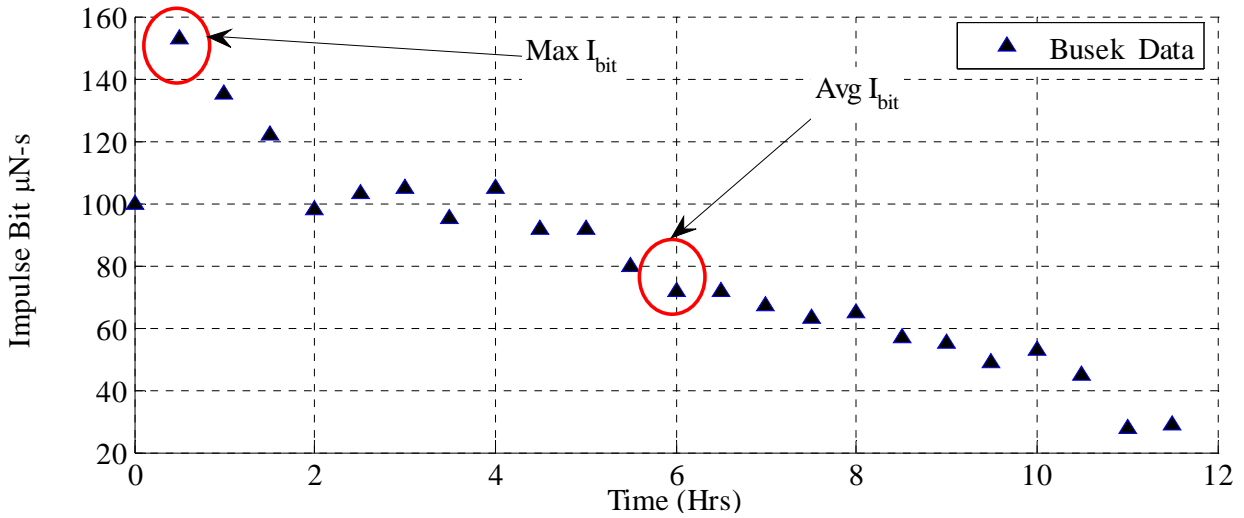
Figure 49. Manufacture's Ibit performance

Table 14. Summary statistics for all data

Parameter	Min	Max
Max Ibit-µN-s	157.00	
Ibit avg. (all data)-µN-s	72.75	
Standard Deviation (avg./max)-µN-s	14.00	24.00
Number of firings	24216.00	
Test Conditions	112.00	
Torque(µN-m) 1.3J	4.00	
Torque (µN-m) 1.2J	2.69	
Power Consumed (pulsed min/max)-W	31.80	35.40

Thrust efficiency was determined once the discharge energy, pulse time, the velocity and mass loss rate are known. For example, at 1.47J/shot and using the mass loss of $19.71*10^{-9}$ kg/shot and u_e equal to 8110.1 m/s, results in a theoretical efficiency of about 31 percent using equation (12). This is just the thruster efficiency. The total efficiency will be less than this because of the all the heat losses of the electronics in inside the GG-μPPT and the heat lost to producing hot neutral particles, not accelerated by the Lorentz Force. The thruster efficiency was determined to be about 21% in this research, but that does not include the losses from the internal electronics of the GG-μPPT device. Factoring these in, the actual efficiency is probably close to historical values of 6-10 percent.

In summary, the errors of the instrumentation and the test collection tools were at least four to 10 times smaller than the signal analyzed and collected from the oscilloscope. Moving the roughing pump off the stand and using the noise rejection features of the oscilloscope resulted in a much better SNR, making data analysis and model fitting much easier. The high frequency noise is random and in nature, and removed using filtering techniques. The error between data collected in this research and Busek is 2.6 % for the maximum value and 9.1% for the average. .

V.   Conclusions and Recommendations

The final chapter of this research take the information gathered from the thrust, plots, photographs, error plots and statistical fitting to determine the best conditions to operate at, and the test conditions that were accomplished. Next, recommendations are made to individuals following up with this research or upgrading the torsion balance to be adjustable once down to vacuum conditions. Finally, there is some discussion regarding the future work on this device.

Optimum Voltage and Energy Operating Conditions

The first major finding is the Ibit appears to decrease with a decrease in discharge energy. However, from the graphs presented in chapter four, some variation with the data as is present as the conditions change and the thruster moves in and out of the chamber during reprogramming, and effectively change the spring constant. This is a concern because spring constant that is too stiff will prevent the signal from being above the noise floor. The total average for Ibit across all runs is 73 μN, close to spec. The best setting to operate the GG-μPPT is **20V 1.5Hz at 1.47J for maximum Ibit of 157 μN-s**. The next best setting is at 1.4J and provides approximately 83 μN-s of impulse.

Earlier Ibit levels that were calculated were about 181 μN-s, but that number was slightly too high for two reasons. First, the sensitivity constant of -0.4V/mm or -400 mV/mm that was used is slightly too low. Using the chart provided by Philtec™, the sensitivity constant of -15.30 mV/mil for the far side of the LDS sensor translates into -0.602V/mm or -602 mV/ mm. This sensitivity will affect the observed voltage output and change on the oscilloscope and will make thrust levels appear higher, than they really are.

Second, even though the thrust force is relatively constant, the impulse bit over time will decrease due to a larger proportion of particles not ionized as efficiently as when the thruster was new. The thruster efficiency calculated solely on the discharge energy results in a theoretical efficiency of 31 percent. The main culprit to reduced efficiency would be the particle accumulation that accrues on the surface of the Teflon™. This effectively reduces the Isp and uses more propellant resulting also in decreased efficiency.

Not all the conditions for the torque were accomplished, but torque was measured between two different energy levels at all four voltage settings for the 1.3 and 1.2J energy setting in Table 15.

Table 15 Accomplished Test Conditions

Control variables	E=$1/2CV^2$,C=2μF			
Discharge energy (J)	Output voltage	Frequency(Hz)	Stick pattern	Voltage
✓ 1.7	1303.84	0.5,1,1.5,2	1,2,3,4,5,6,7,8,9	12.5,15,17.5,20
✓ 1.6	1264.91	0.5,1,1.5,2	1,2,3,4,5,6,7,8,9	12.5,15,17.5,20
✓ 1.5	1224.74	0.5,1,1.5,2	1,2,3,4,5,6,7,8,9	12.5,15,17.5,20
✓ 1.4	1183.22	0.5,1,1.5,2	1,2,3,4,5,6,7,8,9	12.5,15,17.5,20
✓ 1.3	1140.18	0.5,1,1.5,2	1,2,3,4,5,6,7,8,9	12.5,15,17.5,20
✓ 1.2	1095.45	0.5,1,1.5,2	1,2,3,4,5,6,7,8,9	12.5,15,17.5,20
Discharge energy (J)	Output voltage	Frequency(Hz)	Stick pattern	Voltage
1.7	1303.84	0.5,1,1.5,2	3,8	12.5,15,17.5,20
1.6	1264.91	0.5,1,1.5,2	3,8	12.5,15,17.5,20
1.5	1224.74	0.5,1,1.5,2	3,8	12.5,15,17.5,20
1.4	1183.22	0.5,1,1.5,2	3,8	12.5,15,17.5,20
✓ 1.3	1140.18	0.5,1,1.5,2	3,8	12.5,15,17.5,20
✓ 1.2	1095.45	0.5,1,1.5,2	3,8	12.5,15,17.5,20

Time was an issue, because of the need to share equipment, but there is no reason to suspect that the torque difference between the sticks would be any different for the other discharge energy levels, because the relative thrust is the same for all sticks, unless contaminated or damaged. The firing of the μPPT sticks was dependable, but there was misfiring that occasionally did occur. One possible explanation for the misfiring is that the plume ion plume from the adjacent stick is sufficient to effectively short out the electric potential established by electric field that exists between the various electrodes in the thruster unit and the cathode. The cathode is rated to reach 10 kilovolts, 9,700 volts was the highest observed in research. With such a high electrical potential, even a good vacuum might allow enough particles to start an

ionization trail in addition to the charged particles coming out of the other thruster sticks, at the tight spacing of this assembly.

The very fast response of the oscilloscope allowed the capture of details like the pulse width of the thruster firing that would have been difficult to measure otherwise. There are a few recommendations put forth for the next generation of torsion balance or for an individual doing follow-on research with the GG-μPPT.

Recommendations

Torsion Balance Improvements and Considerations

There is much to say about the torsion balance provided by Busek. The sensitivity of the instrument is amazing to say the least. Very few devices can measure such small impulse bits and forces produced by μPPTs and other 'micro-thrusters' accurately, even with some background noise present. There are a couple of improvements to consider for future models or upgrades. First, I would start with the calibration process for the main and damping electrode. Under ideal conditions, the distance between the electrodes should not change significantly from the 1.0 mm position if not disturbed. However, the reality of the situation is different. The calibration process takes place in the external environment and atmosphere, and thermal gradients as well as physical changes of the sized due to pressure forces, change this distance..When the chamber is under vacuum, the dimension of the chamber due to thermal and atmospheric effects can cause the alignment of the balance to change, where the electrodes are no longer 1 mm apart. This will change the voltage to force calibration constant.

A recommended action would be to attach a separate low noise motor be connected to the micrometer with electrical connections so that the distance of 1.0 mm could be re-established once in vacuum conditions and the system is stable in terms of temperature and physical strain.

90

The other change recommended, would be the installation of some electrical connections on the base of the balance arm. One of the toughest issues was dealing with the 26 or so wires that were very stiff and overwhelmed the spring constant of the balance itself. This would reduce the amount of error in both the calculation and the data gathering. A standard serial connection and power connections would have been immensely helpful. All in all, this balance is the most sensitive thrust measuring instruments at AFIT. The instrument was so sensitive that most of the data gathering had to be done late in the evening, when the amount of external noise was as low as it could be (minus the N_2 pumps.)

Future Research

One variable for further investigation is the duty cycle of both the main capacitor and the trigger circuit on the Ibit. The default is 30 percent for the trigger, though at its maximum energy per pulse of 1.697 J, the main capacitor's duty cycle jumped to 100 percent. There was no information on the effect of this parameter on the overall performance of the thruster. Changing this parameter without damaging the internal electronics or the thrusters themselves was a principle concern, since this is a one a kind piece of equipment. I learned a great deal about electronics, plume interaction and EMI, through my research with this thruster was amazed by how brilliantly it shines. This is definitely a propulsion system that any nano-satellite program would benefit from.

In summary the highest Ibit observed was 157 μN-s, with a average of 72 μN-s across all discharge energies. In some of the plots, the Ibit seemed to be slightly higher for the higher voltages, and in others, it was not the case. Firing frequency had a more dramatic effect on the Ibit than the voltage, but overall the Ibit varies the most by discharge energy as evident in Table 13.

The photo in Figure 50, is the GG-µPPT facing the window, taken with a SLR camera with a exposure duration of five seconds, because at two hertz firing frequency, all thrusters can be captured in the photo.

Figure 50. Gatling-gun firing at 2 Hz

References

[1]   Keidar, M., Boyd, L.D., Antonsen, E.L., *"Optimization issues for a micropulsed plasma thruster,"* Journal of Propulsion and Power, Vol. 22, No. 1, 2006, pp. 48-55.

[2]   Rowan, S., and Hough, J., *"Gravitational wave detection by interferometry (ground and space),"* Living Rev.Relativity, Vol. 3, No. 3, 2000.

[3]   Humble, R.W., Henry, G.N., and Larson, W.J., *"Space propulsion analysis and design,"* McGraw-Hill, New York, 1995.

[4]   Katz, I., Goebel, Dan, M., *"Fundamentals of electric propulsion : ion and Hall thrusters"* Hoboken, N.J.: Wiley, 2008.

[5]   Sutton, G., *"Rocket propulsion elements - An introduction to the engineering of rockets"* (6th revised and enlarged edition) [Book]," New York, Wiley-Interscience, 1992, 646 pg.

[6]   Spence, P., "Deep Space 1," *Encyclopedia of Astronomy and Astrophysics*, 2002, pp. 5460.

[7]   Hofer, Richard R. (Jet Propulsion Laboratory, California Institute of Technology, Pasadena, CA 91109), Johnson, L.K., Goebel, D.M., *"Effects of an internally-mounted cathode on hall thruster plume properties,"* Collection of Technical Papers - AIAA/ASME/SAE/ASEE 42nd Joint Propulsion Conference, p 1702-1724 Vol. 3, 2006.

[8]   Spores, R.A., Gulezinksi III, F., and Stuhlberger, J., *"In-Space Propulsion,"* 2003 AIAA/ICAS International Air and Space Symposium and Exposition: The Next 100 Y, AIAA 2003-2588.

[9]   Wie, B., and Murphy, D., *"MicroPPT-Based Secondary/Backup ACS for a 160-m, 450-kg Solar Sail Spacecraft,"* 41 st AIAA/ASME/SAE/ASEE Joint Propulsion Conference & Exhibit, 2005, pp. 1-14.

[10]   Burton, R., and Turchi, P., *"Pulsed plasma thruster,"* Journal of Propulsion and Power, Vol. 14, No. 5, 1998, pp. 716-735.

[11]   Rayburn, C.D., Campbell, M.E., and Mattick, A.T., *"Pulsed plasma thruster system for microsatellites,"* Journal of Spacecraft and Rockets, Vol. 42, No. 1, 2005, pp. 161-170.

[12]   Wertz, J.R., and Larson, W.J., *"Space mission analysis and design,"* 1999. El Segundo, Calif. :Microcosm Press; Dordrecht; Boston : Kluwer, c1999. Space technology library ; v. 8

[13]   Selstrom, J.J., *"Thrust and Performance Study of Micro Pulsed Plasma Thrusters,"* Master's Thesis, 2010, pp. 148. Air Force Institute of Technology, Graduate School of Engineering and Management, Wright-Patterson Air Force Base, OH 45433

[14]   Spanjers, G., Bromaghim, D., Lake, J., *"AFRL MicroPPT development for small spacecraft propulsion,"* 38th AIAA/ASME/SAE/ASEE Joint Propulsion Conference and Exhibit, Indianapolis, IN; United States; 7-10 July 2002

[15]   Jahn, R.G., "Physics of electric propulsion," McGraw-Hill, 1968. Ch 8-9.

[16]   Prof. Manuel Martinez-Sanchez, Spring 2004, *"16.522 Space Propulsion"* (Massachusetts Institute of Technology: MIT OpenCouseWare), http://ocw.mit.edu (Accessed [Date]). License: Creative Commons BY-NC-SA

[17]   Bluhm, H., and Rusch, D., "Pulsed power systems," Springer Berlin, 2005.

[18]   Kesenek, C., Branam, R.D., and Reed, G., *"Contamination Study of Micro Pulsed Plasma Thruster,"* 2008. Air Force Institute of Technology, Wright-Patterson Air Force Base, OH 45433

[19]   Keidar, M., Boyd, I.D., Antonsen, E., *"Electromagnetic effects in the near-field plume exhaust of a micro-pulsed-plasma thruster,"* Journal of Propulsion and Power, Vol. 20, No. 6, 2004, pp. 961-969.

[20]   Myeongkyo, S.*,"Characterizing the Exhaust Plume of the Three-Electrode Micro Pulsed Plasma Thrusters,"* 2009. Air Force Institute of Technology, Graduate School of Engineering and Management, Wright-Patterson Air Force Base, OH

[21]   Branam, Richard D., *"Geo-orbital Nano-thruster Analysis and Testing (GNAT) Laboratory"*, Description document, Asst. Professor of Aerospace Engineering, Air Force Institute of Technology, Wright-Patterson Air Force Base, 45433

[22]   Ziemer, John K. *"Performance Measurements Using a Sub-Micronewton Resolution Thrust Stand."* Presented at Presented at the 27th International Electric Propulsion Conference, Pasadena, CA, 15-19 October, 2001. California Institute of Technology.

[23]   Reid, Gary, J., *"Linear System Fundamentals, Continuous, and Discrete, Classic, and Modern."* Ch. 7 State-Space Analysis 1983, McGraw-Hill Co. New York.

[24]   Ogata,Katsuhiko. Ch. 11, Analysis of Control Ssytems in State Space, *"Modern Control Engineering"*, Ch. 11, Analysis of Control Ssytems in State Space,. 4ed., 2002,Prentice Hall, ISBN 0-13-060907-2.

[25]   Busek Co. *"Multi-Emitter Operations and Maintenance Manual"*. December 22, 2009. Natick MA 01760

Appendix A. Physical Dimensions of the Torsion Balance

Thesis: Gatling Gun-micro Pulsed Plasma Thruster (PPT) 24 Sept 2010-Equipment setup-calibration Thruster Physical Characteristics and Measurements Mass: 1.898 Kg (Satellite Design Scale) 1.895 Kg (Chemical Back Lab Scale) Dimensions: (L/H) 7-7/32"~7.25 in (Length or height) (W) 4-7/32"~4.25 in (Width-side to side) (D) 5-7/32"~5.25 in (front to back) Center of Mass Setup:	3x3 in. 5 in.

Scale 2
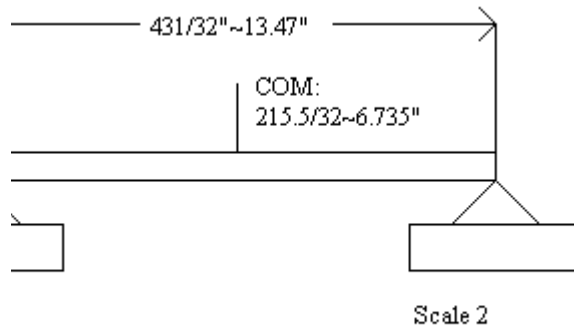
Center of Mass properties
Zbar (L/H):   3-29/32" from top
Ybar (from power supp. side) 2-6/32~2.1875"
Xbar (from front to back

Torsional Balance Characteristics
Arm length: 18-24/32=18.75" edge-edge
Geometric Center: 1.5"x 1.5" on each plate

Distance between
geometric centers: 15-24/32=15.75"

Hole spacing (arm-arm)
15.1225mm~0.5954"

Hole spacing (side-side)
8.6225mm~0.3395"

Counter weight
- Material: T6061 Al
- $V=45$ in.^{3}
- M=1.921 kg
- 10/32 hole drilled base of weight for mounting

Appendix B: Test Conditions

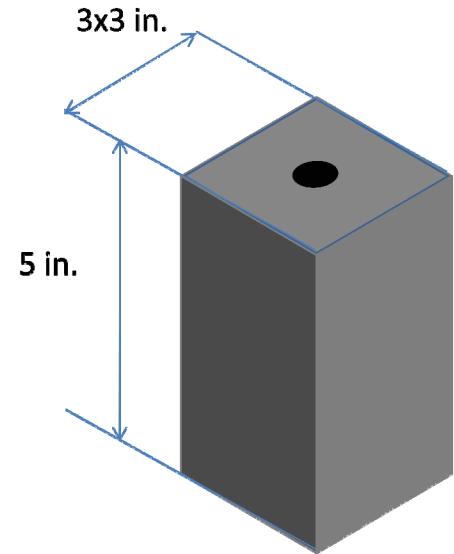| Test Condition #	Frequency (Hz)	Discharge Energy (J)	Voltage (V)	Ibit (μN-s)	shot count
1.	0.500	1.47	17.5	107.00	36
2.	0.500	1.47	12.5	96.50	47
3.	0.668	1.47	12.5	79.00	50
4.	1.000	1.47	15.0	107.00	101
5.	1.000	1.47	12.5	96.00	58
6.	1.500	1.47	20.0	157.00	94
7.	1.500	1.47	15.0	106.00	81
8.	2.000	1.47	17.5	134.00	134
9.	2.000	1.47	15.0	96.00	134
10.	0.500	1.697(No Cal)	12.5	95.20	25
11.	0.500	1.697	12.5	73.00	43
12.	0.500	1.697	15.0	70.00	38
13.	0.500	1.697	15.0	66.20	38
14.	0.500	1.697 (No Cal)	17.5	62.20	25
15.	0.500	1.697	17.5	61.10	43
16.	0.500	1.697 (No Cal)	20.0	54.80	25
17.	0.500	1.697(No Cal)	20.0	52.30	25
18.	1.000	1.697	12.5	60.70	81
19.	1.000	1.697	15.0	68.20	92
20.	1.000	1.697	17.5	77.10	66
21.	1.000	1.697	20.0	67.20	88
22.	1.500	1.697	12.5	109.00	133
23.	1.500	1.697	15.0	72.10	129
24.	1.500	1.697	17.5	71.20	128
25.	1.500	1.697	20.0	66.00	141
26.	2.000	1.697	12.5	70.10	160
27.	2.000	1.697	15.0	109.00	160
28.	2.000	1.697	17.5	106.00	159
29.	0.500	1.6	12.5	31.20	45
30.	0.500	1.6	15.0	34.70	45
31.	0.500	1.6	17.5	36.80	43
32.	0.500	1.6	20.0	37.80	44
33.	1.000	1.6	12.5	36.30	53
34.	1.000	1.6	15.0	32.70	69
35.	1.000	1.6	17.5	35.70	86
36.	1.000	1.6	20.0	38.80	88
37.	1.500	1.6	12.5	29.70	130
38.	1.500	1.6	15.0	29.90	122

39.	1.500	1.6	17.5	16.20	130
40.	1.500	1.6	20.0	30.60	128
41.	2.000	1.6	12.5	55.40	164
42.	2.000	1.6	15.0	43.50	160
43.	2.000	1.6	17.5	43.00	166
44.	2.000	1.6	20.0	42.90	170
45.	0.600	1.6	20.0	38.20	7
46.	0.500	1.4	12.5	108.00	44
47.	0.500	1.4	15.0	107.00	43
48.	0.500	1.4	17.5	108.00	41
49.	0.500	1.4	20.0	108.00	41
50.	1.000	1.4	12.5	96.50	87
51.	1.000	1.4	15.0	97.10	86
52.	1.000	1.4	17.5	87.90	88
53.	1.000	1.4	20.0	82.00	88
54.	1.500	1.4	12.5	91.80	130
55.	1.500	1.4	15.0	59.00	130
56.	1.500	1.4	17.5	55.20	130
57.	1.500	1.4	20.0	77.60	128
58.	2.000	1.4	12.5	49.70	173
59.	2.000	1.4	15.0	85.50	172
60.	2.000	1.4	17.5	88.60	172
61.	2.000	1.4	20.0	99.10	173
62.	0.600	1.4	12.5	33.80	51
63.	0.600	1.4	15.0	30.50	52
64.	0.600	1.4	17.5	63.30	54
65.	0.600	1.4	20.0	70.90	52
66.	0.500	1.3	12.5	56.30	43
67.	0.500	1.3	15.0	95.30	41
68.	0.500	1.3	17.5	89.00	42
69.	1.000	1.3	12.5	62.60	86
70.	1.000	1.3	15.0	40.00	86
71.	1.000	1.3	17.5	67.10	85
72.	1.000	1.3	20.0	82.40	86
73.	1.500	1.3	12.5	55.70	130
74.	1.500	1.3	15.0	96.20	130
75.	1.500	1.3	17.5	73.90	128
76.	1.500	1.3	20.0	82.50	129
77.	2.000	1.3	12.5	78.90	170
78.	2.000	1.3	15.0	84.20	175
79.	2.000	1.3	17.5	60.80	173
80.	2.000	1.3	20.0	42.90	173

81.	0.500	1.2	12.5	62.10	43
82.	0.500	1.2	15.0	41.10	43
83.	0.500	1.2	17.5	27.40	43
84.	0.500	1.2	20.0	58.70	43
85.	1.000	1.2	12.5	58.00	88
86.	1.000	1.2	15.0	42.90	88
87.	1.000	1.2	17.5	32.00	87
88.	1.000	1.2	20.0	57.40	86
89.	1.500	1.2	12.5	68.50	130
90.	1.500	1.2	15.0	38.70	128
91.	1.500	1.2	17.5	102.00	129
92.	1.500	1.2	20.0	62.60	131
93.	2.000	1.2	12.5	70.20	173
94.	2.000	1.2	15.0	91.70	175
95.	2.000	1.2	17.5	47.00	174
96.	2.000	1.2	20.0	92.30	175

Appendix C Thrust vs. Voltage for 1.7 thru 1.2J

This first graph Figure 51 shows how the thrust varies from 12.5 volts to 20 volts, the
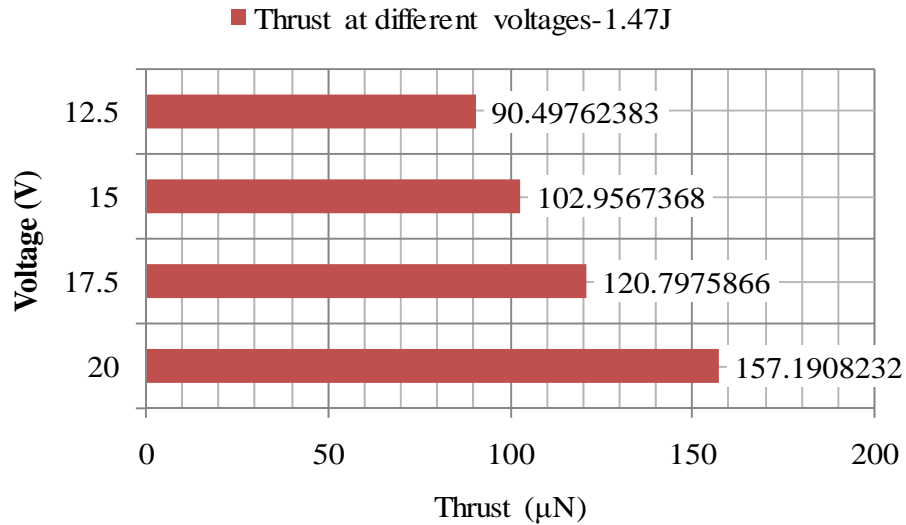trend is that there is a slight increase in the thrust levels.

Figure 51. Thrust vs. Voltage for 1.47J

The next plot is the 1.697J plot and it has different behavior and not the smooth
progression that is was in Figure 51. Here, the 15 volt setting actually has the highest thrust
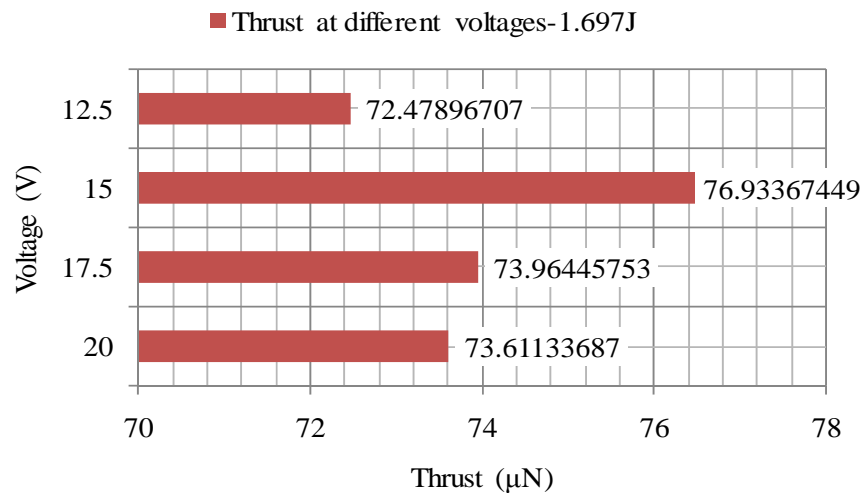number.

Figure 52. Thrust vs. Voltage for 1.697J

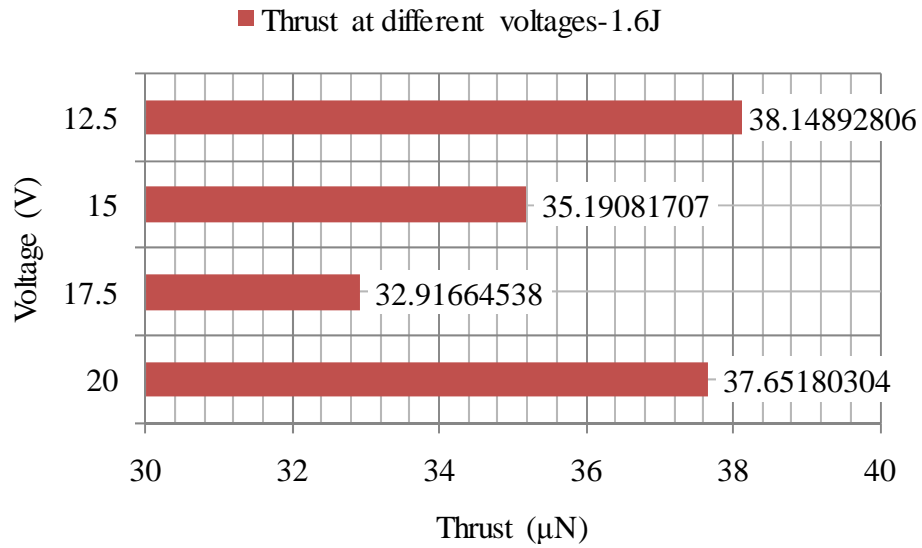The 1.6J data is different from the two previously.

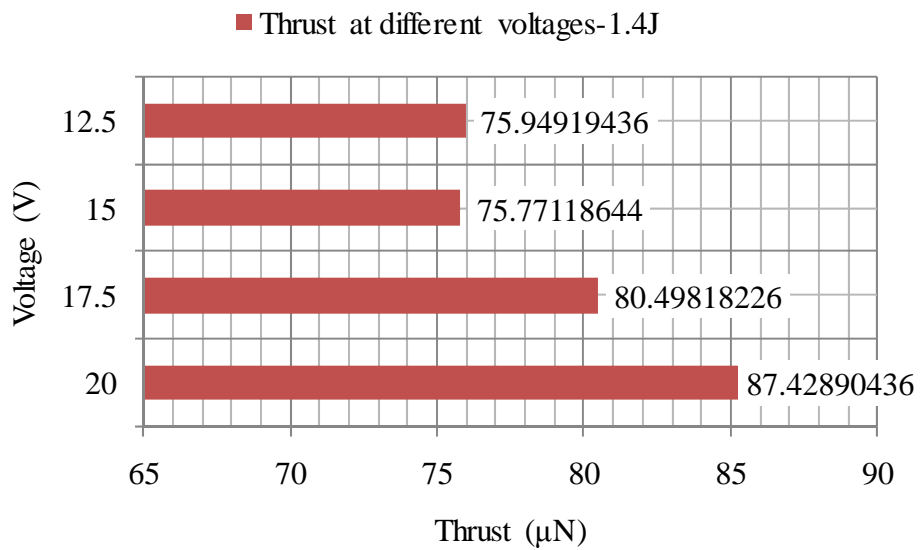Figure 53. Thrust vs. Voltage for 1.6J

Figure 54. Thrust vs. Voltage for 1.4J

The 1.4J data appears to follow the same path as the 1.47J with regard to increasing thrust with voltage.

100

The thrusts are very close to each other in this set, probably no statistical difference between the thrust values.
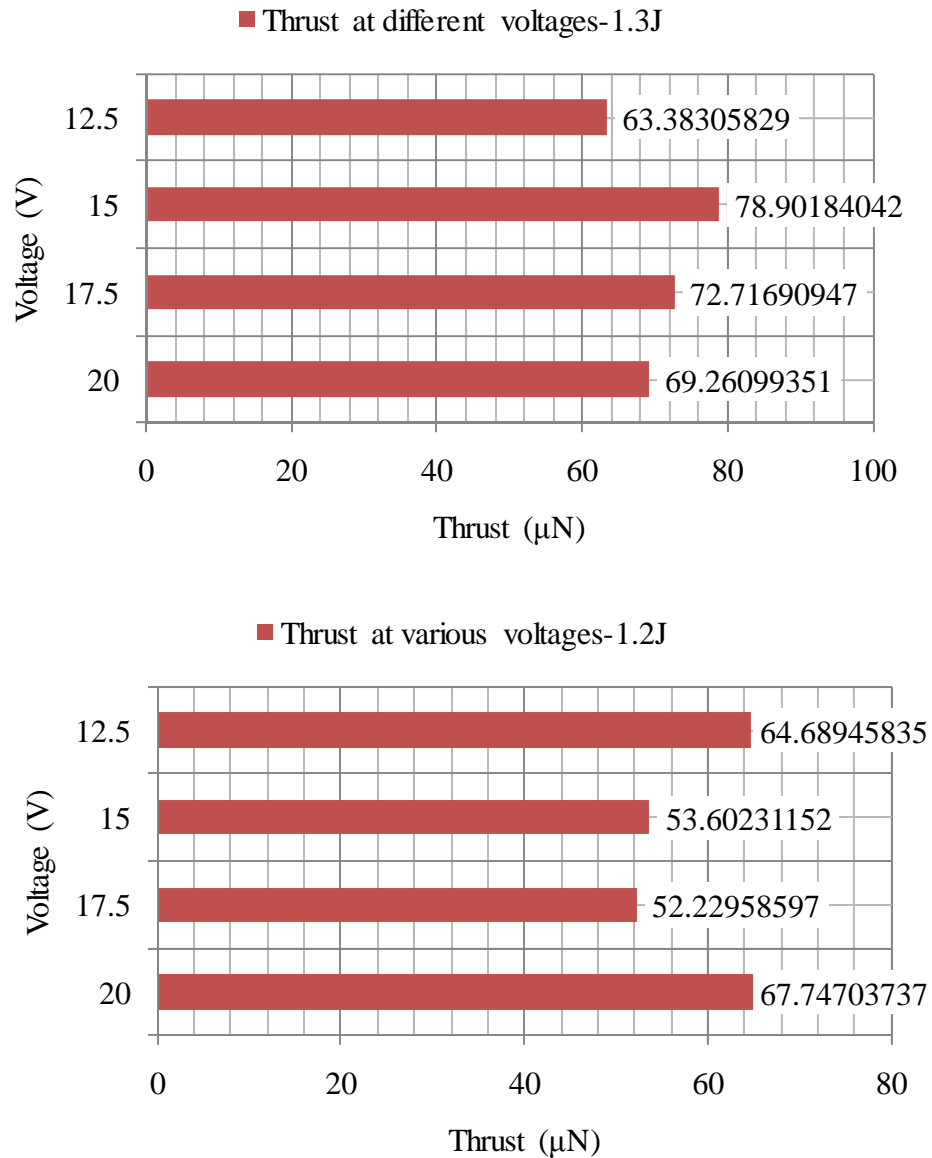

Figure 55. Thrust vs. Voltage for 1.3J and 1.2

The thrust appears to have a small 'bowl' in the middle of the voltage ranges, where the voltages are less than the lower and higher end values.

Vita

Captain Lee Watson graduated from Henry Foss High School in Tacoma, WA. He entered undergraduate studies at the University of Washing in Seattle, WA where he graduated with a Bachelor of Science degree in Aeronautical Engineering in June of 2003. He entered Officer Training School upon graduation and commissioned as a second Lieutenant in the United States Air Force.

His first assignment was at Edwards AFB, CA as a performance and flying qualities engineer on the F-22 program as part of the combined test force (CTF) in Nov, 2003. In Nov, 2006, he was assigned to the AWACS 40/45 system program office (SPO) at Hanscom AFB, MA. While there, he was the program office lead and coordinator for all flight test activities. In Aug of 2009, he entered the Graduate School of Engineering and Management, Air Force Institute of Technology. Upon graduation, he will be assigned to the Air Force Research Laboratory's Propulsion Directorate at Edwards AFB, CA.

					Form Approved
REPORT DOCUMENTATION PAGE					OMB No. 074-0188

The public reporting burden for this collection of information is estimated to average 1 hour per response, including the time for reviewing instructions, searching existing data sources, gathering and maintaining the data needed, and completing and reviewing the collection of information. Send comments regarding this burden estimate or any other aspect of the collection of information, including suggestions for reducing this burden to Department of Defense, Washington Headquarters Services, Directorate for Information Operations and Reports (0704-0188), 1215 Jefferson Davis Highway, Suite 1204, Arlington, VA 22202-4302. Respondents should be aware that notwithstanding any other provision of law, no person shall be subject to an penalty for failing to comply with a collection of information if it does not dIsplay a currently valid OMB control number.
PLEASE DO NOT RETURN YOUR FORM TO THE ABOVE ADDRESS.

1. REPORT DATE (DD-MM-YYYY)	2. REPORT TYPE	3. DATES COVERED (From – To)
24-03-2011	Master's Thesis	Aug 2009 – Mar 2011

4. TITLE AND SUBTITLE	5a. CONTRACT NUMBER
Using a Gatling-Gun Configured Micro Pulsed Plasma Thruster as a Means to Control Micro Satellites with Extreme Precision	5b. GRANT NUMBER
	5c. PROGRAM ELEMENT NUMBER

6. AUTHOR(S)	5d. PROJECT NUMBER
Watson, Lee I., Captain, USAF	11Y38
	5e. TASK NUMBER
	5f. WORK UNIT NUMBER

7. PERFORMING ORGANIZATION NAMES(S) AND ADDRESS(S)	8. PERFORMING ORGANIZATION REPORT NUMBER
Air Force Institute of Technology, Graduate School of Engineering and Management (AFIT/EN) 2950 Hobson Way, Building 640 WPAFB OH 45433-8865	AFIT/GAE/ENY/11-M32

9. SPONSORING/MONITORING AGENCY NAME(S) AND ADDRESS(ES)	10. SPONSOR/MONITOR'S ACRONYM(S) AFRL/RZS
Air Force Research Laboratory/ Propulsion Directorate Attention: Mr. Michael Huggins 525-5230 michael.huggins@edwards.af.mil Building: 8353,Rm: 216B 5 Pollux Drive Edwards AFB, CA 93524	11. SPONSOR/MONITOR'S REPORT NUMBER(S)

12. DISTRIBUTION/AVAILABILITY STATEMENT
APPROVED FOR PUBLIC RELEASE; DISTRIBUTION UNLIMITED.

13. SUPPLEMENTARY NOTES
This material is declared a work of the U.S. Government and is not subject to copyright protection in the United States

14. ABSTRACT
Micro-Pulsed Plasma Thrusters (μPPT) are becoming increasingly attractive for their low power consumption and moderately high specific impulse from 800-1000s. The Gatling Gun micro-Pulsed Plasma Thruster (GG-μPPT) is a new device offering reduced mass and higher thrust than single μPPTs in precise pointing and orbit maintenance applications. The performance of μPPTs depends on frequency and applied voltage/power levels. A variation of these input parameters and effects on operation and performance of this thruster system will be the focus of this research. Contamination aspects will also be considered, since the buildup of carbon results in decreased life for these thrusters. The goal is to match the frequency and power input to avoid this operating condition.

15. SUBJECT TERMS
Micro-PPT, Pulsed Plasma Thruster, Lorentz Force

16. SECURITY CLASSIFICATION OF:			17. LIMITATION OF ABSTRACT	18. NUMBER OF PAGES	19a. NAME OF RESPONSIBLE PERSON Richard E. Huffman, Lt Col, USAF
a. REPORT	b. ABSTRACT	c. THIS PAGE	UU	119	19b. TELEPHONE NUMBER (Include area code) (937) 255-6565, ext 7490 (Richard.Huffman@afit.edu)
U	U	U			

Standard Form 298 (Rev. 8-98)
Prescribed by ANSI Std. Z39-18